INFRARED LASER SPECTROSCOPY OF SALT-SOLVENT COMPLEXES USING HELIUM NANODROPLETS

Thesis submitted for the degree of

Doctor of Philosophy

at the University of Leicester

by

Ahmed M, Sadoon

Department of Chemistry

University of Leicester

2017

INFRARED LASER SPECTROSCOPY OF SALT-SOLVENT COMPLEXES USING HELIUM NANODROPLET

Ahmed M, Sadoon

Abstract

Infrared (IR) spectra of complexes consisting of an alkali halide salt (MX) molecule and one or more protic solvent molecules have been recorded for the first time in this thesis. NaCl and LiI are the principal salts investigated and have been combined with the solvents water and methanol to form complexes of type $MX(solvent)_n$ (n = 1-7) in liquid helium nanodroplets. IR spectra were recorded using a depletion technique. For small complexes (n = 1 – 3) the spectra are consistent with formation of contact ion-pair structures in which each solvent molecule forms a single ionic hydrogen bond (IHB) to an intact M^+X^- ion-pair. For $n \geq 4$, the IR spectra suggest that multiple isomers of $MX(solvent)_n$ are present in helium nanodroplets. *Ab initio* calculations were used to support the results by predicting possible structures and their corresponding IR spectra.

A mass spectrometric study of a variety of alkali halide salts with a variety of protic and aprotic solvents in helium nanodroplets was also performed. The aim here was to survey the mass spectrometric behaviour of species within the helium nanodroplets in preparation for future IR spectroscopic studies. The salts chosen for this study were NaCl, NaBr, NaF, NaI, LiI, LiCl, CsI and KF, while the solvents chosen were water, methanol, acetone and acetonitrile, i.e. two protic and two aprotic solvents. The ions observed in the mass spectra have been described and assigned to be derived from the neutral species in helium nanodroplets environment.

Acknowledgements

First and foremost, I want to express my deepest and sincere gratitude to my academic supervisor Prof. Andrew Ellis, who supported, encouraged and challenged me to learn as much as possible in laser science during my PhD study. Also, I want to thank him for his precious feedback and editorial guidance which helped immeasurably in crafting this thesis.

The technical staff at the University of Leicester, namely Carl Schieferstein, Praful Chauhan and Gareth Bustin, helped in the maintenance of the experimental equipment. Furthermore, Dr Corey Evans, Dr Andrew Hudson and Dr Adrian Boatwright have been extremely helpful throughout the research project, including assisting with computational chemistry calculations.

I would like to thank the entire Laser Chemistry group at the University of Leicester who have made my three years of research incredibly enjoyable and significantly easier. Also gratefully acknowledged is my sponsor, the Ministry of Higher Education and Scientific Research in Iraq and their representative in the UK, the Iraqi Cultural Attaché, for giving me the opportunity to study for a PhD.

Finally, I am greatly thankful to my family and friends for always finding the right words to put a smile back on my face and for providing unparalleled support during my educational years.

Table of Contents

List of Tables

List of Figures

CHAPTER 1

Introduction

1.1 Introduction

The behaviour of ions in solutions has been the subject of much study over many decades.[1-3] The importance of understanding the behaviour of ions in solution derives from the critical role they play in general solution chemistry, as well as in specific areas such as environmental chemistry, electrochemistry,[4] and numerous other chemical disciplines.[5] Biologically, ions are essential in the function and structure of nucleic acids, proteins, and lipid membranes.[6] Ion-selective chemistry is derived from the non-ideal behaviour of ions, such as that seen for cell signaling using K^+ and Na^+,[7, 8] and reflect the fact that solutions under quite modest ionic strengths have significantly different properties from the infinite dilution limit.[3] Such deviations from ideality are strongly affected by ion-pairing effects.

Information about ion-pairs is usually extracted from the properties of bulk solutions, such as their relaxation response, thermodynamics and ion transport, but these measurements are unable to describe the intricate behaviour of ion-pairs at the molecular scale.[9,10] On the other hand, simulation methods like molecular dynamics or Monte Carlo calculations are widely used to provide valuable complementary information. Unfortunately, an accurate simulation of the properties of even simple electrolytic solutions is still difficult.[11]

A challenge in the experimental study of ion-pairs is to find techniques for making these ion-pairs and analyzing their properties. Also, the experimental technique must be capable of observing and identifying various types of ion-pairs. The work in this thesis will address the interaction between cation-anion pairs and a solvent, such as water or another polar solvent. The ion-pairs will be salts in molecular form, such as alkali halide molecules. The specific targets are complexes derived from ‘salt’ molecules, such as NaCl, with attached solvent molecules. Infrared (IR) spectroscopy is a good option for recording spectra,

since the OH stretching region is a sensitive probe of hydrogen bonding networks. The aim will therefore be to use IR spectroscopy to determine the structures of the isolated solvated alkali halide complexes. The ultimate motivation is to see if there is any evidence for ion separation into distinct M^+ and X^- ions with an increasing number of solvent molecules. As will be seen later, helium nanodroplets were used as the interaction medium in which to trap these salt-solvent complexes.

1.2 Salt-Solvent Interactions

Since this work deals with the ion-pair/solvents interaction, it is worth discussing the Hofmeister series, in brief, as a way of characterising ion behaviour in solution. It's well known that ions have a significant effect on solvent properties, such as the liquid surface tension and the solubility of proteins.[12-15] The effect of ions on the latter was studied for the first time by Hofmeister in 1888.[16] The focus was on studying the ability of different cations and anions to "salt in" or "salt out" proteins from aqueous solutions, giving rise to the so-called Hofmeister series. For cations, the common order of the Hofmeister series is[17, 18]

$$Cs^+ > Rb^+ > NH^+ > K^+ > Na^+ > Li^+ > Ca^{+2} > Mg^{+2} > Zn^{+2}$$

while for anions, the order is usually giving as

$$F^- > HPO_4^{-2} > \text{acetate} > Cl^- > NO_3^- > Br^- > ClO_3^- > I^- > ClO_4 > SCN^-$$

The ions on the left side of the series increase the surface tension of the solvent and thus decrease the solubility of nonpolar molecules by strengthening the hydrophobic interaction (salting out). By contrast, the ions on the right side of the series increase the solubility of nonpolar molecules by weakening the hydrophobic effect (salting in). More details about the effect of ion size on the dissolution behaviour, *kosmotropic* and *chaotropic* behaviour, will be discussed in Chapter Four.

The stepwise process by which a salt molecule dissolves can be explained within the context of the Eigen-Tamm model.[19] This is actually more usually used as a means of describing the stages of ion association in solution but here it will be viewed in reverse, i.e. as a dissolution process. The basic underlying idea is that

an association or dissociation process involving two oppositely charged ions in the presence of a solvent can go through several different states corresponding to different energy minima. The concept is illustrated in Figure 1.1, which focuses on a salt (MX) in an aqueous solution.

Figure 1.1. Schematic representation of salt dissolution in solution showing the four notional stages. The blue shading is intended to indicate the solvent medium immediately around the solute.

The (MX)/water dissolution process has four steps. The starting point is the bringing together of MX and solvent molecules. The first energy minimum is a hydrated contact ion-pair (CIP). In this state, the cation and anion are in direct contact and are surrounded by solvent molecules. The cation-anion distance will tend to be longer than that of the bare MX molecule because of the interaction with the solvent. Some solvents, and most obviously water molecules, can eventually insert between the two ions. When a single water molecules inserts between the two ions we get a second potential energy minimum known as a solvent-separated ion-pair (SSIP). The third state of ion-pair dissociation is the (double) solvent separated ion-pair (2SIP), where both ions have complete primary solvation shells. Finally, the complete dissolution state occurs when ions drift apart, as is typical in a dilute aqueous solution.[20]

This mechanism is supported by different experimental and theoretical studies of salts in water. Molecular dynamics and Monte Carlo simulation studies[21, 22] show that these ion-pairs do indeed correspond to energy minima but in fact the barriers, separating one state from another, depend strongly on the identity of the salt and the solvent.

The transition from CIP to SSIP reflects the beginning of ionic dissolution. The identification of a SSIP in a bulk solution using spectroscopic methods, such as Raman spectroscopy, is difficult because of the small difference in signals between the SSIP/2SIP states and the bulk solvent molecules. This is

compounded by the limited spectral resolution available in bulk liquids because of the rapid collision rates.[21]

Numerous experimental and theoretical studies have addressed the effect of ion size on the structures of CIP and SSIP.[23-27] A significant study that focused on the effect of ion size and the hydration number on formation of CIPs has been reported by Liu *et al.*[27] Using classical molecular dynamics calculations, Liu *et al*. suggest that the relative cation and anion sizes are vital in determining how many water molecules must be added before formation of an SSIP complex becomes plausible. This study found that the CIP structure of $LiI(H_2O)_n$ exists between n =1 and n =4 and thereafter a SSIP-like complex forms for n = 5. In marked contrast, for CsI a CIP-like structure for the salt is maintained up to about n = 20, i.e. the salt is less willing to 'dissolve' in a small quantity of water than LiI. Liu *et al.* claimed that the main reason for the difference between the CIP structure of $CsI(H_2O)_n$ and $LiI(H_2O)_n$ complexes is likely a result from the weak interaction of CsI with water compared to the strong interaction of LiI with water.[27] Also, the calculations illustrate that water molecules prefer to interact with the alkali cation rather than with the negative ion like iodide. In other words, the water molecules in the SSIP complex surround the positive ion while the negative ion is located at the cluster surface. Several other studies will be discussed later in the following chapters.

Given the limited experimental evidence available for CIP and SSIP complexes in bulk solutions, this study approaches the problem in a different way. As mentioned above, the ion-pairs in contact with a small number of solvent molecules will be studied inside liquid helium nanodroplets. Helium nanodroplets will be used for this purpose for two reasons. First, they provide a convenient method for forming complexes, including very weakly bound complexes. Second, it is possible to record optical spectra using a depletion technique (see later), which is applicable to any absorbing species in helium nanodroplets.

1.3 Helium nanodroplet properties

Helium nanodroplet technology is derived from the combination of two powerful experimental techniques.[28] The first technique is cryogenic matrix isolation,

which has been used for several decades to study transient species, such as molecular radicals[29] and ions.[30] The second technique derives from seeded supersonic beams, which have also been used to cool free molecules to produce transient species such as molecular complexes[31] and clusters.[32] Helium nanodroplets essentially combine these ideas into a single technology.

The most significant properties of helium nanodroplets in this context are their low temperature (0.37 K), their ability to rapidly cool added molecules and their chemical inertness. In addition, helium nanodroplets do not interact with radiation below 20 eV.[33] Furthermore, helium nanodroplets have the ability to easily pick up atoms and molecules to form new species on their surfaces or in their interior, providing a means of combining different molecules at low temperatures.[28] All of these properties mean that helium nanodroplets provide a fascinating nanoscale laboratory for a variety of fundamental experiments.

Helium as an element has two isotopes, ^{4}He and ^{3}He, with ^{4}He being by far the more abundant element isolated in nature. The very weak attractive interaction between helium atoms, which arises from the small atomic size and the closed 1s shell, means that helium only liquefies at very low temperatures. For ^{4}He the critical temperature is 5.2 K. This means that helium cannot be liquefied at temperatures above 5.2 K, even with a large excess pressure.[34] Another remarkable property of ^{4}He is that it will not solidify at pressures near that of atmospheric pressure even at a temperature of absolute zero. This property comes from the small atomic mass of helium in combination with the very weak attractive interatomic forces, which means that the zero point vibrational energy exceeds the binding energy required to fix the helium atoms at specific lattice sites.[35]

In the bulk, ^{4}He shows another significant property. At a temperature below 2.18 K, the liquid changes phase from a normal liquid to a superfluid.[20] The normal fluid phase is often labelled as the He I phase. In the superfluid phase, referred to as He II, the liquid possesses some remarkable properties such as the absence of viscosity and an exceedingly high thermal conductivity.

The other isotope of helium, ^{3}He, can also form a superfluid phase. However, because ^{3}He atoms are fermions (half integer net spin), whereas ^{4}He atoms are bosons (integer) zero (net spin), formation of the superfluid phase requires a much lower temperature for ^{3}He as the fermions must pair up to make quasi-bosons. The transition temperature is 0.003 K and this, coupled with the very low abundance of ^{3}He (making it very expensive), means that ^{3}He is rarely used in helium nanodroplet experiments. Everything that follows is therefore focused on ^{4}He nanodroplets.

1.3.1 Helium nanodroplet formation

Helium droplets were observed for the first time about 100 years ago as a fog during the cooling of helium gas.[36] Other experiments have produced very large droplets with diameters varying from 10 mm to 2 cm in vacuum. Weilert *et al*. [37] formed helium droplets in a trap as a mist by pumping on helium liquid placed in the lower part of the cell to make it boil violently. Droplets in the mist then agglomerated to form a large drop. The large droplets were then levitated by applying a high static magnetic field since helium is diamagnetic. The size of liquid helium drops using this technique was about 2 cm in diameter. Weilert *et al.*, in a different study,[38] used the same method of forming helium droplets but in this case, a laser beam was used to levitate droplets of 10–20 μm diameter. In a different experiment,[39] large positively charged helium droplets were made by field ionization of a liquid in an electrospray experiment. More recently helium droplets were formed using a pulsed expansion of cold helium gas into a helium bath cryostat.[40]

Helium droplets can also be formed using a supersonic (free jet) expansion through a pinhole into a vacuum. Such expansions naturally produce cooling but in the case of helium the interatomic forces are so weak that this is insufficient to cause condensation. Consequently, in order to form helium droplets, cooling of the gaseous helium prior to expansion is essential. The expansion process itself is an adiabatic process, also called an isentropic expansion since the system entropy remains constant during the gas expansion. The random kinetic energy of the gas atoms is converted into directed supersonic flow via two-body or three-body collisions. Two-body collisions can exchange energy but do not allow an

initial He_2 dimer to form. To achieve this, a third body is needed to remove excess energy and trap the system in the dimer potential energy well. This dimer provides the seed for subsequent condensation.[41]

There are different expansion regimes for helium droplet formation depending on the stagnation pressure and temperature, namely sub-critical and super-critical regimes. Figure 1.2 shows a phase diagram which helps to explains these regimes. The dashed lines refer to different isentropes, which reflect the helium behaviour during the expansion process at different temperatures from 40 K to 2.6 K. Figure 1.2 also illustrates a boundary line which almost overlaps with the isentropic line at 11 K. This line is critical for defining the expansion regimes because it separates the gas phase and the liquid phase (He I phase). The sub-critical regime occurs at about $T_0 > 11$ K, when helium crosses the gas – liquid boundary line into the superfluid phase from the gaseous side. This means helium droplets are formed by the accumulation of helium atoms by two- and three-body collisions in the region just after the nozzle orifice. The super-critical regime exists at $T_0 < 11$ K when the expansion isentrope passes the gas-liquid boundary line from the liquid side to form droplets by fragmentation of the fluid. This fragmentation happens downstream from the nozzle aperture at a temperature of about 6 K. Above 6 K and after leaving the nozzle, helium droplets are accelerated from sub-sonic to supersonic while expanding and cooling (see the dotted line in Figure 1.3). When T_0 is below 6 K, helium is present in new regime and ejected from the nozzle as a liquid after passing the velocity separation line. [42-44]

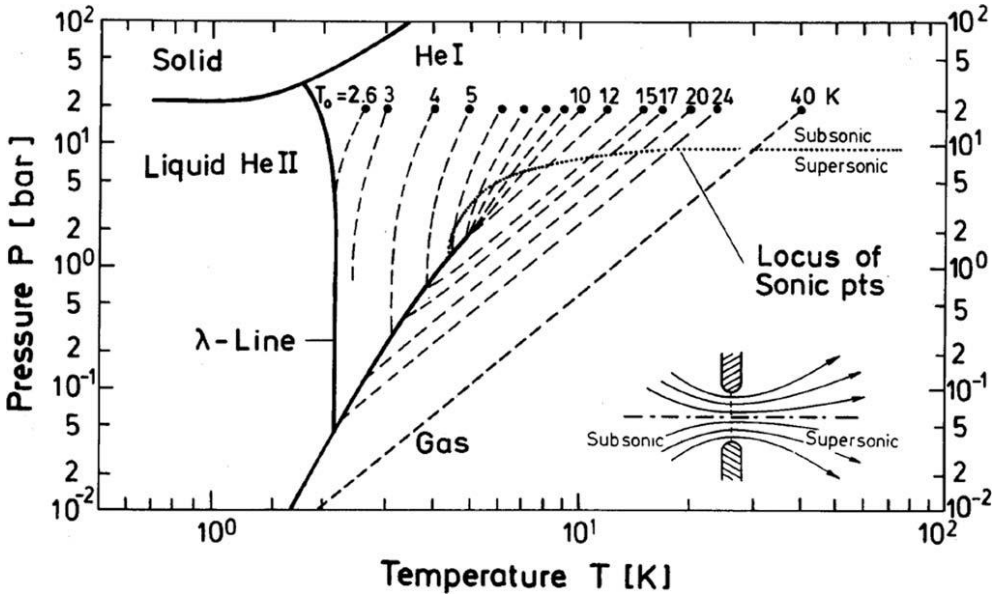

Figure 1.2. Pressure-temperature phase diagram of ^{4}He. The dashed lines are the isentropic lines of droplet formation at a stagnation pressure of P_0 = 20 bar and various temperatures. Reprinted from ref [43].

At distances of about 1000 orifice diameters from the pinhole, collisions between the expanding atoms largely ends and the helium beam consists of a mixture of helium atoms and droplets. [42]

The binding energy of a single helium atom within a droplet is approximately 5 cm^{-1} and at least this quantity of energy is removed from the droplet with the loss of each helium atom. Helium atoms can continue to evaporate from the droplet until the droplet temperature reaches the equilibrium temperature at 0.37 K, at which no further net evaporation occurs. [45, 46]

At present, the majority of liquid helium droplet experiments have been performed with droplets produced in supersonic expansions. Helium droplets by this route were made for the first time by Becker *et al*. in 1961.[47] The experiment involved cooling a nozzle by a liquid helium bath. Helium was then expanded from the nozzle to produce droplets and then converted into a beam using a skimmer. The velocity distribution was then determined by a time-of-flight method in order to demonstrate that the helium droplets have been successfully formed. In more recent studies the ready availability of commercial closed-cycle cryostats makes helium droplets more convenient to make.[42,48-50] Helium droplets are now produced by expanding helium, pre-cooled by a closed-cycle cryostat to a

temperature in the range T_0 = 5–20 K and at a high source pressure (P_0 = 20–100 bar), into a vacuum. The typical nozzle diameter is approximately 5 μm, as illustrated in Figure 1.3. Such an approach was used in the current work and so the next section will discuss this technique in some detail.

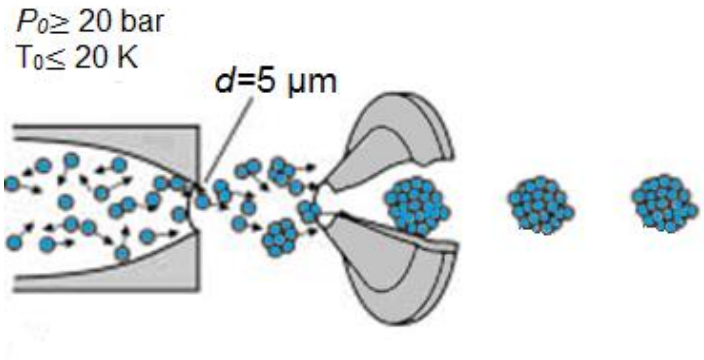

Figure 1.3. Schematic representation of the formation of helium droplets via a supersonic gas expansion.

1.3.2. Droplet sizes

The size of helium droplets depends on the source temperature, helium gas pressure and nozzle diameter. Figure 1.4 shows the dependence of the mean droplet size and the droplet diameter on the source stagnation conditions for P_0 = 20–100 bar and T_0 = 5–20 K using a nozzle with an aperture of several microns diameter.[28] The smallest droplets are made under subcritical expansion conditions (see bottom image in Figure 1.4). Larger droplets with $N_{He}>>10^4$ atoms are formed by expanding liquid helium in a supercritical expansion after leaving the orifice, where the liquid fragments into fairly large droplets (10^5-10^7 helium atoms; middle image in Figure 1.4). Larger droplets with about 10^{10} atoms can be produced by forming a liquid microjet at source temperatures below about 4.2 K (top image in Figure 1.4).[28, 35] This microjet fragments into large droplets by Rayleigh oscillations after travelling for a short distance.

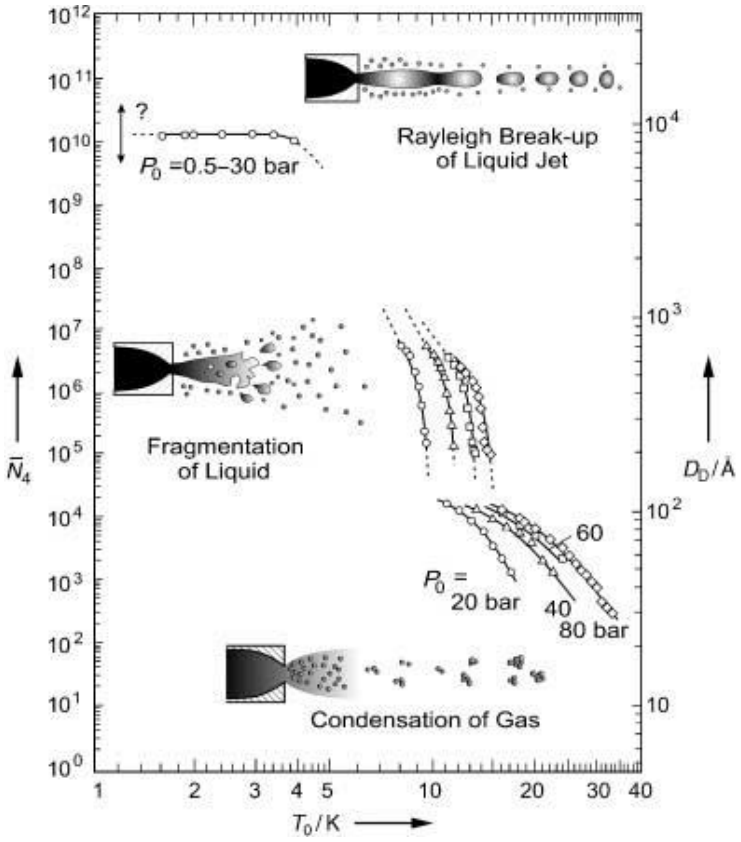

Figure 1.4. Diagram showing how the mean droplet size (*N* helium atoms) and liquid-droplet diameters (D_0) of ^{4}He droplets vary under different expansion conditions. Reprinted from ref [28].

Assuming spherical droplets and a density of helium comparable to that of bulk liquid helium, the average number of helium atoms (N_{He}) contained in one droplet is linked to the droplet radius (R/ Å) by equation [1].[43]

$$R = 0.22\ (N_{He})^{1/3} \qquad [1]$$

The sizes of helium droplets have been investigated experimentally under different source conditions. Harm and Toennies determined the average number of helium atoms by deflecting a helium droplet beam by collisions with a secondary gases beam formed in another free jet expansion source. The helium droplets were formed under different source pressures (P_0 = 40-80) bar and nozzle temperatures between T_0 = 13-26 K with a 20 µm nozzle diameter. The secondary beam consisted of Ar or Kr gas. The two beams were crossed at an angle of 40° and the deflected droplets were then ionized using an electron beam. Helium clusters ions were then detected using a magnetic sector mass

spectrometer, which can be easily rotated around the scattering area in the plane of the two beams. The number of helium atoms in the droplets was found to be about 2600 at a source temperature of 25 K and a stagnation pressure of 80 bar.[51]

The sizes of larger droplets (N_{He}>10^5) have been studied by attaching an electron to the droplet and then deflecting the charged droplets in an electric field for analysis.[52] Droplets have also been formed with sizes in the range of 10^4–10^5 atoms using pulsed droplet sources.[40,53-55] Here the helium droplets were produced using a pulsed nozzle at different pressures and nozzle temperatures. The helium droplets were then passed through a pick-up cell to attach phthalocyanine molecules. Laser induced fluorescence (LIF) was then used to detect the phthalocyanine and the droplet size was derived from the phthalocyanine LIF signal under specific conditions of helium partial pressure and nozzle temperature. The average size of the droplets was found to be about 1.8× 10^4 and 1.4× 10^4 atoms at T_0 = 11 and 12 K, respectively, and P_0 = 20 bar.[53]

In our apparatus, the average number of helium atoms for each droplet has been assumed based on the aforementioned detailed studies of helium droplet sizes and the associated scaling laws, which can be used to predict how the size changes as the source conditions are altered. Typical conditions that were used are a helium stagnation pressure of 32 bar, a nozzle temperature of 16 K and a nozzle diameter of 5 μm. Under these conditions we expect helium nanodroplets to contain a mean number of ~5500 atoms, a typical size for spectroscopy experiments (see later).

1.3.3. Dopant pick-up by helium droplets

In general, helium droplets have the ability to pick up almost any species or impurities present in the gas phase during their journey through the vacuum system. Whether the dopant is located inside or on the surface of helium droplets depends on the dopant properties. The earliest studies of dopants attached to helium droplets was by Gspann *et al*.[56-62] The first such experiments [57,58,60] focused on measuring the loss of Cs or Xe atoms when produced as a beam which crossed a helium droplet beam at a range of crossing angles between 15º-

90º. The extinction of Cs and Xe beams were then calculated with the help of a time-of-flight (TOF) mass analyzer for droplet sizes around 4×10^6 atoms. The data showed that helium can easily pick-up Cs or Xe atoms in or on the helium droplets but no information was provided about the location of these dopants.[63]

Subsequent work has shown that most dopants reside inside helium droplets.[28,35,50] To systematically add a dopant the helium droplet beam is passed through a pickup cell where the chosen dopant is deliberately added, in gaseous form, as shown in the cut-away image of a pickup cell in Figure 1.5.

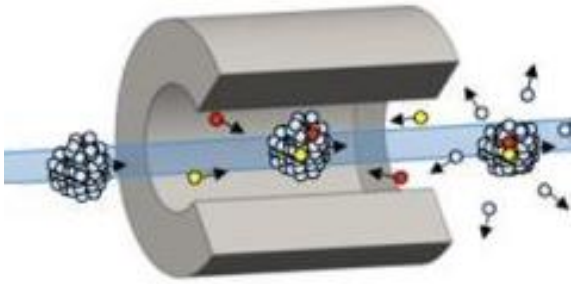

Figure 1.5. Schematic illustration of the pickup procedure**.**

Dopants will be trapped inside helium droplets after losing their initial kinetic energy and their internal energy during the impact with the droplet. As they do so, the droplet shrinks via the evaporation of helium atoms. Since each helium atom is bound to the droplet by a minimum of 5 cm^{-1}, every 1 eV of injected energy leads to evaporation of up to 1600 He atoms.[28, 64]

If a fixed helium droplet size is assumed (i.e. ignoring evaporation of helium atoms by the pickup process), the probability P_k of picking up k dopant particles can be expressed in terms of a Poisson distribution (equation [2]). [43]

$$P_k = \frac{(\rho\sigma l)^k}{k!}\exp(-\rho\sigma l) \qquad [2]$$

Here ρ is the number density of the dopants, σ is the cross sectional area of the droplet and l is the length of the pickup cell. The dependence on how the number of dopants atoms/molecules (k) which are picked up by helium droplets is affected by the dopant partial pressure is shown in Figure 1.6. The assumption of a Poisson distribution of the helium droplets was shown to agree well with experimental studies of helium droplet sizes.[28, 49]

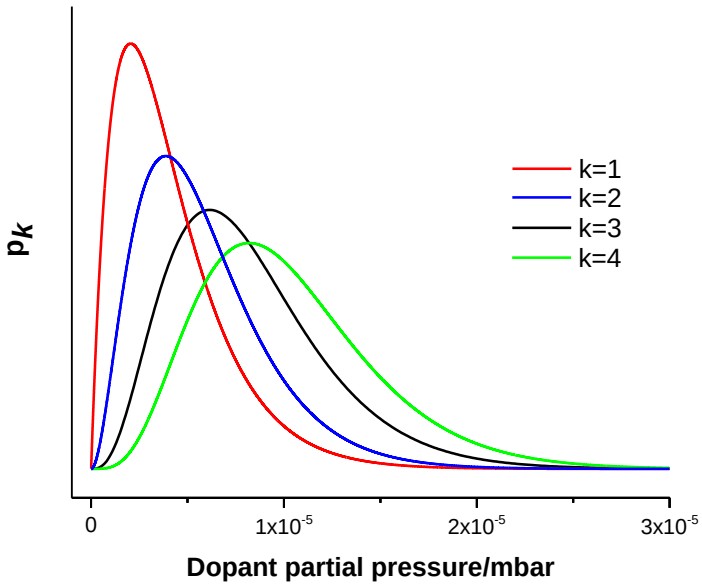

Figure 1.6. The dependence of the number (*k*) of dopant atoms/molecules picked up by helium droplets with different partial pressure values. These plots assume a Poisson distribution and a mean helium droplet size of 5500 atoms.

The gaseous dopants or vapour derived from volatile liquids are easy to capture by helium droplets.[65] Equally, atoms and molecules from low-vapour-pressure species, such as metals or large organic molecules, can also be picked up using a heated cell. Depending on the droplet size, a vapour pressure of about 10^{-6}–10^{-5} mbar is sufficient to pick-up a single atom or molecule.[66,67] The pick-up of highly volatile materials such as refractory metals can also be achieved using a pulsed laser ablation source.[53]

1.4 Infrared spectroscopy of dopants in helium droplets

Helium droplets provide an opportunity for spectroscopic studies of dopants since helium is transparent across a wide wavelength range, including the infrared (IR). There are other benefits to recording spectra using doped helium droplets. A significant one is the chemical inertness of helium. Another property is the very low temperature, which makes it possible to explore the interactions between very weakly bound species inside a helium droplet. The low temperature also helps in terms of simplifying spectra through the reduced population of excited quantum states.[68]

The majority of spectroscopic studies of molecules in liquid helium droplets have used a depletion technique for recording IR spectra. If the dopant molecule absorbs a photon, then the added energy will eventually be dissipated into the droplet, leading to the evaporation of helium atoms. About 1600 helium atoms will be evaporated for every eV of added energy.[35] The depletion spectrum can then be observed by recording the reduction in helium droplet size after absorption of light by the dopant using a bolometer, a sensitive heat measuring device, or by recording the reduction in the ion signal in a mass spectrum (see below and Chapter Two). In this way the optical spectrum is recorded as an action spectrum, i.e. the consequence of light absorption on the ion signal. For the optimum depletion signal, the helium droplets must not be too large, otherwise the percentage change in the ion signal becomes too small. Typically the preferred droplet size is a few thousand helium atoms.[69]

The first spectroscopic study of molecules in helium droplets was by Goyal *et al*.[69] In this experiment, SF_6 was the dopant and was excited using a tunable CO_2 laser. A bolometer was used to detect the difference in the droplet thermal energy as a result of shrinkage in droplet size after absorption. An IR depletion spectrum was thereby recorded by scanning the wavelength of the laser while measuring the bolometer output. Later, the group led by Toennies[70] demonstrated that droplet shrinkage could be registered using a mass spectrometer instead of a bolometer. This can be achieved by following the ion signal produced by electron ionization, which is related to the size of the helium droplets. Thus an optical spectrum can be recorded by monitoring the ion signal in mass spectrometer as the laser wavelength is scanned.

1.5 Previous work on salt-water complexes

The majority of the information on hydrated alkali halide complexes $M^+X^-(H_2O)_n$ has come from *ab initio* calculations and molecular dynamics simulations.[23, 71-80] Nevertheless, several experimental studies have been performed. Photoelectron spectra of $[LiI(H_2O)_n]^-$ and $[CsI(H_2O)_n]^-$ anions have been reported in combination with *ab initio* simulations.[71] This study shows new evidence for the transition from CIP to SSIP in the structures of the corresponding neutral complexes, which are significantly different from the anions. The Li−I distance in the $[LiI(H_2O)_n]^-$ anion

is longer than that in the neutral complex and increases suddenly at n = 3, whereas in neutral $LiI(H_2O)_n$ this occurs at n = 5. This early separation in the $[LiI(H_2O)_n]^-$ anion is derived from the additional electron, which weakens the attraction between the Li^+I^- ion-pair. For $[CsI(H_2O)_n]^-$ there is a significant increase in the Cs−I distance at n = 3 and it reaches a maximum at n = 4, before decreasing with an increase in n. For neutral $CsI(H_2O)_n$, no significant change in the Cs−I distance occurs for n = 0 to 6, presumably as a result of the weak interaction of CsI with water.

Only a few spectroscopic studies of $M^+X^-(H_2O)_n$ complexes have so far provided any structural information. An early study of $NaCl(H_2O)_n$ complexes in an argon matrix provided a vibrational spectrum of $NaCl(H_2O)$. The IR spectrum of this complex shows two bands in the O-H stretching region, in addition to two bands between 400-700 cm^{-1}. These bands suggested a pyramidal structure in which the sodium cation is linked to the oxygen atom of the water molecule, while the chloride anion is located below the base of the pyramid.[80] A microwave investigations of $NaCl(H_2O)_n$ for n = 1-3 has also been reported and was used to extract structural information on these complexes.[81,82] The structures of $NaCl(H_2O)_n$ complexes obtained from this study are different from those deduced from the early matrix IR work. The spectra analysis are supported by theoretical calculations and are consistent with a CIP complex with a steady increase of Na-Cl bond with every additional water molecule. Also the computational chemistry calculations illustrate that the structures contain a bond between the Na ion and the oxygen atom, while the chloride ion is linked to the water molecule through an ionic hydrogen bond (IHB). However, this finding illustrates that three water molecules is insufficient to increase the distance between the Na^+ and Cl^- ions significantly.

Recently, the Leicester helium nanodroplet group recorded IR spectra of $NaCl(H_2O)_n$ complexes in liquid helium nanodroplets. [67] The IR spectra were recorded for n = 1-4 and the spectra for n = 1, 2, and 3 are consistent with formation of the lowest energy CIP structures, in which each water molecule forms a single (IHB) to an intact Na^+Cl^- ion-pair (Figure 1.7). Through a combination of the experimental findings and *ab initio* calculations, different structures with hydrogen bonding between water molecules become

energetically competitive for n = 4, and the IR spectrum indicates likely the coexistence of at least two isomers.

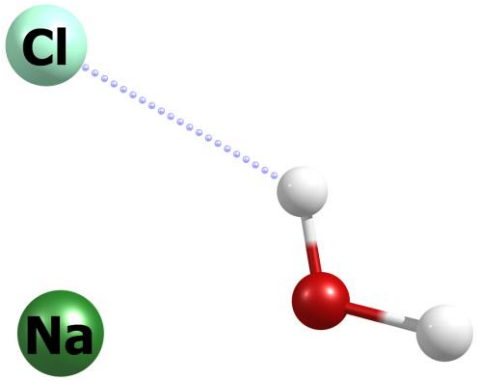

Figure 1.7. The structure of the global energy minimum of $NaCl(H_2O)$ showing an ionic hydrogen bond between the water and the chloride ion in the Na^+Cl^- ion-pair.

1.6 The aim of the work in this thesis

This work builds upon the preliminary study of $NaCl(H_2O)_n$ complexes described in the previous section. It aims to extend the study of the formation and the properties of ion-pairs in solutions by looking at different salts, as well as with other solvents.

The remainder of this thesis is arranged as follows. In Chapter Two, details about the helium nanodroplet apparatus will be provided. In chapters Three, Four and Five, the IR spectra of $NaCl(CH_3OH)_n$, $LiI(H_2O)_n$ and $LiI(CH_3OH)_n$, respectively, are presented and discussed. LiI is an interesting alternative to NaCl because it has a cation and an anion with very different sizes and therefore dramatically different charge densities. This difference provides an opportunity to compare the effect of cation and anion size on the hydration process.

The final chapter presents mass spectra recorded for a variety of salts with a variety of polar solvents such as water, methanol, acetone and acetonitrile. These measurements were made as a foundation for future IR spectroscopic studies.

CHAPTER 2

Experimental Apparatus

2.1. The superfluid helium nanodroplet system: an overview

The apparatus used in these experiments was the helium nanodroplet apparatus illustrated in Figure 2.1. It provides a high vacuum environment in which to grow, dope and probe helium nanodroplets. The system consists of three vacuum chambers isolated by two gate valves. The vacuum seals on all chambers use copper gaskets to try and achieve the highest possible vacuum. Before entering the first chamber, the source chamber, high-purity helium gas is pre-cooled using a closed-cycle cryostat. This cold gas then expands into the source chamber by supersonic expansion through a pinhole aperture. The second chamber is the pick-up zone in which atoms and molecules, in the gas phase, can be added to the helium nanodroplets. Sequential pick-up of more than one substance is possible when the nanodroplets travel through different pick-up regions. In this case binary clusters can be formed. Finally, the third chamber is the analyzing chamber and here there is a quadrupole mass spectrometer. It is also here where the laser beam used for recording IR spectra enters the apparatus. The base pressures in the source chamber, pick-up and mass spectrometer chambers are around 10^{-7}, 10^{-8} and 10^{-10} mbar, respectively.

A photograph of the helium nanodroplet apparatus is shown in Figure 2.2. More details will be provided about each part of the apparatus in the following sections.

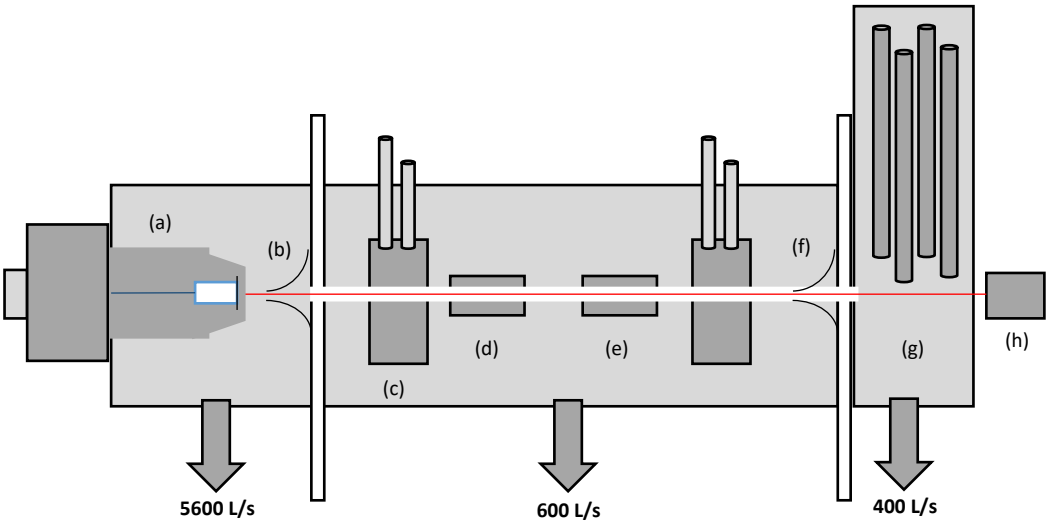

Figure 2.1. Schematic showing the three vacuum chambers of the helium nanodroplet apparatus. (a) Helium droplet source, (b) 0.5 mm nickel skimmer, (c) cryo-trap (77 K), (d) evaporator oven, (e) solvent pick-up cell, (f) 5 mm nickel skimmer, (g) quadrupole mass spectrometer and (h) OPO/A laser for spectroscopic studies. Pumping speeds are shown beneath each chamber in L/s.

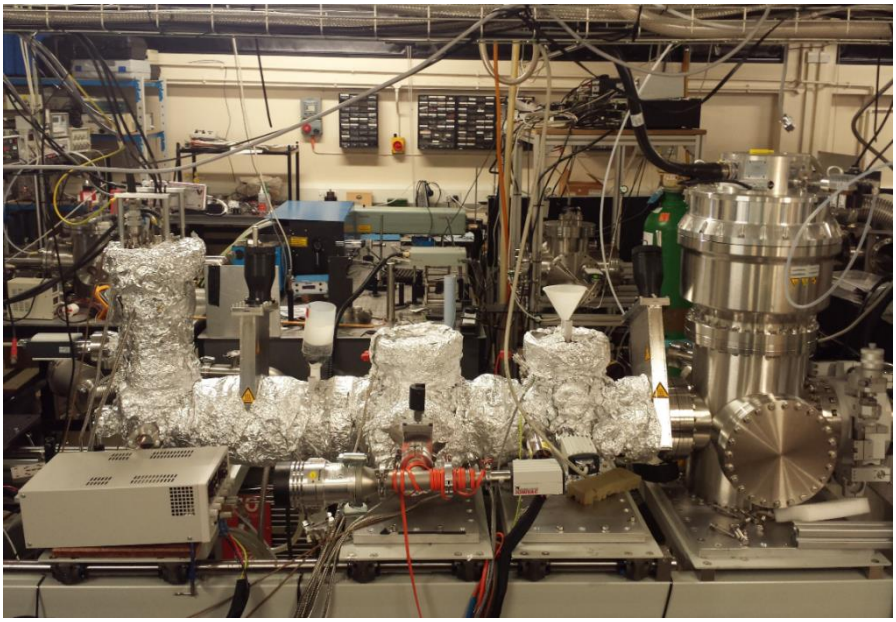

Figure 2.2. Photograph of the helium nanodroplet apparatus. The mass spectrometer chamber is on the left side and the source chamber on the right. All of the chambers are mounted on a bearing system to allow them to be separated for maintenance. The vacuum chambers downstream of the source chamber are also equipped with a baking system (hence the aluminium foil) to help improve the vacuum.

2.1.1 Helium nanodroplet source

The first step in forming helium nanodroplets is to pre-cool high-purity helium gas (99.9999%) using a closed-cycle cryostat (F-50, Sumitomo Heavy Industries). Helium nanodroplets are then formed by supersonic expansion of the pre-cooled helium through a pinhole nozzle. This pinhole is made from a Pt:Ir (95:5) electron microscope aperture (Günther Frey GmbH & Co. KG), which is a 5 mm diameter disk with a 5 μm circular orifice in the centre and a thickness of 0.2 mm. This disk is placed between a copper cylinder with a 1 mm diameter channel through its centre and a copper plate with a 0.5 mm diameter aperture and conical angle of 90° expanding outwards into the vacuum chamber. An indium sheet is used to provide a seal between the nozzle and the copper cylinder, thereby preventing escape of helium around the edges (see Figure 2.3). Once formed the helium nanodroplets are collimated into a beam by passage through a nickel skimmer with a 0.5 mm diameter aperture. The entire nozzle/cryostat assembly is mounted on an XYZ manipulator to allow the correct alignment with respect to the skimmer and to allow the nozzle-skimmer distance to be adjusted. The nozzle-skimmer distance is usually about 5-10 cm.

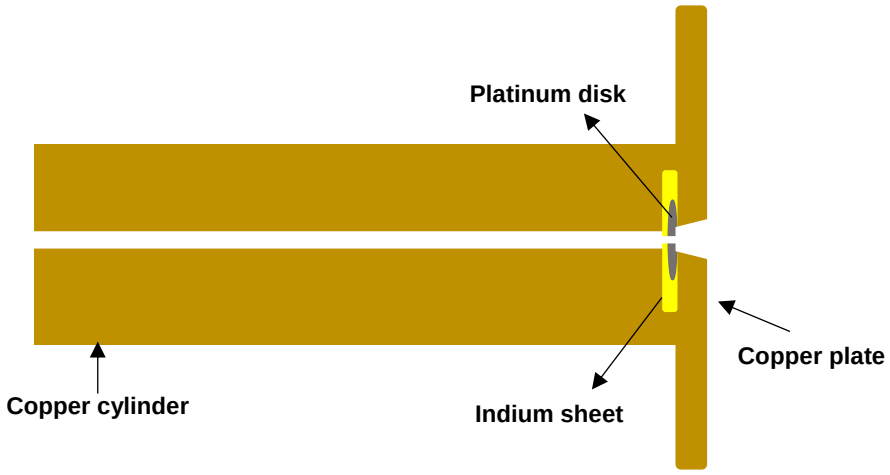

Figure 2.3. Cross-sectional schematic of the pinhole nozzle.

For the experiments in the current study we require helium nanodroplets consisting of a few thousand helium atoms (on average). To achieve this, the gaseous helium was pre-cooled to temperatures between 14 and 16 K. This steady-state temperature is maintained by a Lakeshore 336 controller, which supplies current to a heater placed behind the nozzle pinhole. The combination

of the cooling from the cryostat and the heating from the heater cartridge makes it possible to maintain a fixed temperature, which can be adjusted as needed. The stagnation pressure of the gaseous helium behind the nozzle in the experiments reported in this thesis was usually 30-33 bars.

The source chamber vacuum is maintained by two large turbomolecular pumps (Turbovac MAG W 2800, 2800 L/s each, Oerlikon-Leybold) backed by single roots pump (RUVAC 251, Oerlikon-Leybold), which in turn is backed by a large scroll pump (SCROLLVAC SC60 D, Oerlikon-Leybold). In total, the pumping speed is 5600 L/s.

2.1.2 Pick-up chamber

The helium nanodroplet beam is collimated by the first skimmer and enters the pick-up region. For the experiments described in this thesis two pick-up cells were used, one to add salt molecules to the nanodroplets and a second to add solvent molecules. These are described in the sub-sections below. The overall vacuum in the pick-up zone is provided by a 600 L/s turbo molecular pump (Leybold Turbovac MAG W 600 P), which is backed by a scroll pump (SCROLLVAC SC15 D, Oerlikon-Leybold or D-35614 Asslar, Pfeiffer Vacuum). This pumping system achieves a chamber base pressure in the region of 1×10^{-8} mbar, rising to 7×10^{-8} mbar when helium nanodroplets flow through this region.

2.1.2.1 *Salt pick-up cell (evaporation oven)*

To pick-up one or more molecules when the helium nanodroplets have a mean size in the region of a few thousand helium atoms, dopant pressures on the order of 10^{-6} to 10^{-5} mbar are required.[35] The first pick-up cell consists of an oven evaporator for heating solid samples to generate a significant vapour pressure. This heated pick-up cell was constructed from a high thermally conductive ceramic cylinder (FRIATEC Aktiengesellschaft/ Germany) whose dimensions are shown in Figure 2.4. The ceramic is alumina (Al_2O_3) (DEGUSSIT AL23). Helical grooves on the outside of the cylinder position a 0.8 mm diameter tantalum (Ta) heating wire. To prevent any electrical shock and to also minimize heat losses, the heating wire was covered by a thin layer of ceramic glue (Cotronics Corporation Co), which provides high electrical resistance, dielectric strength and

thermal conductivity to about 1600 °C. Also, both ends of the Ta wire which connect to the power supply are covered by ceramic paste. The chosen solid (in our case a salt) is placed within the alumina tube and the open ends are then closed by attaching ceramic wafers with a 6 mm hole in the centre to allow the helium nanodroplet beam to pass through. These ceramic wafers are press-fitted onto the open end of the cylinder host and held in place using the same ceramic paste that was used to cover the heating wire. A thermocouple wire (Type (C) tungsten/rhenium alloy) is attached to the outer surface of the cell which is capable of measuring temperatures up to and in excess of 2000 °C. Finally, to avoid increasing the temperature of other components inside the vacuum system, the entire oven is surrounded by water-cooled copper tubing. Under these conditions an oven temperature of more than 1600 °C can be achieved and this is sufficient to evaporate a wide range of salts.

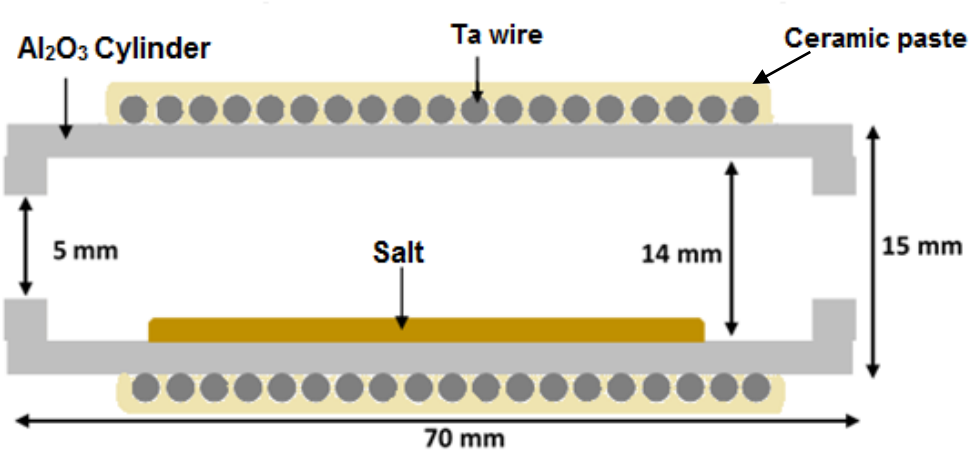

Figure 2.4. Schematic of the evaporation oven.

2.1.2.2 *Alkali halide evaporation process*

Several studies have dealt with the mechanism of alkali halide evaporation. Mellir and Ewing[83,84] pointed out that MX salt evaporation occurs via a two-step mechanism. The first step is the conversion from crystal to surface salt while the second step is the conversion from the surface state to the vapour. The monomer prevails at low temperature while, other species such as the dimer and trimer are dominant at high temperature. The evaporation of NaCl at the temperature used in this work (445 °C) has been found to produce monomeric NaCl almost exclusively in the vapour, with negligible production of NaCl dimer and atomic

sodium at this temperature.[67,85] On the other hand, the evaporation temperature of LiI was found to be 285 °C at which gave the maximum intensity of LiI^+ ion at 134 m/z. More details on the evaporation LiI will be discussed in Chapter Four.

2.1.2.3 *Solvent pick-up cell*

Solvent pick-up occurred in a second pick-up cell downstream of the salt pick-up cell. The design of this cell is quite different from that of the salt pick-up cell for two reasons. First, this cell is not heated. Second, the aim here was to provide solvent vapour at a carefully controlled and known pressure, in order that this pressure can be adjusted and used to confirm spectral assignments. To do this, a differentially-pumped pick-up cell was used.

The basic arrangement is shown in Figure 2.5. The cell is formed from a stainless steel 4-way KF cross. The long tube (shown as the larger diameter horizontal tube) spans the width of the vacuum chamber. On one side solvent vapour is bled in using a needle valve, while at the opposite end of the tube is a pressure sensor and a small turbo pump (Turbovac TMP 50, 50 L/s, Oerlikon-Leybold) backed by a small mechanical pump (SCROLLVAC SC15 D, Oerlikon-Leybold and D-35614 Asslar, Pfeiffer Vacuum). Perpendicular to this tube is narrower diameter tubing terminating in KF16 flanges. The open ends of this axis are closed by KF 16 caps with a 4 mm hole in the centre to allow the helium nanodroplet beam to pass through. These holes are sufficiently small such that an essentially constant pressure can be maintained inside the pick-up cell, i.e. there is no significant pumping effect from the larger turbo pump outside of the cell. In this way we can carefully control the dopant pressure inside this pick-up cell. The base pressure in the pick-up cell is about 1.7×10^{-6} mbar when the needle valve is closed, so all pressures of the dopant are quoted relative to this baseline value.

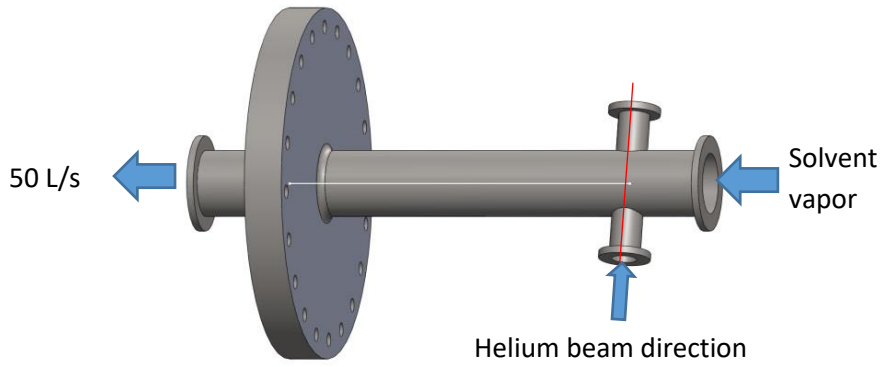

Figure 2.5. Schematic of the solvent pick-up cell.

2.1.3 Analysis chamber

A mass spectrometer is mounted vertically from the top of the last vacuum chamber. The mass spectrometer, which is described in more detail in the next section, serves several roles including as a diagnostic for helium nanodroplet formation. At the very end of the chamber is a quartz window, which allows a laser beam to be directed into the source region of the mass spectrometer for spectroscopic experiments. In fact, the laser beam can be directed further along the apparatus through a window in the gate valve, which makes it easy to align the laser beam along the path of the helium nanodroplets without having to vent the mass spectrometer vacuum chamber.

The vacuum in this chamber is provided by a 400 L/s turbomolecular pump (Leybold Turbovac MAG W 400 P backed by a SCROLLVAC SC15 D, Oerlikon-Leybold scroll pump). This pumping system achieves a chamber base pressure of about 1×10^{-9} mbar, rising to 7×10^{-9} mbar when the gate is open and exposed to the helium nanodroplet beam.

2.2 Mass spectrometry

Two types of mass spectrometers have been used in the work described in this thesis. Quadrupole mass spectrometry (QMS) was used for recording IR depletion spectra and will be briefly described in this section while a reflectron time-of-flight mass spectrometer (TOF-MS) was used for exploring the evaporation behaviour of salts and their ability to co-add a solvent (see separate details in Chapter Six).

The quadrupole mass spectrometer used in this work was an Extrel MAX 4000 model. This is equipped with an electron impact ionization source whose energy can easily be varied but is usually set between 60-100 eV, with an approximate resolution of 1 eV. After ionization the positive ions are drawn transversely into a quadrupole mass filter via deflection electrodes and focusing lenses. The highest detectable m/z ratio in the QMS is about 4000 and the mass resolution ($m/\Delta m$) is 1200.

The QMS can be operated in two modes. One option is the full scan mode, which simply records a mass spectrum over the range chosen by the user. However, for IR depletion spectroscopy a second mode is used, the single ion mass (SIM) scan. Here the quadrupole mass filter is set to transmit ions only in a very narrow mass range through to the detector. The choice of mode is set by the user via the Merlin (proprietary) software provided.

Note that there are other uses for the SIM mode in addition to the one given above. It can be used for aligning the helium nanodroplet beam by observing the dimer ion (He_2^+) signal while changing the expansion conditions. Also, the SIM mode can be used for optimizing the pick-up conditions, such as oven temperature and solvent partial pressure.

2.3 Optical parametric oscillator/amplifier (OPO/A) laser

A tunable infrared laser beam for spectroscopic experiments was provided by an optical parametric oscillator/amplifier (OPO/A) system (LaserVision). This system consists of two principal components, an optical parametric oscillator (OPO) and an optical parametric amplifier (OPA). The system produces an output that is tunable from 712 to 880 nm and from 1.35 to 5.0 μm.

The first optical parametric oscillator (OPO) was discovered by Giordmaine and Miller in 1965.[86] The underlying principle of the OPO is a nonlinear interaction between optical radiation and certain types of crystal: this effect is only noticeable at the very high light intensities available from lasers. Basically, an OPO converts a fraction of the input (pump) laser beam (frequency ω_p) into two output beams of lower frequencies by means of a nonlinear interaction between the dielectric polarization of the crystalline medium and the electric field of the light. The output

beam with the higher frequency is called the ***signal beam*** (ω_s) while the second beam is called the ***idler*** (ω_i). By conservation of energy we have:

$$(\omega_p) = (\omega_s) + (\omega_i) \qquad [3]$$

For the LaserVision system the pump beam is the 532 nm output from an Nd:YAG laser (Continuum Surelite II-10). This 532 nm beam derives from the 1064 nm fundamental output of the Nd:YAG laser and is obtained by frequency doubling inside the OPO system. The 1064 nm beam from this laser (up to a maximum input pulse energy of 585 mJ) is directed into the OPO/A system at a repetition rate of 10 Hz with pulses of approximately 5 ns duration. The 1064 nm beam is divided into two pathways, as can be seen in Figure 2.6.

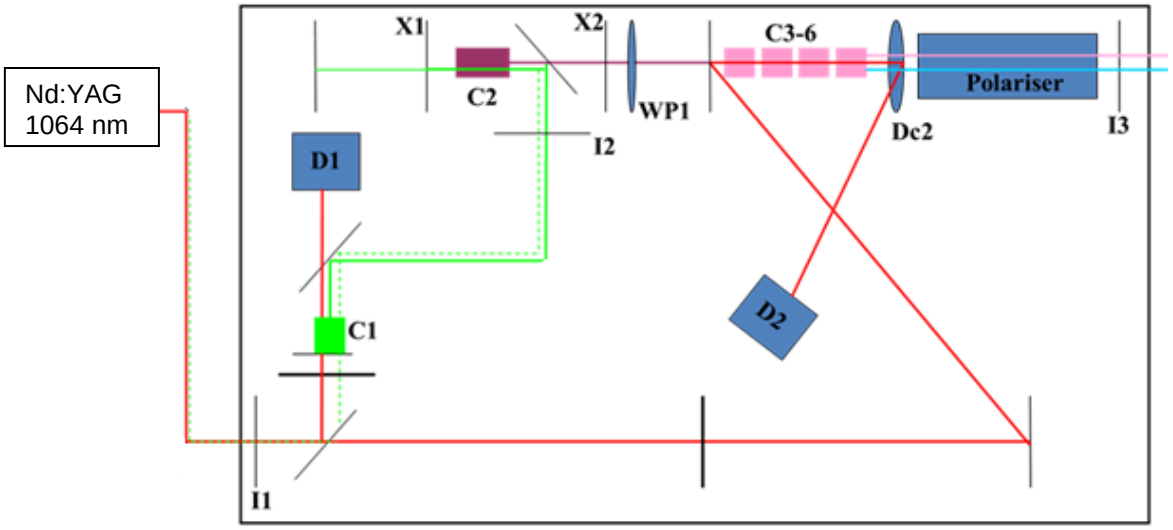

Figure 2.6. Schematic of the OPO/OPA laser.

One part of the 1064 nm beam enters the OPO part of the laser. As mentioned above, here the beam is frequency doubled from 1064 to 532 nm using a KTP crystal (C1). The residual of this portion of the 1064 nm beam after the doubling is dumped at D1 while the green 532 nm beam is then steered into the oscillator cavity (Rear Mirror X1 and Output Coupler X2), which contains a second KTP crystal (C2). The oscillator cavity generates radiation at two different frequencies through an optical parametric process to produce the signal and idler waves. The signal wave is horizontally polarized while the idler is vertically polarized. The

polarizations of the signal and idler are then flipped using a half-wave plate (WP1). The use of WP1 is to rotate the seed beam polarization and permits the 1064 nm OPA crystals to be angle-turned in the horizontal, rather than the vertical, plane before entering the OPA stage of the laser.

In the second stage, the OPA, two further signal and idler waves are generated by mixing the rest of the pump 1064 nm beam with the idler output from the OPO stage. Both beams are then passed through four KTA (C3-6) crystals for amplifying the signal and idler energy and then onwards into a dichroic mirror (Dc2), which removes any residual 1064 nm pump from the co-propagating signal and idler waves. The second part of the OPA stage acts as an amplifier for the signal and idler. The signal is horizontally polarized while the idler is vertically polarized. Before the signal and idler pass from the laser housing, the polarizer will dictate which one will pass out of the system (but not both), depending on the orientation of the polarizer.

The laser beam is then steered into the helium nanodroplet apparatus chambers using two mirrors. Before the apparatus, two irises are used to control the laser beam alignment. The laser beam travels from the OPO/A system to the apparatus through an air-purging system which consist of 1.4 m plastic tube containing pure N_2 gas. This purged optical path is used to reduce absorption by gases in air. To achieve the maximal overlap of the laser light with the helium nanodroplet beam, a concave lens is used to gently focus the laser beam.

2.4 Depletion spectroscopy

Optical spectra of molecules and complexes in helium nanodroplets are often extracted using the technique of depletion spectroscopy. The basic principles of the technique were described in section 1.4. Briefly, the output beam from the OPO/A enters the helium nanodroplet apparatus from the end opposite to the helium nanodroplet source. The laser beam therefore travels in a counter-propagating fashion to the nanodroplet beam. It is important to try and achieve maximum overlap of the two beams (Figure 2.7 (a)). This overlap can be achieved using two irises and one concave lens (Melles Griot Co) with a 100 cm

focal length to concentrate the laser power to a focal point in front of the second pick-up cell.

The picked up dopants (Figure 2.7 (b)) can be excited by absorbing energy from the laser, providing the right frequency is selected. Resonant absorption of a photon will cause the droplets to shrink by losing (typically) several hundred helium atoms (Figure 2.7 (c)). The decrease in the droplet size will reduce the electron-impact cross section for ionization, causing a significant drop in the mass spectrometer signal at resonance (Figure 2.7 (d)): this process is called depletion.[64] Thus a depleted ion signal is recorded when the laser achieves resonance. A typical level of signal depletion is a few % and the process is illustrated in Figure 2.7.

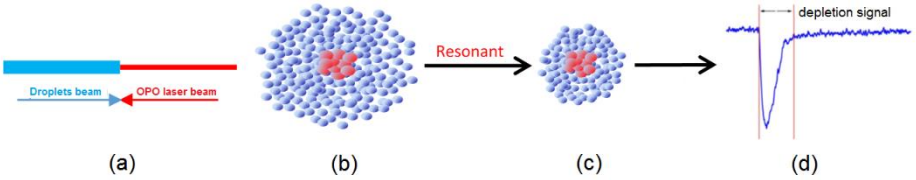

Figure 2.7. Schematic of optical depletion process for a doped helium droplet. (a) Laser beam and molecule bean overlap. (b) Helium droplets picked up dopants. (c) Resonant absorption cause the droplets to shrink. (d) Depletion signal during resonance.

2.5 Computational chemistry calculations

Ab initio calculations were used to support the results by predicting possible structures of MX(solvent)$_n$ complexes and their corresponding IR spectra. A high level of theory, second order Møller-Plesset perturbation theory (MP2), was used to identify the structures of the studied complexes. Also, the accuracy of the basis sets were increased gradually to predict the possible structures. This level of theory was used to explore the structures of LiI complexes with water and methanol. The details of these calculations are explained in sections 4.3 and 5.3. In case of the calculations of NaCl(CH_3OH)$_n$ complexes in Chapter Three, the predicted spectra at the MP2 level of theory did not agree very well with experiments. Therefore, density functional theory DFT was used as an alternative theory to support the result of these complexes. DFT theory showed better correlation with the experimental spectra than MP2 theory due to the differences

in scaling factors. The details of the *ab initio* calculations of $NaCl(CH_3OH)_n$ complexes is discussed in section 3.3.

2.6 Data acquisition and processing

Proprietary software (Merlin Automation, version 4.0) is used to control the QMS and monitor the mass-resolved ion signal. For recording IR depletion spectra, the QMS software is used in combination with a program written in LabVIEW (version 2015) that scans the OPO/A wavelength and reads the ion signal accumulated by a photon counter (SRS Model SR400).

Once the QMS is set to monitor the ion signal of interest the IR depletion signal is collected in the following way. The internal system timer of the digital delay generator (BNC Model 555) generates the starting pulse, T_0, every 100 ms (10 Hz). Three channels on the delay generator are then used to provide trigger pulses to the Nd:YAG pump laser and the photon counter. Channel A triggers the flashlamps in the Nd:YAG laser at a delay time of 4.242 ms relative to T_0, whilst channel B triggers the opening of the Nd:YAG laser Q-switch after a further delay of 0.203 ms; this generates a nanosecond laser pulse, Figure. 2.8(a). Channel C triggers the photon counter at a delay time of 0.01 ms relative to T_0. The photon counter also receives an input signal from the QMS ion detector and uses two independent channels (1 and 2), set by the internal trigger of the photon counter, to count the number of ions that arrive during a selected time interval after the trigger from Channel C, as illustrated in Figure. 2.8(b). Channel 1 on the photon counter is used to accumulate the ion signal from target molecules that are temporally overlapped with the laser pulse inside the spectrometer chamber (laser ON). The optimum delay time and width for this channel were determined to be 5.1 ms and 1.0 ms, respectively. Channel 2 on the photon counter measures the ion signal generated in the absence of a laser pulse (laser OFF). The respective ion signals are accumulated by the photon counter after 400 laser shots, which corresponds to a time period of 40 s. This long accumulation time was chosen in order to achieve a suitable signal/noise ratio and to account for slowly varying fluctuations in the ion signal.

When recording the IR depletion spectrum, the LabVIEW program sends a command to the OPO/A to scan the wavelength over a specific range and at a chosen scan rate. The LabVIEW program reads the values from both channels on the photon counter as well as the OPO/A wavelength. This process is repeated until the laser reaches the end of the specified wavelength range. The depletion signal, which is the difference between values recorded on the two channels of the photon counter, is then calculated as a function of the laser wavelength.

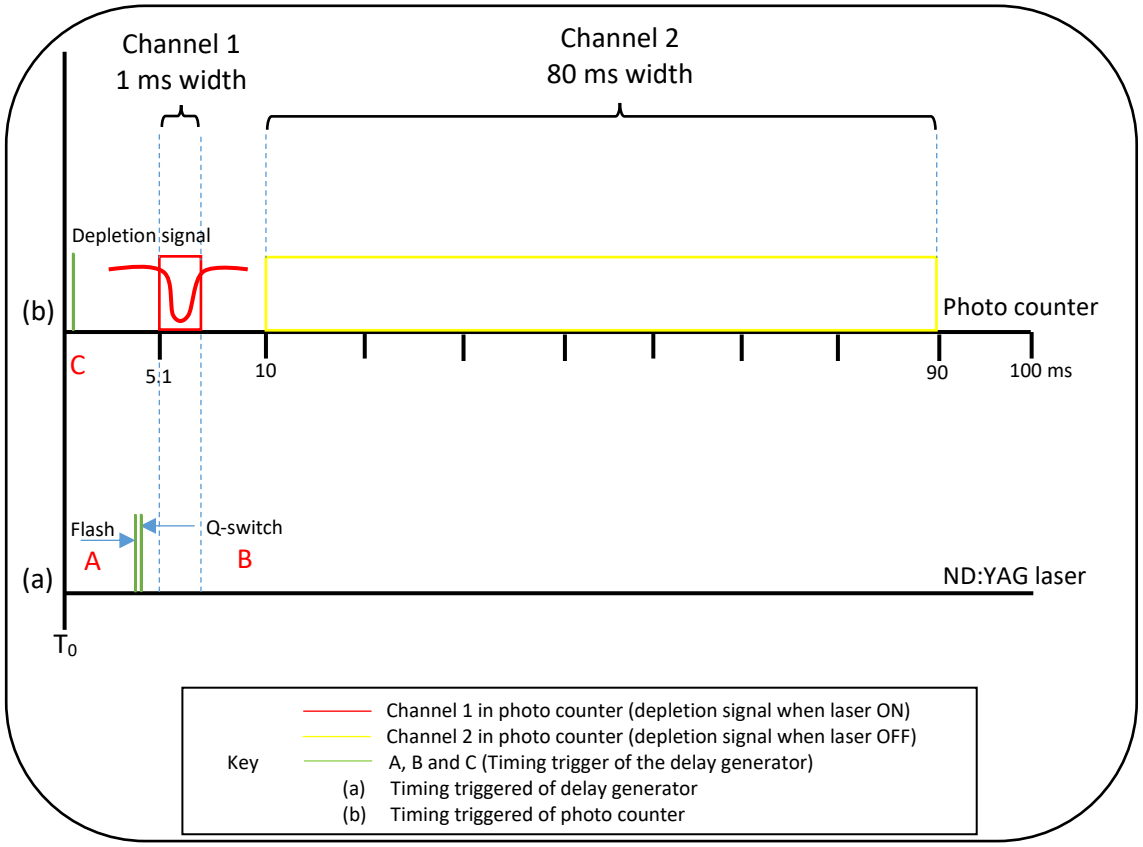

Figure 2.8. Illustrative experimental timing diagram.

CHAPTER 3

Infrared Spectroscopy of $NaCl(CH_3OH)_n$ Complexes in Helium Nanoroplets

3.1 Introduction

In solid, alkali halides have a crystalline structure which, when placed in a solution, is disrupted by polar solvents (such as water) and the solid dissolves to produce separated ion-pairs, in dilute solutions. The solubility of these salts in water is extremely high. However, the solubility of alkali halides in other polar protic solvents, such as methanol, is much lower than in water. [87, 88] The main reason for the reduced solubility of salts in methanol and other alcohols, compared with water, is related to the hydrophobic alkyl group(s).

In bulk solutions there have been some investigations of possible structures that occur when alkali halides are dissolved in an alcohol. For example, Bowron and Finney [89] applied neutron scattering measurements to a solution of NaCl in *t*-butanol. The data suggest that the linkage between NaCl and *t*-butanol consists of an ionic hydrogen bond (IHBs) between the halide atom and the OH group of alcohol molecules. On the other hand, Paschek *et al*.[90] have rejected the conclusion of IHBs and presented experimental and theoretical evidence for a different type of interaction between NaCl and *t*-butanol in which a halide ion attaches to the methyl groups in *t*-butanol. If correct, this linkage will increase the attractive interactions between the hydrophobic methyl groups in other *t*-butanol molecules.

There have been several spectroscopic investigations of $NaCl(H_2O)_n$ complexes, which were summarised in Chapter One.[67,80-82] The aim of such studies is to learn more about the way salt molecules interact with water molecules and to learn about the transition from simple complexes to a fully solvated system. By working with finite-sized systems one can also readily bring *ab initio* electronic structure calculations into the investigation to supplement the experimental work.

Given the recent success in looking at $NaCl(H_2O)_n$ complexes, a natural extension is to replace the water molecules with methanol. This will allow the effect of the amphiphilic character of methanol on its interaction with NaCl to be explored. As will be discussed below, the resulting data are consistent with the formation of contact ion-pair structures in which several methanol molecules can bind to a neutral NaCl molecule via IHBs between the OH groups and the chloride ion. These structures are similar to the salt-bridge structures mentioned in the previous paragraph.[89] The experimental work has been supported using quantum chemical calculations to explore the structure of the complexes for $n \leq 4$.

3.2 Experimental

The experimental apparatus was described in detail in Chapter Two of this thesis. In brief, helium nanodroplets were formed by expanding pre-cooled high purity helium gas at a stagnation pressure of 33 bar and a temperature of 16 K through a small aperture (5 μm) into a vacuum. The mean size of the nanodroplets is expected to be close to 5500 helium atoms under these expansion conditions. After passing through a skimmer, the nanodroplet beam then sequentially travels through two pick-up cells: the first contained NaCl vapour and the second methanol vapour. NaCl vapour was produced by resistively heating a pick-up cell containing solid sodium chloride (99.9999 %, Fisher Scientific) to a temperature of 445°C. The methanol (99.999 %, Sigma-Aldrich) was degassed using the freeze-pump-thaw technique. This entailed freezing the solvent using liquid nitrogen and then pumping off residual gases for 10 minutes. This process was repeated three times before starting each experiment. Methanol was placed in an ice bath during the experiment to lower the vapour pressure and was then delivered into the second pick-up cell via a needle valve. The partial pressure in the pickup cell was around 2×10^{-6} mbar before the addition of methanol and increased gradually with increased methanol vapour pressure. Under these conditions, small $NaCl(CH_3OH)_n$ complexes can be formed and conditions can be optimized to favour a specific complex by adjusting the partial pressures of the two dopants. However, in helium nanodroplets a distribution of cluster/complex

sizes always occurs because of the statistical nature of the pickup process, so full selectivity by pressure control is not achieved.

IR spectra were recorded via a depletion technique. This technique depends on recording the reduction of the mass signal of complex ion, as a result of IR absorption, and was fully detailed in section 2.4.

3.3 Computational details

Theoretical support for this work was provided by Magnus Hanson-Heine and Nicholas A. Besley at the University of Nottingham. *Ab initio* calculations were performed on $NaCl(CH_3OH)_n$ for n = 1- 4 using the Q-Chem software package.[91] Density functional theory (DFT) with the M06 functional[92] was used to search for optimized geometries. Fifty different initial configurations were generated by rotating the methanol molecules randomly around the NaCl ion-pair in order to scan a wide range of potential geometries.

The initial configurations for the n = 1 and 2 complexes were optimized at the M06/6-311++G(d,p) level of theory. For the n = 3 and 4 complexes, the initial configurations were optimized at the M06/6-31++G level of theory. All optimized structures within 0.5 eV of the minimum energy structure were then re-optimized with the larger 6-311++G(d,p) basis set.

Vibrational frequencies were calculated assuming the harmonic approximation. To achieve realistic agreement with experiment, a scaling factor is needed to account for vibrational anharmonicity. Instead of using a standard scaling factor, the scaling factor employed was derived from actual anharmonic vibrational frequency calculations of OH stretching modes of the $NaCl(CH_3OH)_n$ complexes. The anharmonic vibrational frequencies for $NaCl(CH_3OH)_n$ (n = 1 and 2) complexes were calculated using second-order vibrational perturbation theory (VPT2), in addition to using the transition optimized shifted Hermite (TOSH) variation on VPT2.[93] When compared with the calculated harmonic vibrational frequencies the average of more than three vibrational modes and the two methods gave a scaling factor of 0.924, which was then applied to the harmonic frequencies. The value of 0.924 is lower than most typical scaling factors [93] and suggests that the OH stretching mode in $NaCl(CH_3OH)_n$ complexes has a high

degree of anharmonicity, which may be a consequence of the ionic hydrogen bonding.

3.4 Results and Discussion

3.4.1 Overview of the experimental results

A mass spectrum recorded from the $NaCl(CH_3OH)_n$ experiments can be seen in Figure 3.1. Three series of peaks are observed in this spectrum. One series derives from He_n^+ cluster ions, which can be seen across the mass spectrum but which are particularly noticeable at *m*/*z* values < 120. These peaks are not labelled in Figure 3.1 but give rise to a series of peaks separated by 4 mass units. Of the two highlighted series, one is assigned to $(CH_3OH)_mH^+$ and the other to $(CH_3OH)_mNa^+$. The $(CH_3OH)_mH^+$ ions derive from ionization of methanol clusters within helium nanodroplets while the $(CH_3OH)_mNa^+$ ions are the products of ionization of $NaCl(CH_3OH)_n$ complexes in these nanodroplets. We do not see any intact $[NaCl(CH_3OH)_n]^+$ ions, i.e. loss of a Cl atom on ionization must be facile. This behaviour is analogous to that seen in the ionization of $NaCl(H_2O)_n$ complexes in helium nanodroplets. [67]

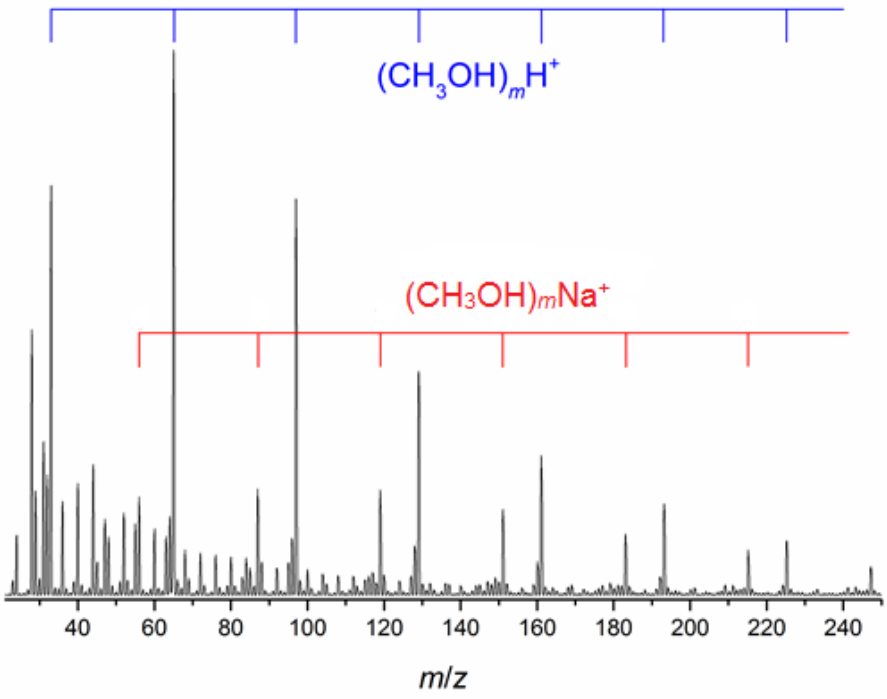

Figure 3.1. Mass spectrum from the $NaCl/CH_3OH$ system obtained using an electron energy of 70 eV.

IR spectra were recorded using the depletion technique by detecting specific $(CH_3OH)_mNa^+$ ions. The resulting spectra are shown in Figure 3.2. Before going into more detail later, some general comments are required here. Figures 3.2 (a), (b) and (c) show IR spectra recorded by detecting ions with m = 1, 2 and 3, respectively. Peaks are seen in both the OH stretching region (>3000 cm^{-1}) and the CH stretching region (<3000 cm^{-1}). Some relatively sharp peaks can be seen in the OH stretching region for m = 1 – 3. However, the OH stretching region for m = 4, which is shown in Figure 3.2 (d), is very broad with no obvious structure and which reaches a maximum near 3300 cm^{-1}. Beneath each spectrum for m = 1- 4 are the predicted IR spectra from DFT calculations assuming the value of m in the $(CH_3OH)_mNa^+$ ions matches the solvation number in the corresponding neutral complex, $NaCl(CH_3OH)_n$, *i.e*. assuming $n = m$. Later in this chapter we will discuss specific band assignments and the validity of these assumptions.

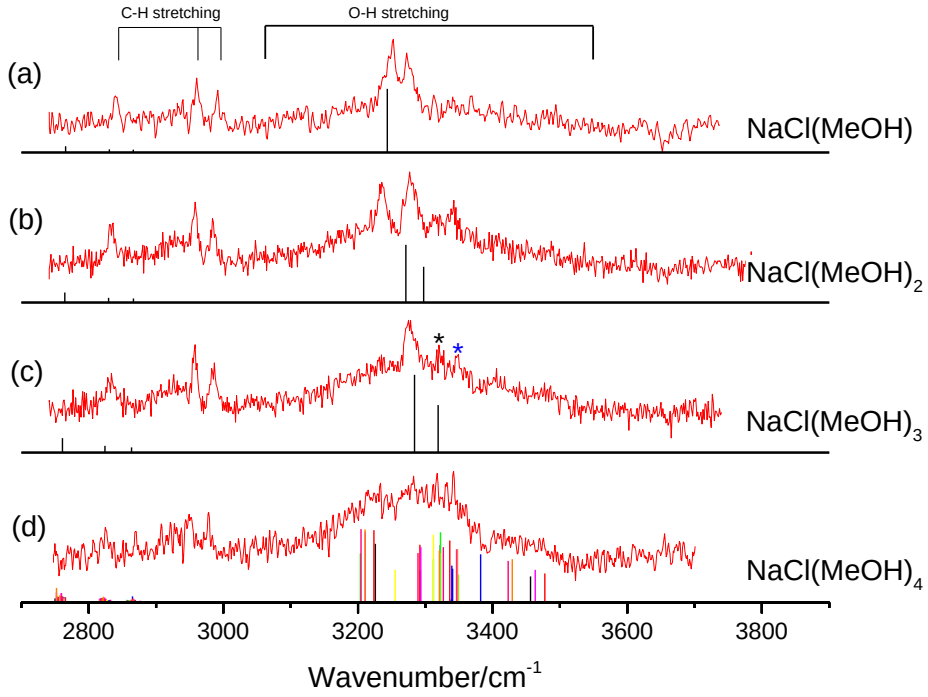

Figure 3.2. Infrared spectra of $NaCl(CH_3OH)_n$ recorded by monitoring ion signals at (a) m/z 55 ($Na^+(CH_3OH)$) (b) m/z 87 ($Na^+(CH_3OH)_2$), (c) m/z 109 ($Na^+(CH_3OH)_3$) and (d) m/z 141 ($Na^+(CH_3OH)_4$). Also shown are the theoretical IR spectra for the complexes shown on the right of the figure. For n=1-3 only the vibrational lines from the global minimum energy structure are shown while the transitions from global and all calculated local minima are shown for n=4. The black and blue asterisks are weak absorption bands (see later).

3.4.2 Predicted structures

The DFT calculations found four structures corresponding to potential energy minima for the NaCl(CH_3OH) complex, all of which are shown in Figure 3.3. In the global minimum, the NaCl ion-pair is positioned such that the chloride ion can form an (IHB) with the OH on the methanol, while additional stabilization is achieved by the close distance between the Na^+ ion and the O atom. This structure is similar to that reported previously for the global minimum energy structure of NaCl(H_2O). [67,82] In the next lowest energy structure, one of the C-H bonds is oriented towards the chloride ion while the Na^+ interacts with the O atom of the methanol. This structure has an energy about 0.11 eV higher than the global minimum. The other two isomers have only one hydrogen bond between methanol and NaCl and have relative energies of 0.21 and 0.71 eV.

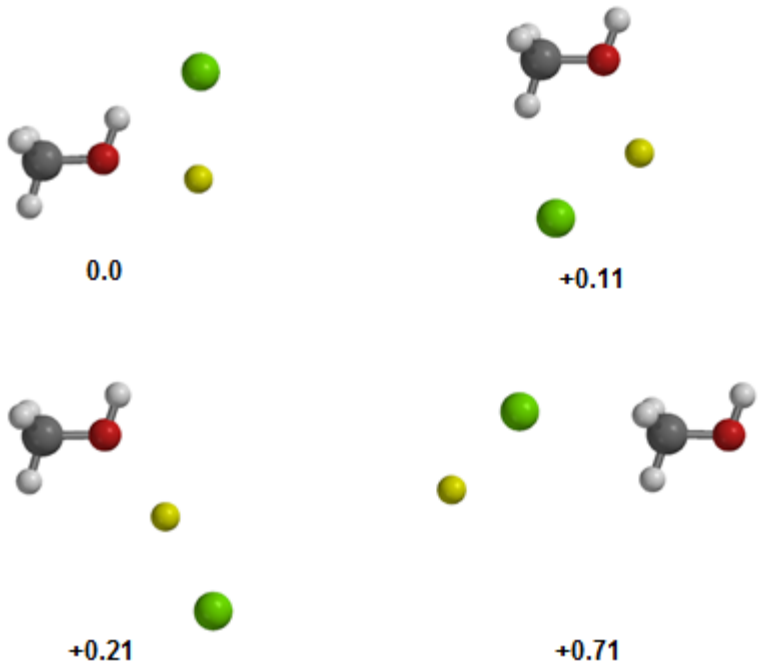

Figure 3.3. Calculated equilibrium structures of NaCl(CH_3OH) along with their energies (not corrected for zero point energy) in eV relative to the global potential energy minimum.

For NaCl$(CH_3OH)_2$, the calculations revealed five distinct minima, as can be seen in Figure 3.4. The lowest energy structure for the *n* = 2 complex has two IHBs linking the chloride ion and the OH groups. The next lowest energy minimum has an energy of only 0.03 eV above the global minimum and has two distinct bonding

modes. One of the methanol molecules is attached to the NaCl in a similar manner to the global minimum. However, the other methanol molecule has a slightly different orientation so that it can form a partial ionic hydrogen bond to the chloride ion and also with the CH bonds from the methyl group. The OH and methyl groups in the other minima have different orientations. The highest energy structure lies 0.15 eV above the global minimum structure.

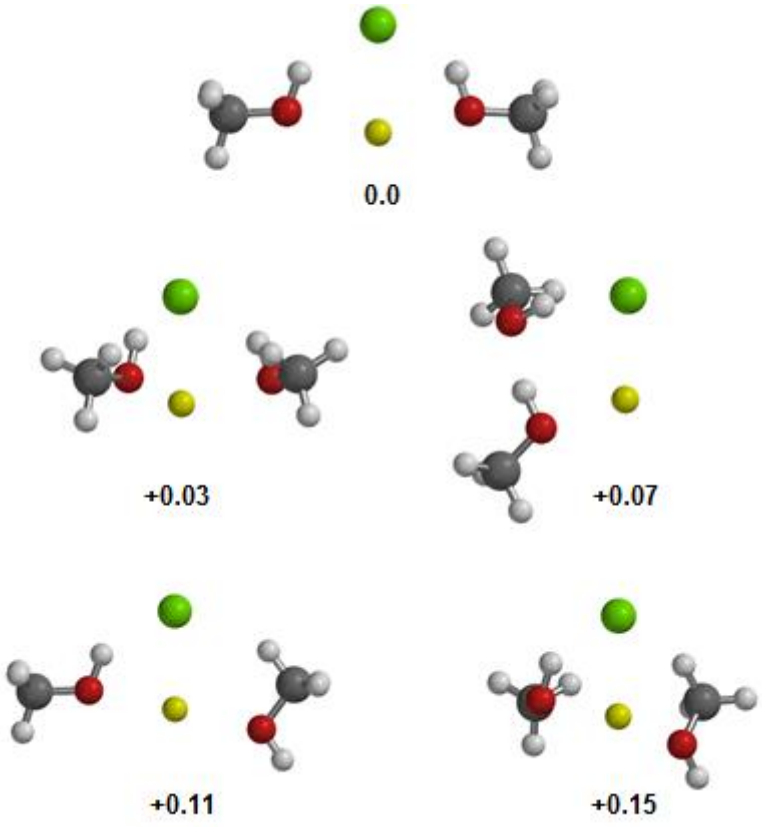

Figure 3.4. Calculated structures of $NaCl(CH_3OH)_2$ along with their energies (not corrected for zero point energy) in eV relative to the global potential energy minimum.

Prediction of the structures of n = 3 and 4 complexes provided more of a challenge. The global minimum for $NaCl(CH_3OH)_3$ is similar to those found for $NaCl(CH_3OH)$ and $NaCl(CH_3OH)_2$, but now with three equivalent IHBs (see Figure 3.5). The other structures have different positions of the OH and CH_3 groups and the highest energy structure lies 0.17 eV above the global minimum. For $NaCl(CH_3OH)_4$, the lowest energy structure has three IHBs linking the chloride ion and the OH groups, while the fourth methanol is effectively in a

second solvation shell and is hydrogen-bonded to one of the methanol molecules in the inner solvation shell (see Figure 3.6). However, nine different structures have been found for $NaCl(CH_3OH)_4$, which obviously makes for a more complicated potential energy landscape.

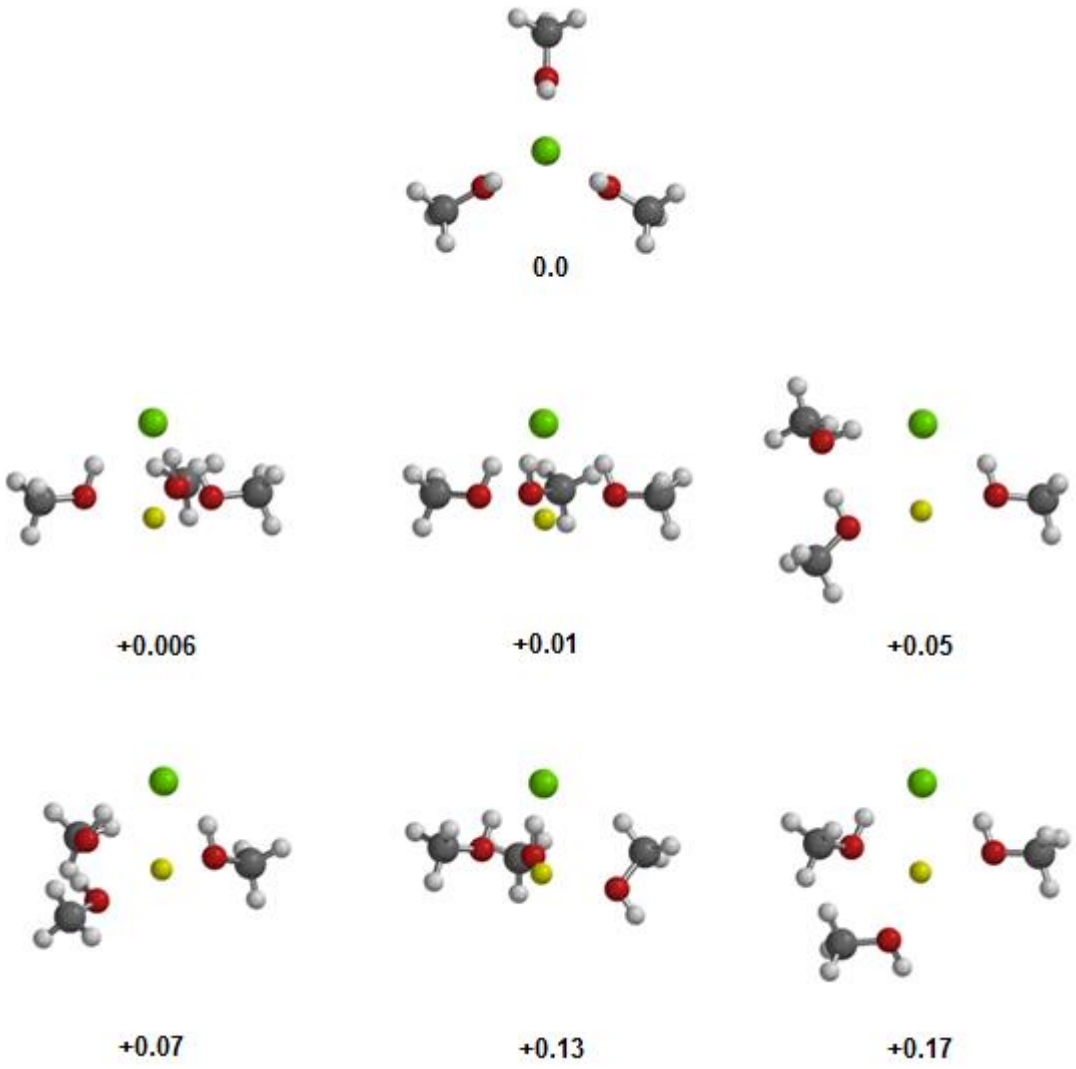

Figure 3.5. Calculated structures of $NaCl(CH_3OH)_3$ along with their total energies (not corrected for zero point energy) in eV relative to the global potential energy minimum.

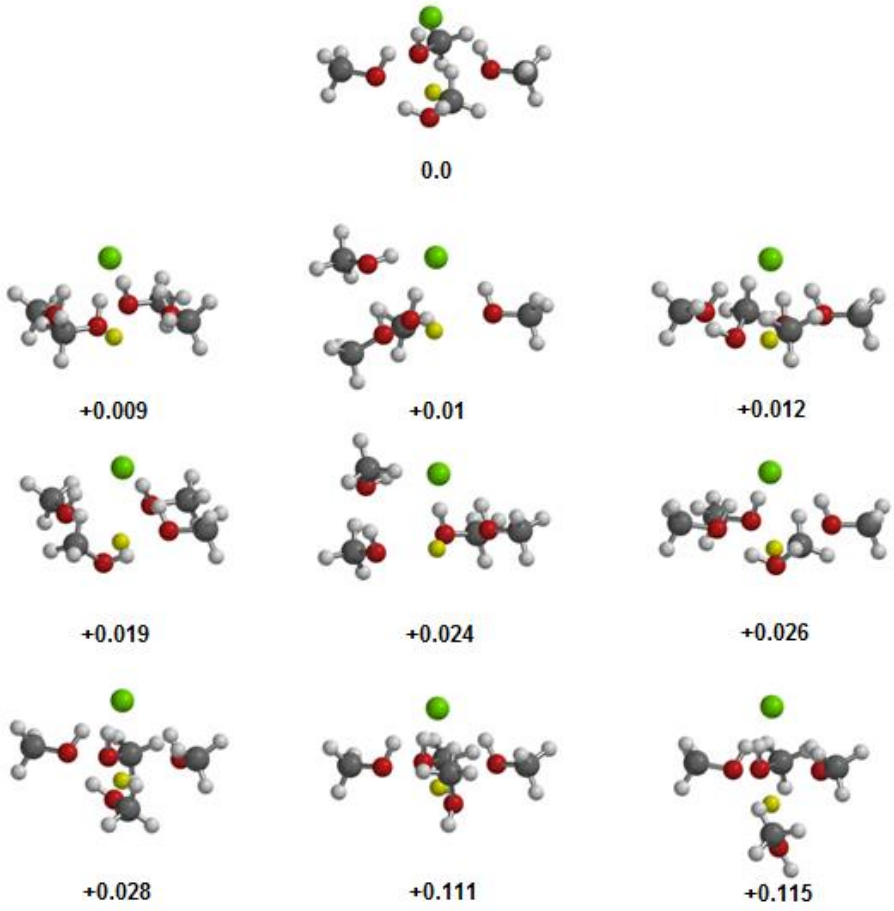

Figure 3.6. Calculated structures of $NaCl(CH_3OH)_4$ along with their energies (not corrected for zero point energy) in eV relative to the global potential energy minimum.

3.4.3 Assignment of IR spectra: OH stretching region

Several bands in the OH stretching region can be seen in Figure 3.2. Although mass-selective detection of ions has been applied to record the IR depletion spectra, this technique does not guarantee that the spectrum derives from a single neutral complex. The reason for this is that fragmentation, by the loss of one or more methanol molecules, might occur when ionization takes place, and thus the same absorption band might be in the spectra from different mass channels. However, mass selectivity can unambiguously identify the *minimum* number of methanol molecules in the complex or complexes contributing to a specific IR spectrum.

Important information on band assignment can also be obtained from the dependence of the IR signal on the methanol pick-up pressure, as was done

previously for $NaCl(H_2O)_n$.[67] Figure 3.7 shows pick-up pressure (PUCP) data for $NaCl(CH_3OH)_n$. Also shown are Poisson curves for different values of *n* which reflect the probability of picking up *n* dopant molecules in the limit of negligible droplet shrinkage after pick-up. Unfortunately, the PUCP measurements for $NaCl(CH_3OH)_n$ are not as useful as they were for $NaCl(H_2O)_n$ for two reasons. Firstly, there are obvious overlapping bands for different sized complexes, as can be seen clearly by looking at Figures 3.2(a), (b), (c) and (d), where peaks are seen at similar positions in different mass channels. Secondly, the relatively narrow OH stretching bands have a broad underlying absorption feature, which is most likely related to complexes that have relatively large values of *n* (≥ 4). This underlying broad absorption is very obvious in the IR spectra recorded in the $(CH_3OH)_2Na^+$ and $(CH_3OH)_3Na^+$ mass channels. Indeed there is even some hint of a contribution in the $(CH_3OH)Na^+$ channel. This issue of the broad absorption can be partially offset by estimating and subtracting its contribution from the intensities of the narrower peaks as the methanol partial pressure is changed. However, the overlapping of the sharper bands is a more serious problem and thereby reduces the ability to gain assignment information from the PUCP data.

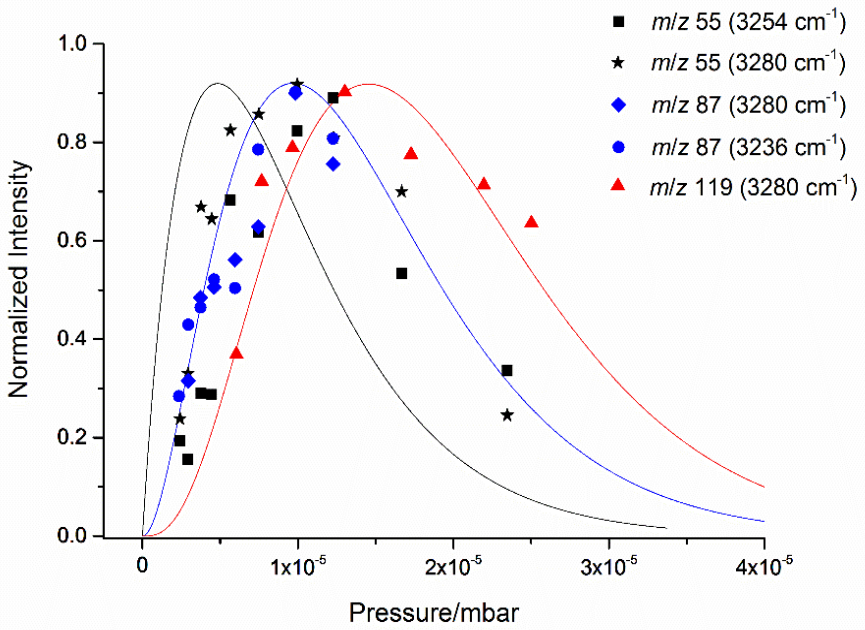

Figure 3.7. Dependence of the IR absorption band intensities on the partial pressure of methanol in the second pick-up cell detected in the *m/z* 55 ($(CH_3OH)Na^+$), *m/z* 87 ($(CH_3OH)_2Na^+$), and *m/z* 119 ($(CH_3OH)_3Na^+$) mass channels. Calculated Poisson curves for the pick-up of one (black), two (blue), and three (red) methanol molecules are also given.

Before starting to make specific assignments, the positions of the sharp bands seen in the OH stretching region are summarized in Table 3.1. All of these bands lie between 3230 and 3360 cm^{-1}, which is a relatively narrow range. These frequencies are strongly red-shifted from the single OH stretching band at 3685 cm^{-1} of the methanol molecule in superfluid helium.[94] The main reason for this red shift is thought to be the formation of ionic hydrogen bonds, which weaken the OH bonds and thereby lower the OH stretching frequencies. It is useful to compare this observation with an IR study by Lisy and co-workers in the gas phase for the anionic complexes $Cl^-(CH_3OH)_n$.[95, 96] In this study two distinct structures for n = 2 were identified from the IR spectra. In the first one, each methanol molecule is bound to Cl^- by an ionic hydrogen bond. For the second structure a methanol dimer binds to Cl^- by an IHB and then the second methanol molecule binds to the first by a normal hydrogen bond. The latter structure has an IHB which caused an exceptionally strongly red-shifted band for this OH group, giving an absorption band at 2773 cm^{-1}. No comparably large red-shift was seen in the region of 2750 to 3700 cm^{-1} in this work. We therefore conclude that there is no methanol-methanol hydrogen bonding in small $NaCl(CH_3OH)_n$ clusters. This difference between $Cl^-(CH_3OH)_n$ and $NaCl(CH_3OH)_n$ probably comes from the additional electrostatic stabilization provided between Na^+ and the O atom on methanol when an IHB forms between OH and the chloride ion in NaCl (for example see the global energy minimum structure for $NaCl(CH_3OH)$ in Figure 3.3). Structures with the maximum number of IHBs will be energetically favoured for small values of n.

Table 3.1. Positions and assignments of OH stretching bands for $NaCl(CH_3OH)_n$ for n = 1-3.

Band position/cm^{-1}	Assigned carrier
3236	$NaCl(CH_3OH)_2$
3254	$NaCl(CH_3OH)$
3278	$NaCl(CH_3OH)_2$ + $NaCl(CH_3OH)_3$
3323	$NaCl(CH_3OH)_3$?
3344	$NaCl(CH_3OH)_3$?

3.4.3.1 *Assignment of $NaCl(CH_3OH)$*

The assignment process can begin by looking for the IR spectrum of the smallest complex, $NaCl(CH_3OH)$. Taking into account possible ion fragmentation, the spectrum of this complex might be observable as signal depletion in the Na^+ or $(CH_3OH)Na^+$ mass channels. Previously, the IR spectrum of $NaCl(H_2O)$ was recorded by our group by detecting Na^+. [67] However, when H_2O is replaced by CH_3OH, there were no OH stretching bands seen when searching for depletion in the Na^+ mass channel. It is therefore reasonable to conclude that ionization of $NaCl(CH_3OH)$ in a helium nanodroplet leads to ejection of Cl but is not accompanied by loss of CH_3OH. Consequently, the IR spectrum of $NaCl(CH_3OH)$ must be contained within the spectrum recorded in the $(CH_3OH)Na^+$ channel, which is shown in Figure 3.2(a). This spectrum shows two partly overlapping bands, one peaking at 3254 cm^{-1} and the other at 3271 cm^{-1}. The band at 3254 cm^{-1} is unique because it has no exact counterpart in spectra from higher mass channels in Figure 3.2, although it does partly overlap with a peak whose maximum is at 3236 cm^{-1} in the $(CH_3OH)_2Na^+$ channel. The 3254 cm^{-1} band is Therefore assigned to $NaCl(CH_3OH)$. Note that the PUCP curve for this band in Figure 3.7 does not entirely support this assignment, since it shows a pressure-dependence that is more related to n = 2 than n = 1. However, the underlying broad absorption envelope may distort this curve and therefore the PUCP must be taken as indicative only.

The band at 3271 cm^{-1} in the $(CH_3OH)Na^+$ mass channel is close to a band seen at 3278 cm^{-1} in both the $(CH_3OH)_2Na^+$ and $(CH_3OH)_3Na^+$ mass channels. It is therefore possible that the 3271 cm^{-1} band in the $(CH_3OH)Na^+$ channel is wholly or partly a contribution from $NaCl(CH_3OH)_2$ or a larger complex.

The simulation of the IR spectrum derived from DFT calculations for the global minimum energy isomer for $NaCl(CH_3OH)$ is shown beneath the experimental spectrum in Figure 3.2(a). Several OH stretching bands are expected if many isomers are present in helium nanodroplets. However, since only one OH stretching band is identified as arising from $NaCl(CH_3OH)$, only one isomer is present in helium nanodroplets. The band in the IR spectrum of $NaCl(CH_3OH)$ was red-shifted by ~430 cm^{-1} from the OH stretching band of the methanol

monomer in superfluid helium,[94] which means that there is a very significant weakening of the O-H bond when methanol forms a complex with NaCl. A previous study of the anionic complex $(CH_3OH)Cl^-$ found that formation of an (IHB) between the OH and the chloride ion results in a red shift for the OH absorption of 519 cm^{-1}.[96] The smaller red-shift seen for $NaCl(CH_3OH)$ compared with the anion is reasonable for two reasons. First, the negative charge on the chloride ion in NaCl is expected to be smaller than for bare Cl^-, making the IHB weaker. Second, interaction between the Na^+ and the O atom is also likely to affect the strength of the IHB.

There is close agreement between the experimental band position and the DFT calculation for the global minimum isomer of $NaCl(CH_3OH)$ in Figure 3.2(a) (the difference is 10 cm^{-1}). This provides additional support for the assignment of the $NaCl(CH_3OH)$ absorption band. Note that, in addition to the experimental argument made above, there are other reasons to suspect a contribution from only one isomer of $NaCl(CH_3OH)$. Firstly, other isomers of $NaCl(CH_3OH)$ have a much higher energy than the global minimum energy structure. Secondly, the other isomers do not have IHBs and therefore, their OH stretching bands will be observed at much higher frequencies than the global minimum structure.

3.4.3.2 *Assignment of $NaCl(CH_3OH)_2$*

The DFT calculations for $NaCl(CH_3OH)_2$ predict a global minimum structure in which each methanol molecule is bonded to the NaCl independently in a symmetrical configuration which involves two IHBs. Therefore, two absorption bands should be seen for the symmetric and antisymmetric combinations of the two OH stretching vibrations. The formation of two IHBs with Cl^- is expected to lead to a weakening in each individual IHB when compared to $NaCl(CH_3OH)$, as a result of sharing of the negative charge on the chloride ion between the two OH groups. Consequently, the O-H bonds in $NaCl(CH_3OH)_2$ complexes will be stronger and so a smaller red-shift for the OH stretches is expected compared with $NaCl(CH_3OH)$. The IR spectrum in the $(CH_3OH)_2Na^+$ mass channel is shown in Figure 3.2(b), and is dominated by two bands of almost equal intensity, one centred at 3236 cm^{-1} and the other at 3278 cm^{-1}. The band at 3236 cm^{-1} has no

counterpart in the spectrum recorded in the $(CH_3OH)_3Na^+$ mass channel and is therefore assigned to $NaCl(CH_3OH)_2$. This is supported by the corresponding PUCP curve in Figure 3.7, which matches the Poisson curve for n = 2 quite closely. The DFT calculations predict a separation between the antisymmetric (lower wavenumber) and symmetric OH stretches of about 26 cm^{-1} for the global minimum isomer of $NaCl(CH_3OH)_2$. The band at 3278 cm^{-1} might be that band, although it would imply a much larger splitting of 42 cm^{-1} when compared with the 26 cm^{-1} predicted by the DFT calculations. Another band is also seen at a similar position in the $(CH_3OH)_3Na^+$ mass channel and therefore the 3278 cm^{-1} band in Figure 3.2(b) may have contributions from both $NaCl(CH_3OH)_2$ and $NaCl(CH_3OH)_3$. This seems to be supported by the PUCP data, which are somewhat scattered but fall between the Poisson curves for n = 2 and 3. The OH stretching bands of $NaCl(CH_3OH)_2$ should be shifted to the blue of that for $NaCl(CH_3OH)$ for the reason mentioned above. If we accept the assignment made, then the midpoint of the symmetric and antisymmetric bands is indeed shifted to the blue of the single OH stretching band of $NaCl(CH_3OH)$, but the shift is only +3 cm^{-1} whereas the DFT calculations predict a value of 41 cm^{-1}. Other isomers of $NaCl(CH_3OH)_2$ do not offer a better match with experiment, so the assignment to the global minimum energy structure made here seems the most plausible.

3.4.3.3 *Assignment of $NaCl(CH_3OH)_3$*

For the IR spectrum recorded by monitoring the $(CH_3OH)_3Na^+$ channel, the strongest band is seen at 3278 cm^{-1} and was mentioned in the previous paragraph because its overlaps with a band at a similar position in the $(CH_3OH)_2Na^+$ mass channel, see Figures 3.2(c). This band is assigned to $NaCl(CH_3OH)_3$ because there is no obviously sharp structure at this position above the broad absorption envelope in the spectrum in Figure 3.2(d) from the $(CH_3OH)_4Na^+$ mass channel. Of course it is possible that a particular isomer of $NaCl(CH_3OH)_4$ could form $(CH_3OH)_3Na^+$ on ionization but this isomer-selective ion fragmentation seems unlikely. This is confirmed by the PUCP data, which most closely matched the n = 3 Poisson curve. The DFT calculations predict that the lowest energy isomer of $NaCl(CH_3OH)_3$ contains three equivalent IHBs and will have two distinct OH stretching bands because of the threefold rotational

symmetry in this structure. This DFT predictions show two bands at 3284 cm^{-1} and 3320 cm^{-1} with a splitting of 36 cm^{-1}. The band at 3284 cm^{-1} is from the (degenerate) antisymmetric OH stretch and is in good agreement with the experimental band at 3278 cm^{-1}. The other theoretical band at 3320 cm^{-1} arises from the symmetric OH stretch and also shows a good agreement with the experimental spectrum for n = 3, which has a band at 3323 cm^{-1} (marked with a black asterisk). In addition there is another weaker absorption band seen in the IR spectrum at 3349 cm^{-1}, which is labelled with a blue asterisk in Figure 3.2(c). This band is also seen in the $(CH_3OH)_2Na^+$ mass channel and is unfortunately too weak to record useful PUCP data. Consequently, no specific assignment for the weak band at 3349 cm^{-1} has been made but it could be arise from a higher energy isomer of $NaCl(CH_3OH)_3$, or possibly even from $NaCl(CH_3OH)_4$.

3.4.3.4 *Assignment of $NaCl(CH_3OH)_n$ n= 4 and 5*

There is a significant change in the IR spectra recorded by detecting $(CH_3OH)_4Na^+$ (see Figure 3.2(d)). This spectrum shows only very broad absorption features in the OH stretching region, which extend from roughly 3100 to 3400 cm^{-1}. The broad absorption envelope can be explained by the presence of overlapping bands from multiple isomers for $NaCl(CH_3OH)_4$, in addition to possible contributions from larger complexes. The DFT calculations have found seven local minima structures within 0.03 eV of the global potential energy minimum of $NaCl(CH_3OH)_4$ (see Figure 3.6). Figure 3.2(d) shows the predicted IR contributions from each of these isomers beneath the IR spectrum. The simulation shows that contributions from multiple isomers extend across the absorption range of 3200-3450 cm^{-1} and therefore gives a reasonable explanation for the spectral broadening.

The same trend of a broad absorption envelope in the OH stretching region is also seen in the depletion spectrum recorded by detecting $(CH_3OH)_5Na^+$, as shown in Figure 3.8. A broad band was observed from roughly 3050 to 3550 cm^{-1}, which can also be explained by the presence of overlapping bands from multiple isomers for $NaCl(CH_3OH)_5$, as well as contributions from larger complexes.

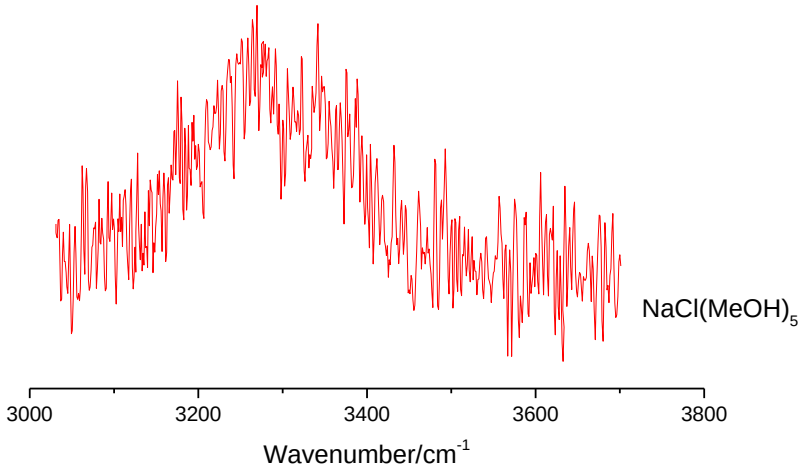

Figure 3.8. Infrared spectrum of $NaCl(CH_3OH)_5$ recorded by monitoring the ion signal at *m*/*z* 183 ($(CH_3OH)_5Na^+$).

3.4.4 Assignment of IR spectra: CH stretching region

Three clear bands can be seen in the IR spectra of $NaCl(CH_3OH)_n$ complexes in the CH stretching region. The CH stretching bands in Figure 3.2 are quite intense, especially for the spectra derived by detecting lighter $(CH_3OH)_nNa^+$ ions. On the other hand, there is even a recognizable trace of CH structure seen in the spectrum recorded at *m*/*z* 151, which can only come from complexes with $n \geq 4$. The three CH absorption bands are found at roughly 2830, 2950 and 2975 cm^{-1}. These bands are shifted a few cm^{-1} to the red when compared with the analogous bands in the isolated methanol molecule in liquid helium.[94] Using the standard notation for free methanol, these three bands can be assigned to the ν_3, ν_9 and ν_2 vibrations of the methanol units in $NaCl(CH_3OH)_n$, respectively. The symmetric CH stretch of the CH_3 group is related to the ν_3 mode, while ν_9 and ν_2 are both derived from antisymmetric CH stretches. There are many anharmonic vibrations with overtone and combination states, such as $2\nu_{10}$ and $\nu_4 + \nu_{10}$, observed in this region. [97] A broad feature to the red of the ν_9 band at 2950 cm^{-1} was observed which reflects these additional vibrational complexity. This can be seen clearly in Figure 3.2(b) and (c).

It is clear that there is no significant change in the CH stretching structure in figure 3.2 as the mass channel is changed. This suggests that the methyl group has no effect on the binding of NaCl to methanol. This in turn is completely consistent

with the DFT calculations for the global minima, where binding of CH_3OH is controlled by IHBs without any participation from the methyl group.

3.5 Conclusions

Infrared spectra of $NaCl(CH_3OH)_n$ complexes have been recorded for the first time. Several separate vibrational bands are observed in the OH and CH stretching regions for n = 1-5. The positions of the OH stretching bands are compatible with formation of isomers in which a IHBs form between the chloride ion and the OH group in each methanol molecule. Narrow bands are seen for $n \leq 3$, while for $n \geq 4$ the narrow bands are replaced by a broad absorption band in the OH stretching region. This significant change for $n \geq 4$ spectra suggests that multiple isomers are formed in the liquid helium environment for these larger complexes. *Ab initio* calculations are used to support the spectral assignments in this work and show reasonable agreement with the experimental data.

CHAPTER 4

Infrared Spectroscopy of LiI$(H_2O)_n$ Complexes in Helium Nanoroplets

4.1 Introduction

The effect of ion size on solvent-solute interactions was studied in the work reported in this chapter. LiI was chosen for this study as an example of a salt with a small positively charged ion coupled with I^- as a large counter-ion. The ability of a single alkali halide molecule to dissolve in a small cluster of water molecules is expected to be strongly dependent on the size, and therefore the charge density, of the cation and anion.[15]

A common way to express how the ions interact with water as a solvent is to describe their behaviour either as *kosmotropic* or *chaotropic* in bulk solution. Kosmotropic ions, also called (order-makers), are usually small and therefore have a relatively high charge density. Presumably, the ordering process of kosmotropic ions in bulk water is related to the formation of the solvation shell and their ability to keep this solvation shell stable in bulk solution. On the other hand, chaotropic ions (disorder-makers) have the opposite effect because they are large in size with low charge density that disrupts the formation of stable solvation shells.[98,99] Li^+, with its small size and high charge density, is expected to be a kosmotropic ion, while I^- acts as a chaotropic ion in bulk solution.[98] So LiI provides an opportunity to combine a kosmotrope with a chaotrope and see the effect this has on complexes formed with network.

The effect of ion size and the hydration number on the formation of a contact ion-pair (CIP) for LiI has been studied using classical molecular dynamics calculations by Liu *et al*.[100] This study was discussed in some detail in section 1.2 of this thesis. Briefly, the potential energy minimum structures of CIP and SSIP for LiI$(H_2O)_n$ complexes depend on the relative cation and anion sizes and the quantity of water added. Liu *et al.* found that the CIP structure of LiI$(H_2O)_n$ for

$n \leq 4$ is lower in energy than the SSIP complexes. However, the energy of the SSIP becomes comparable to that of the CIP at $n = 5$ and therefore an SSIP complex can be formed for $n \geq 5$.[100] By way of contrast, LiF requires many more water molecules to form SSIP complexes. The difference between LiF and LiI can be largely attributed to energetics, and in particular the higher dissociation energy of LiF (577 kJ/mol) [101,102] compared with LiI (about 352 kJ/mol).[101,102] The dissociation of the salt molecule is a fundamental part of the energetic steps needed to form solvated ions and, although F^- has a higher charge density than I^-, and is therefore likely to be solvated more effectively, the higher dissociation energy of LiF seems to be a much bigger obstacle. This argument is consistent with many other previous studies [103-105] suggesting that the ion-pairs consisting of "small−small" ions illustrates stronger associative behaviour between each other, compared with ion-pairs having different ionic sizes (small-large). Thus SSIPs more easily form with fewer water molecules for ion-pairs with dissimilar sized ions, such as LiI.

It is worth discussing the cations (alkali metals) behaviour in water, individually and in absence of the anion effect, to explore the hydration of cations of different sizes. The structures of the alkali metals have been studied by recording the IR and X-ray spectra in aqueous solution.[106] The measurements illustrate that lithium is more strongly hydrated on account of its high charge density and can therefore form a second hydration shell. In contrast, the other alkali ions form only a single shell of water molecules as a result of their lower charge densities.

This chapter will discuss the IR spectra of $LiI(H_2O)_n$ complexes in helium nanodroplets focusing on the OH stretch region. Contact ion-pair structures are observed in a very similar manner to $NaCl(H_2O)_n$. The evidence points towards LiI binding to water molecules via IHBs between the OH groups and the iodide ion for n = 1-3. Broad absorption bands are seen for the larger complexes (n=4-7), which seem to arise also from contributions from multiple isomers. However, there is no direct evidence for SSIP complexes. The experimental work was supported using quantum chemical calculations to explore the structure of the complexes for $n \leq 4$.

4.2 Experimental

Helium nanodroplets were formed using pre-cooled ultrahigh purity helium gas with a stagnation pressure of 33 bar and a nozzle temperature of 16 K. The mean size of the nanodroplets was close to 5500 helium atoms. After passing through the skimmer, the droplets beam then sequentially travelled through two pick-up cells, the first containing LiI vapour and the second water vapour. LiI vapour was produced by resistively heating a pick-up cell containing solid LiI (99.9 %, Sigma-Aldrich) to a temperature of 285 °C. The de-ionised water sample was first degassed using the freeze-pump-thaw technique that mention with details in the previous chapter and then admitted to the second pick-up cell by a needle valve. The partial pressure in the pickup cell was around 10^{-6} mbar. IR spectra in the OH stretching region were then recorded via a depletion technique, as described in Chapter Two.

4.3 Computational details

Ab initio calculations on $LiI(H_2O)_n$ for n = 1- 4 were performed using the Gaussian 09 software package [107] at the National Service for Computational Chemistry Software (NSCCS) at Imperial College in London. Second order Møller-Plesset perturbation theory (MP2) calculations[108] were carried out to find the possible geometries, total energies and vibrational frequencies. Aug-cc-pvtz basis sets were employed for H, O and Li atoms. The effective core potential (ECP) basis set aug-cc-pvtz-pp [109] was used for the I atom, as taken from the EMSL basis set exchange library.[110] A variety of initial structures were chosen with different positions and orientations of the water molecules and LiI in an attempt to find as many isomers of $LiI(H_2O)_n$ as possible. The structures were optimized first at the Hartree-Fock (HF) level of theory to reduce the calculation time. Any equilibrium structures found at the HF level were then re-optimized using MP2 level of theory. The calculated harmonic vibrational frequencies resulting from the optimized structures were scaled by 0.953. This scaling parameter is the recommended value by the National Institute of Standards and Technology (NIST)[111] for this level of theory and is based upon Computational Chemistry Comparison and Benchmark Database Number 101.

4.4 Results and Discussion

4.4.1 *Overview of the experimental results*

Before discussing the mass spectrometric observations, we first review what was previously known about LiI evaporation in the gas phase. The first mass spectrum of LiI vapour was collected by Friedman in 1955.[112] The vapour was produced in this study by heating LiI to 427 °C in an oven in the ion source of the mass spectrometer. Friedman found the first evidence for the presence of both the monomer and the dimer of LiI in the vapour by observing several ions in the mass spectrum, including Li^+, I^+, LiI^+, Li_2I^+, HI^+ and $Li_2I_2^+$. Later, Bencze *et al*. recorded the mass spectrum of LiI vapour in the temperature range of 310-453 °C and found that LiI vapour contains multiple LiI species taking the formula $(LiI)_n$ (n = 1-4). The key finding was that LiI dimer has the highest vapour pressure.[113] Several ions were observed in the mass spectrum of this study such as Li^+, LiI^+ and $[Li(LiI)_n]^+$ (n=1-3). This study shows that the ionisation of the neutral LiI monomer in the vapour can produce both Li^+ and LiI^+ ions. On the other hand, ionisation of $(LiI)_2$ dimer can potentially give several ions such as Li^+, I^+, LiI^+, Li_2I^+, I_2^+ and $Li_2I_2^+$.[113]

In the current study the mass spectrum of LiI vapour was also recorded, in this case by capturing pure LiI vapour in helium nanodroplets. An illustrative mass spectrum is shown in Figure 4.1. Several ions are observed in this spectrum. A series of peaks derived from He_n^+ ions largely dominate the mass spectrum. By way of contrast signals derived from ionization of LiI are relatively weak. The signals for Li^+, Li_2^+, LiI^+ and Li_2I^+ are highlighted with red labels. These ions are presumably derived from the ionisation of the helium nanodroplets containing neutral $(Li)_n$ clusters. It is clear from Figure 4.1 that the signal intensity of LiI^+ ion at 134 m/z is higher than the signal of Li_2I^+ at 141m/z by about 60%. The signal intensity for Li_2^+ at 14 m/z is about the same as that of LiI^+ and is higher than that of the Li^+ signal by about 50%. Ionisation of neutral LiI monomer can only produce Li^+ and LiI^+ ions, while the $(LiI)_2$ dimer has the ability to produce all of the observed ions (Li^+, Li_2^+, LiI^+, Li_2I^+). Consequently, these findings suggest that the $(LiI)_2$ dimer is at least as abundant as the LiI monomer, which does agree to a point with the study by Bencze *et al*.[113]

A mass spectrum obtained after water is added is shown in Figure 4.2. This spectrum was recorded at an LiI oven temperature (285°C), which gave the maximum LiI^+ ion signal. The assumption behind this choice is that this maximum in the ion signal will correlate with the maximum vapour pressure of the LiI monomer. The dominant series marked with the blue lines is assigned to $(H_2O)_nH^+$ formed (presumably) from helium nanodroplets containing no LiI. The other series, marked in red, is attributed $(H_2O)_mLi^+$. The $(H_2O)_mLi^+$ ions are the products of ionization of helium nanodroplets containing $LiI(H_2O)_n$ complexes, where $n \geq m$. Another series of peaks, which are highlighted with red asterisks (in Figure 4.2), are assigned to $(H_2O)_nLi_2^+$ ions. These ions presumably come from the ionization of $(LiI)_2(H_2O)_n$ complexes. Another weak series of peaks was assigned to $(H_2O)_nLi_2I^+$ ions (not shown in Figure 4.2), and these are again attributed to $(LiI)_2(H_2O)_n$ complexes. The relative signal intensities of $(H_2O)_nLi_2^+$ and $(H_2O)_nLi_2I^+$ ions indicate that $(LiI)_2(H_2O)_n$ complexes are more abundant than $LiI(H_2O)_n$ complexes under our experimental conditions, which is consistent with the findings of Bencze *et al*., as discussed earlier. Our evaporation temperature is only marginally lower, by 25 K, than that used by Bencze *et al*., so this assumption is reasonable.[113] Despite the abundance of $(LiI)_2$ dimer complexes with water in helium nanodroplets, this chapter concentrates on complexes of the LiI monomer with water as a first step towards understanding the structure of CIP and SSIP complexes for the LiI/H_2O system. Clearly $(LiI)_2(H_2O)_n$ complexes will make an interesting target for future work. Finally, it seems clear that ionization of LiI follows the same behaviour as NaCl in that it results in loss of a halogen atom.[67,114]

The mass spectra derived from LiI/H_2O mixtures in helium nanodroplets are much weaker, in an absolute sense, than the mass spectra derived from the $NaCl/H_2O$ and $NaCl/CH_3OH$ systems.[67,114] Weak signals were also seen in the mass spectra of $LiI(CH_3OH)_n$ complexes reported in Chapter Five and similarly for LiI with acetone and acetonitrile in Chapter Six of this thesis. This weakness may be related to low vapour pressure of the LiI monomer compared with the $(LiI)_2$ dimer.

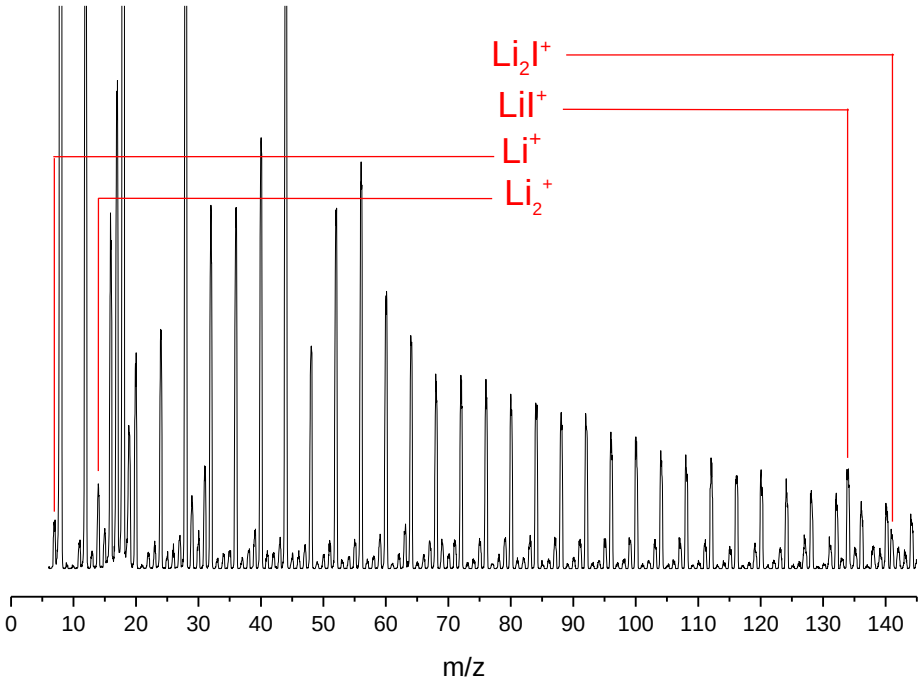

Figure 4.1. Mass spectrum from LiI in helium nanodroplets (temperature for LiI oven was 285 °C) obtained using an electron energy of 70 eV.

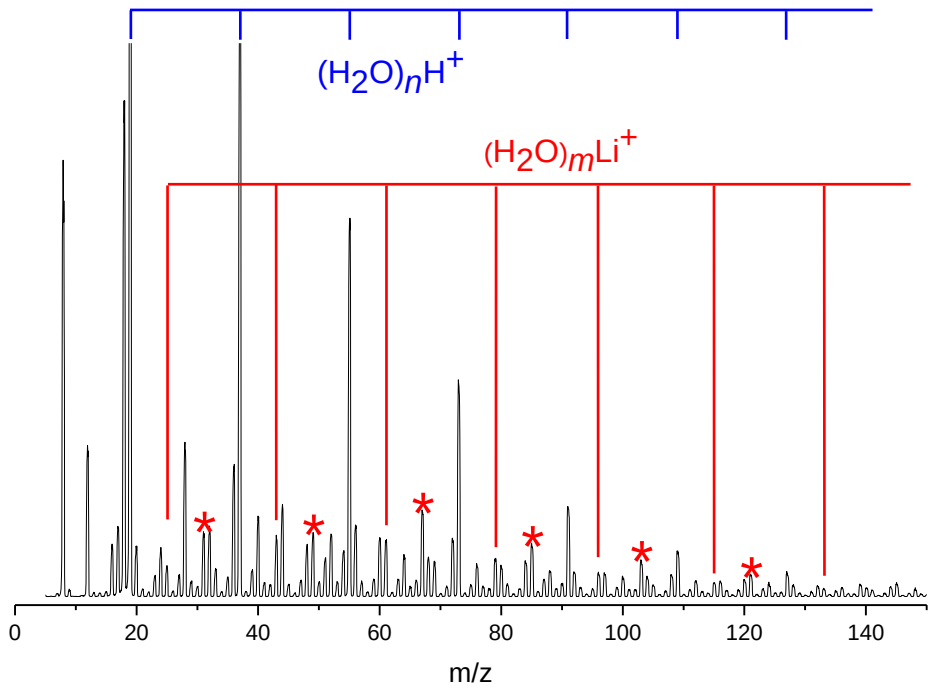

Figure 4.2. Mass spectrum from a LiI/H_2O mixture in helium nanodroplets obtained using an electron energy of 70 eV. The oven temperature was the same as that used to collect the data in Figure 4.1.

Since the peaks assigned to $(H_2O)_mLi^+$ ions are so weak, more evidence, such as Poisson distributions is needed to help with the assignment. The dependence of the ion signals on the water partial pressure has therefore been measured to show that they are consistent with water content. Figure 4.3 shows pick-up pressure data for $(H_2O)_mLi^+$ (m = 1-4) ions at 25, 43, 61 and 79 m/z. In this figure Poisson curves are also shown which show the expected response of the signals as a function of water pickup pressure for different values of m and assuming that the $(H_2O)_mLi^+$ derive from $LiI(H_2O)_m$, *i.e* no significant loss of water molecules on ionization. The data have been collected from several mass spectra recorded under the same experimental conditions (LiI oven temperature and nozzle expansion conditions) but with different water partial pressures. The experimental curves closely match with the Poisson distributions, except the amplitude of the experimental curve for m/z 43 (red symbols) is significantly larger than that predicted by the Poisson curve for m = 2 (red line). The maximum here has an unexpectedly high amplitude which may be caused by overlapping signal from another ion or ions at the same m/z. For example, the propyl cation, $C_3H_7^+$, occurs at m/z 43 and could be derived from trace hydrocarbon contamination from the vacuum system. This difference will be discussed in detail later in the assignment of IR spectrum of $LiI(H_2O)_2$ complex.

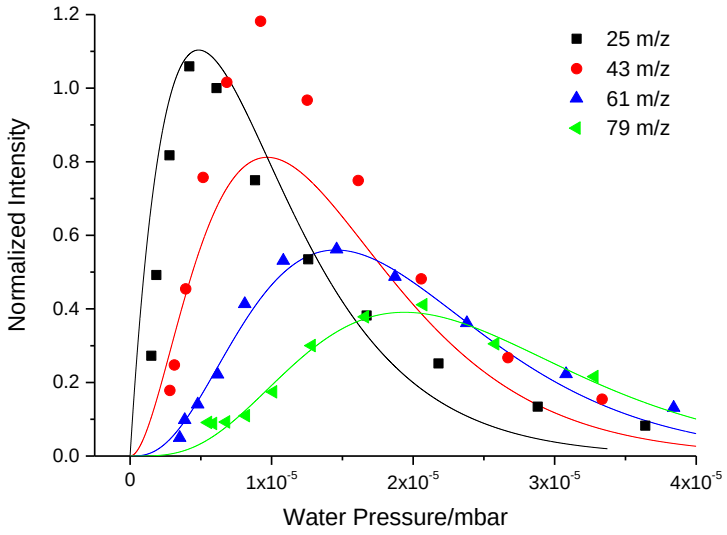

Figure 4.3. Water pressure-dependence of the ion signals at m/z 25 ($(H_2O)Li^+$), m/z 43 ($(H_2O)_2Li^+$), 61 ($(H_2O)_3Li^+$) and 79 ($(H_2O)_4Li^+$). These data were collected with the LiI oven at 285ºC. Also shown are the calculated Poisson curves for the pick-up of one (black), two (red), three (blue) and four (green) water molecules.

Figures 4.4 and 4.5 show the IR spectra recorded by monitoring the $(H_2O)_mLi^+$ ion signals for m = 1-7 in the OH stretching region. Figure 4.4(a), (b), (c) and (d) shows the IR spectra recorded for m = 1-4 together with the predicted IR spectra for of $LiI(H_2O)_n$ from MP2 calculations assuming $n = m$. The predicted spectrum is shown beneath each experimental IR spectrum. Figure 4.5 (a), (b) and (c) shows the IR spectra for m = 5-7.

In general, the IR spectra show some relatively narrow bands, but also in some cases rather broader absorption features can be seen. The S/N ratio in these spectra is not particularly good, although somewhat surprisingly it does seem to increase with the number of attached water molecules. The low S/N ratio may be related to the low intensity of $(H_2O)_nLi^+$ ions observed in the mass spectrum. Also, a significant negative-going feature is observed in the IR spectra which is an artefact derived from the position of the background subtraction gate (see Chapter Two). It was subsequently discovered that by postponing the background gate so that it is after the laser depletion pulse and not before, as measured in this work, the negative-going signal can be removed. However, its presence here does not change the general conclusions from the spectra in Figures 4.4 and 4.5.

In Figure 4.4(a) a single band with a relatively narrow linewidth is seen for m =1. This band lies within the bonded OH stretching region. There is no evidence of a band in the free OH stretching region but given that the signal is weak it is possible that such an absorption does occur but is lost in the noise. The spectrum for m = 2 has three sharp peaks, each with a broader shoulder on one side of the peak. The highest frequency sharp peak is clearly in the free OH stretching region, while the other two fall into the bonded OH stretching region. For m = 3 the spectrum becomes simpler. Once again there is a clear peak in the free OH stretching region and then what appears to be two partly resolved peaks in the bonded OH stretching region. The m = 4 spectrum shows a single but relatively broad and asymmetric band in the free OH stretching. There is also a single, prominent band in the bonded OH stretching region. This band is asymmetric and is accompanied by evidence of broad but weak features in this region.

The IR spectra for *m* = 5-7 are less well defined. Three broad bands are observed clearly for these complexes between 3100 to 3550 cm^{-1}, which puts them in the bonded OH stretching region. A somewhat narrower, although still fairly broad, band is seen in the free stretching region in each case.

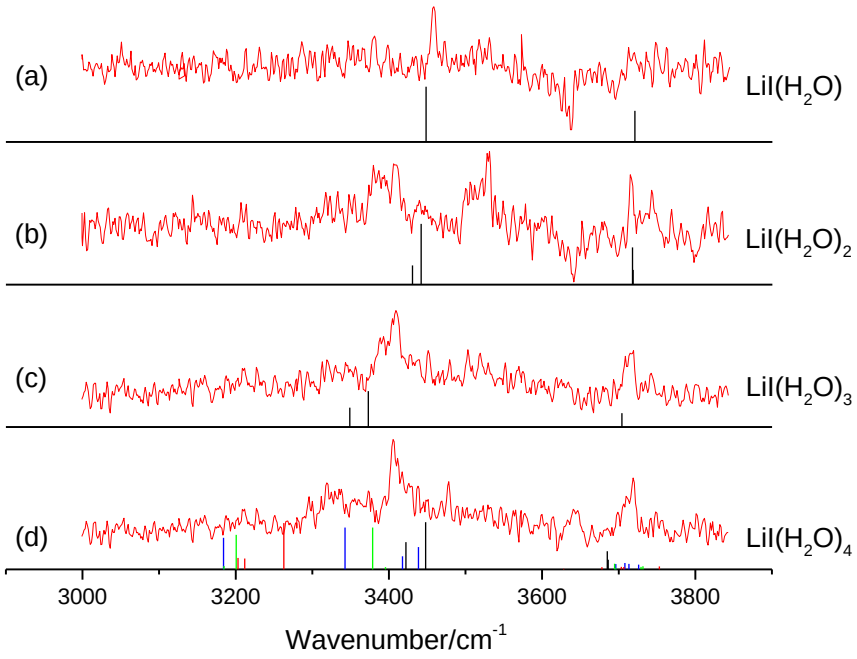

Figure 4.4. Infrared spectra of $LiI(H_2O)_m$ recorded by monitoring ion signals at (a) *m/z* 25 ($(H_2O)Li^+$), (b) *m/z* 43 ($(H_2O)_2Li^+$), (c) *m/z* 61 ($(H_2O)_3Li^+$) and (d) *m/z* 79 ($(H_2O)_4Li^+$)

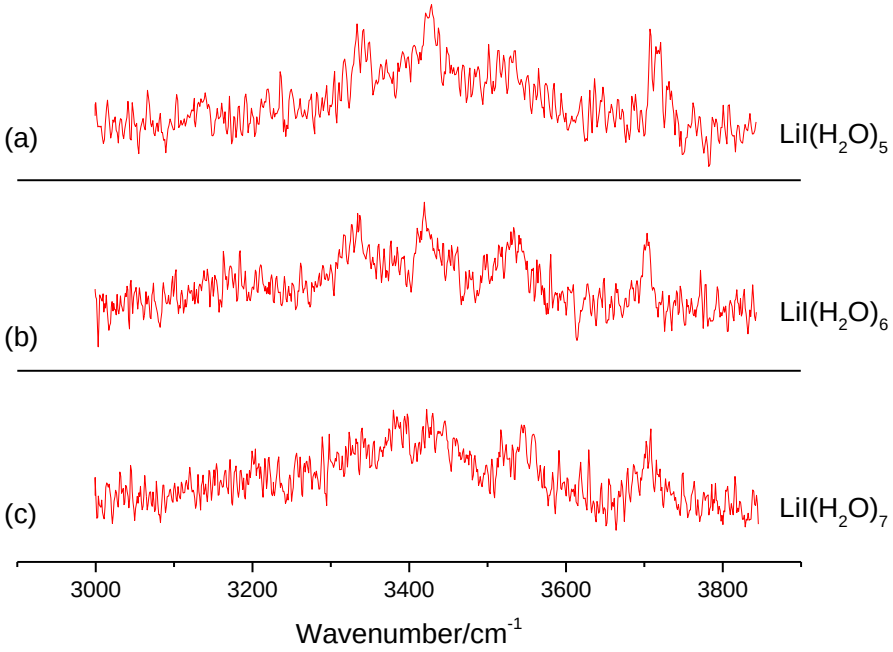

Figure 4.5. Infrared spectra of $LiI(H_2O)_m$ recorded by monitoring ion signals at (a) *m/z* 97 ($(H_2O)_5Li^+$), (b) *m/z* 115 ($(H_2O)_6Li^+$) and (c) *m/z* 133 ($(H_2O)_7Li^+$).

The first challenge is to assign specific bands to specific neutral $LiI(H_2O)_n$ complexes. The dependence of the IR signals on the water pick-up pressure could in principle be used to do this, as was the case for $NaCl(H_2O)_n$ [67] and $NaCl(CH_3OH)_n$.[114] Unfortunately, such measurements were attempted for the (LiI/H_2O) system but, because, the signals are weak, the data were too noisy and therefore do not provide useful information. These pressure measurements are also not helped by broad underlying signals in the OH stretching region, which presumably derive from relatively large complexes. Consequently, attempts to assign the spectra must be done using other information as will be clarified later.

4.4.2 Predicted structures

Two structures corresponding to distinct minima were found for $LiI(H_2O)$ in the MP2 calculations. These structures are qualitatively similar to those found previously for $NaCl(H_2O)$.[67] In the global minimum, the LiI ion-pair is oriented so that the iodide ion can form an ionic hydrogen bond (IHB) with the OH, while additional stabilization is gained by the proximity of the Li^+ ion to the O atom. The other minimum, which is 0.05 eV higher in energy than the global minimum, has an electrostatic interaction between the Li and O atoms but no hydrogen bonding, as can be seen in Figure 4.6.

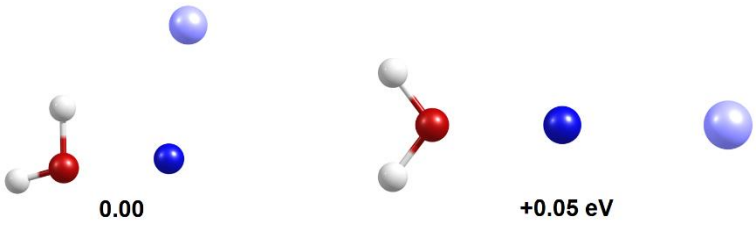

Figure 4.6. Calculated minimum energy structures for $LiI(H_2O)$ along with their energies (not corrected for zero point energy) in eV relative to the global potential energy minimum.

For $LiI(H_2O)_2$, two distinct minima were found (see Figure 4.7). The lowest energy structure has two IHBs linking the iodide to the H atom. The next lowest energy minimum lies 0.092 eV above the global minimum and has two distinct bonding modes, with one water molecule being attached to the LiI via an IHB. The second water molecule in this structure is bonded to the other water molecule via a

normal hydrogen bond but the orientation is such that the Li and O atoms are adjacent and provide additional electrostatic stabilization.

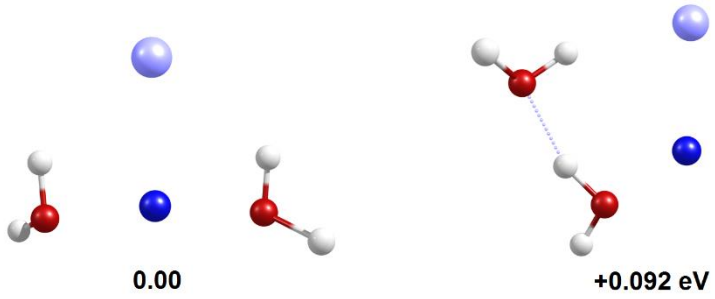

Figure 4.7. Calculated minimum energy structures for $LiI(H_2O)_2$ along with their energies (not corrected for zero point energy) in eV relative to the global potential energy minimum.

Several initial configurations with different positions and orientations of LiI and water molecules were tried in order to find possible equilibrium structures of $Li(H_2O)_n$ for (n = 3 and 4) using the MP2 calculations. From these initial structures only five distinct isomers were found for $LiI(H_2O)_3$ and only four for $LiI(H_2O)_4$. Figure 4.8 shows the five different structures found for $LiI(H_2O)_3$. The global minimum structure for $LiI(H_2O)_3$ has three equivalent IHBs between the iodide and water molecules. The next lowest energy isomer also has three IHBs but the orientations of the free OH groups are now slightly different. This small change in orientation means that this structure lies only 0.026 eV above the global minimum and may be sufficiently close to be interconvertible. The other three structures of $LiI(H_2O)_3$ have energies of 0.076, 0.25 and 1.15 eV, relative to the global minimum. In the lowest energy structure for $LiI(H_2O)_4$, there are three water molecules which are hydrogen bonded to the iodide, forming effectively a first solvation shell. The fourth water molecule is then hydrogen bonded to one of the inner shell H_2O molecules, i.e. there is a single water molecule in a second solvation shell (see Figure 4.9). Three other minima have been found for $LiI(H_2O)_4$ and show energies of 0.0176, 0.032 and 0.088 eV above the global minimum.

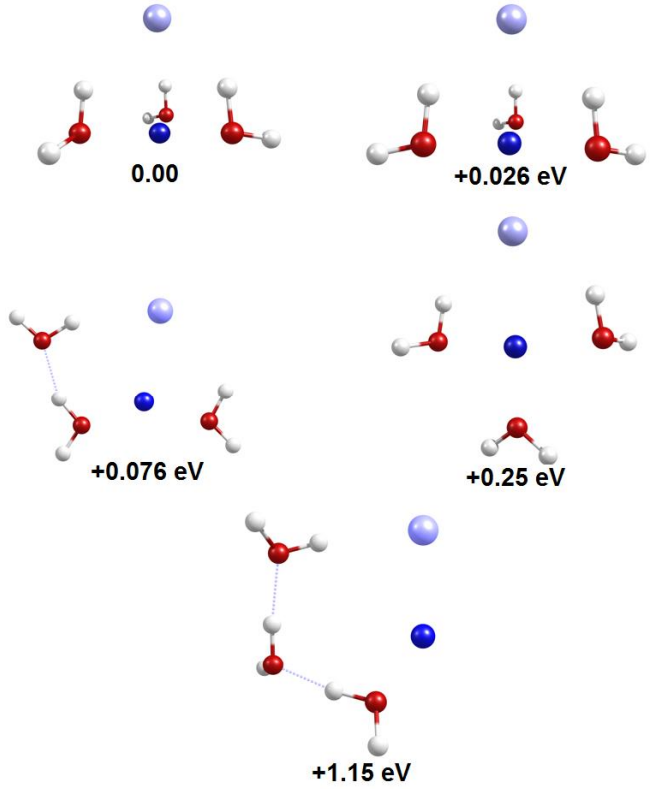

Figure 4.8. Calculated minimum energy structures for $LiI(H_2O)_3$ along with their energies (not corrected for zero point energy) in eV relative to the global potential energy minimum.

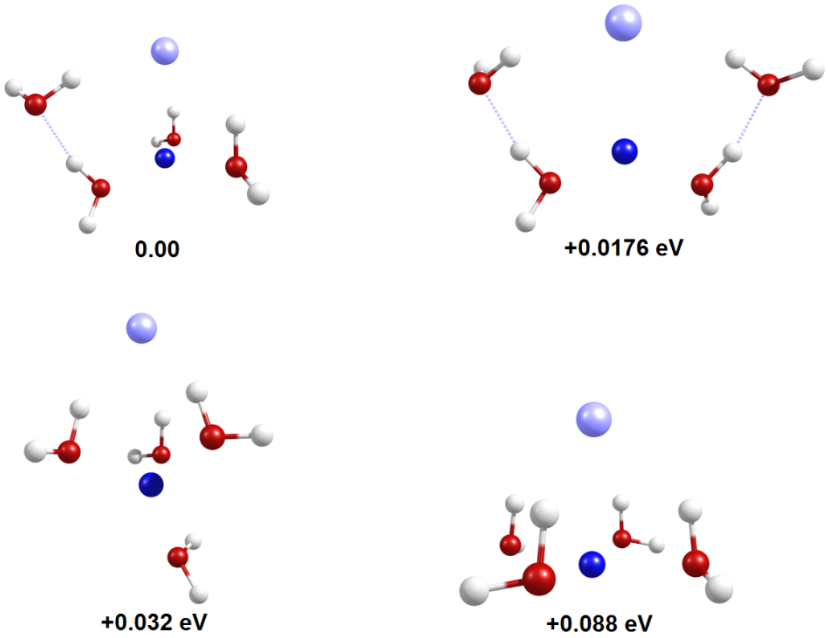

Figure 4.9. Calculated local minima structures for $LiI(H_2O)_4$ along with their energies (not corrected for zero point energy) in eV relative to the global potential energy minimum.

4.4.3. Assignment of IR spectra: OH stretching region

The positions of the IR bands are summarized in Table 4.1. All bands lie between approximately 3350 and 3750 cm^{-1} and are presumed to derive from OH stretches. The bands can be divided into two groups corresponding to those OH groups involved in hydrogen bonds (bonded OH groups) and those that are not involved in hydrogen bonds (free OH groups). As discussed in Chapter Three, the expectation is that any OH involved in hydrogen bonding will have its stretching vibrational frequency red-shifted on account of the weakening of the OH bond by the formation of a hydrogen bond. Examples of this include the hydrated halide complexes, $X^-(H_2O)_n$.[67,114-118] Kim *et al*. found in a theoretical study of $X^-(H_2O)_n$ (X=F, Cl, Br, I) structures that the red-shift of the bonded OH stretching frequency decreases as the size of the halide increases. The red-shift for $X^-(H_2O)_n$ complexes were found to be about 1662, 474, 349 and 220 cm^{-1}, respectively, for F, Cl, Br and I relative to the OH stretching positions of free water molecules.[115] The free OH groups have much higher stretching frequencies and their values are expected to be above 3700 cm^{-1}.

Table 4.1. Positions and assignments of OH stretching bands for $LiI(H_2O)_m$ for m = 1-4.

Band position/cm^{-1}	Assigned carrier
3456 3713	$LiI(H_2O)$
3379 3408 3529 3715 3743	$LiI(H_2O)_2$ $LiI(H_2O)_2 + LiI(H_2O)_3$? $LiI(H_2O)_2$?
3390 3408 3717	$LiI(H_2O)_3$ $LiI(H_2O)_2 + LiI(H_2O)_3$ $LiI(H_2O)_3$
3405 3478 3719	$LiI(H_2O)_4$

4.4.3.1 *Assignment of $LiI(H_2O)$*

We begin the assignment process by discussing the IR spectrum of the simplest complex, $LiI(H_2O)$. The spectrum of this complex might be observable as signal depletion in the Li^+ and/or $(H_2O)Li^+$ mass channels. However, no evidence for any IR absorption was found when detecting Li^+. This is in marked contrast with the

IR spectrum of NaCl(H_2O), which was obtained by monitoring depletion in the Na^+ mass channel.[67] For illustration, Figure 4.10 shows this null IR spectrum of Li^+ signal at *m*/*z* 7. It is therefore concluded that ionization of LiI(H_2O) in a helium droplet leads to ejection only of the I atom, but not the water molecule. Consequently, the IR spectrum obtained by detecting (H_2O)Li^+ (in Figure 4.4(a)) must contain absorption features of LiI(H_2O) (in addition to possible contributions from larger complexes).

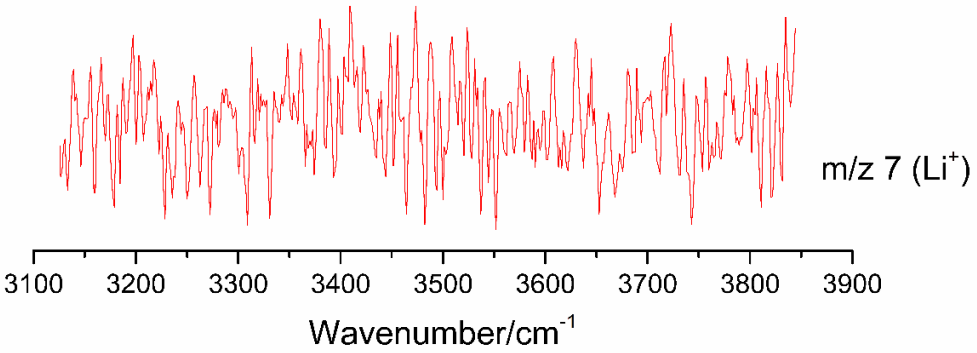

Figure 4.10 Infrared spectrum recorded by monitoring ion signals at *m*/*z* 7, which corresponds to detection of Li^+.

The spectrum in Figure 4.4(a) shows only one, narrow, band at 3456 cm^{-1} in the bonded OH stretching region. No significant bands are seen in the free OH stretching region. It therefore seems reasonable to conclude that this band comes from LiI(H_2O) and that one isomer of this complex dominates in helium nanodroplets. Beneath the experimental spectrum in Figure 4.4(a) is a simulation derived from MP2 calculations for the global minimum isomer for LiI(H_2O). The experimental and MP2 band positions in the OH bonded region are in close agreement, the difference in positions being only 8 cm^{-1}. This excellent agreement between theory and experiment provides good support for the assignment of the spectrum of LiI(H_2O). The other isomer of LiI(H_2O) obtained from MP2 calculations has been excluded from consideration because it has no bonded OH stretches. No free OH stretching absorption is seen in Figure 4.4(a), perhaps because the S/N ratio is unfavourable.

As anticipated by the calculations, the OH stretching frequency is red-shifted by 278 cm^{-1} compared with the OH antisymmetric stretching band of H_2O monomer (3720 cm^{-1}). For I^-(H_2O), *ab initio* calculations [116] predict that the OH stretching

band will be red-shifted by 307 cm^{-1} for a structure containing an ionic hydrogen bond between I^- and H_2O. The smaller red-shift for $LiI(H_2O)$ compared with $I^-(H_2O)$ is reasonable because the latter is exposed to the full negative charge on the iodide ion, whereas a smaller partial charge is expected on the iodide in $LiI(H_2O)$. Consequently, the IHB for $LiI(H_2O)$ will be weaker than for $I^-(H_2O)$ and therefore the corresponding OH bond will be stronger.

4.4.3.2 *Assignment of $LiI(H_2O)_2$*

The IR spectrum of $LiI(H_2O)_2$ is presumably contained within the spectrum recorded in the $(H_2O)_2Li^+$ mass channel (see Figure 4.4(b)). The spectrum shows several bands of almost equal intensity, some narrow and some clearly broader. The spectrum was recorded twice and retains essentially the same features in both spectra, although the relative band intensities did differ. Two peaks were seen in the bonded OH stretching region, one broader than the other and centred at 3379 cm^{-1} and 3408 cm^{-1}. The band at 3379 cm^{-1} has no counterpart in the spectrum recorded in the $(H_2O)_3Li^+$ mass channel and so it was assign to $LiI(H_2O)_2$. The other band at 3408 cm^{-1} in the $(H_2O)_2Li^+$ mass channel coincides with a band seen at a similar position in the $(H_2O)_3Li^+$ mass channel and so this band may have contributions from both $LiI(H_2O)_2$ and $LiI(H_2O)_3$, or indeed may just be entirely from $LiI(H_2O)_3$. The latter seems more likely given that this band is relatively narrow. This assignment is supported by the MP2 calculations, which predict a global minimum for $LiI(H_2O)_2$ which has two bonded OH stretches at 3430 cm^{-1} and 3442 cm^{-1}, which puts them reasonably close to the experimental bands at 3379 and 3408 cm^{-1}. The splitting between the two observed bands in the IR spectrum is ca. 28 cm^{-1}, which is larger than the 12 cm^{-1} predicted from the MP2 calculations. The other predicted isomer of $LiI(H_2O)_2$ has an energy 0.092 eV above the global minimum and shows two OH bonded bands at 3103 and 3335 cm^{-1}. It is clear that the position of these predicted bands are incompatible with the experiment result, and so this isomer does not seem to contribute to the spectrum. Equally, the other higher energy isomers do not yield predicted bands that would match the observed spectrum. The experimental bands at 3379 and 3408 cm^{-1} are therefore assigned to the global minimum energy structure of $LiI(H_2O)_2$.

There is a third band in the *m* = 2 spectrum in Figure 4.4(b), a broad band with a very clear shoulder with the maximum at 3529 cm^{-1}. This absorption has no analogue in the IR spectrum of $LiI(H_2O)$ and the two predicted isomers of $LiI(H_2O)_2$. This band might derive from a possible contaminant signal at 43 m/z. The possibility of a contaminant signal at this mass was discussed earlier in relation to the pickup pressure data in Figure 4.3.

In the free OH stretching region, one narrow band is clearly seen at 3715 cm^{-1} when detecting $(H_2O)_2Li^+$. There is also a somewhat broader and weaker peak at 3743 cm^{-1} but given the background noise, it is not clear whether or not this is a real absorption feature, rather than baseline extension. Given this the higher frequency feature has been ignored from here onwards. The band at 3715 cm^{-1} is assigned to free OH stretches. MP2 calculations for a global minimum structure of $LiI(H_2O)_2$ predict a band in the free OH region at 3717 cm^{-1} that shows good agreement with the experimental band at 3715 cm^{-1}. The other isomer is predicted to have two bands in the free OH stretching region at 3693 and 3735 cm^{-1}. These bands are shifted from the experimental band by about 24 cm^{-1} and 18 cm^{-1}, respectively. Also, as mentioned previously in this paragraph, the fact that this isomer has two bands in the OH bonded stretching is not consistent with the experimental structure. Therefore, this isomer can be ruled out and the band at 3715 cm^{-1} is assigned to the free OH stretching for the global minimum structure $LiI(H_2O)_2$.

4.4.3.3 *Assignment of $LiI(H_2O)_3$*

Two bonded OH stretching bands with different intensities are seen in the $(H_2O)_3Li^+$ mass channel. These two bands peak at 3387 cm^{-1} and 3408 cm^{-1} (see Figure 4.4(c)), with the latter showing the higher intensity. The band at 3408 cm^{-1} was mentioned above, since it coincides with a band in the $(H_2O)_2Li^+$ mass channel. MP2 calculations predicted five different isomers for $LiI(H_2O)_3$. The global minimum structure contains three almost equivalent IHBs between iodide and water molecules with almost identical orientations of the free OH groups. According to the calculations this isomer has three absorptions in the bonded OH stretching region, one with high intensity at 3373 cm^{-1} and the other two bands with low intensity at 3345 cm^{-1} and 3348 cm^{-1}. The predicted band at 3373 cm^{-1}

is essentially the symmetric OH stretching vibration of all three OH groups and is compatible with the experimental band at 3408 cm^{-1}, but is red-shifted by 35 cm^{-1}. Consequently, the experimental band at 3387 cm^{-1} is assigned to the (almost degenerate) antisymmetric OH stretching vibrations. The theoretical splitting between the symmetric and antisymmetric stretches is ~26 cm^{-1}, which fits quite well with the experimental splitting of 21 cm^{-1}.

The isomer of $LiI(H_2O)_3$ lying 0.026 eV above the global minimum also contains three equivalent IHBs between iodide and water molecules but with different orientations of the free OH groups. According to the calculations the IHBs deliver three OH stretching bands at 3335, 3368 and 3390 cm^{-1}. These bands are clearly close to the two experimental bands but the structure is not consistent with experiment and so this isomer was ruled out as a contributor to the IR spectrum. The even higher energy isomers show three OH stretching bands extending from 3027-3363 cm^{-1}, which bears no relationship to the experimental findings. These isomers are therefore also ruled out as potential contributors to the IR spectrum.

Turning now to the free OH stretching in the IR spectrum obtained by detecting $(H_2O)_3Li^+$, a single but quite broad band was observed centred at 3713 cm^{-1}. The MP2 prediction for the global minimum structure of $LiI(H_2O)_3$ predicts a single band at 3704, which is only 9 cm^{-1} from the experimental position.

4.4.3.4 *Assignment of $LiI(H_2O)_4$*

Figure 4.4(d) illustrates the IR spectrum obtained by detecting $(H_2O)_4Li^+$. This spectrum can only come from $LiI(H_2O)_4$ and larger complexes. A relatively intense band peaking at 3404 cm^{-1} is seen in addition to broad underlying absorption in the bonded OH stretching region extending from about 3300-3390 cm^{-1}. Also, seen is a single, relatively broad, band in the free OH stretching region. The presence of broad bands in both free and bonded OH stretching regions presumably derive from contributions from multiple isomers for $LiI(H_2O)_4$ and larger complexes. The MP2 calculations support this suggestion by predicting four isomers within 0.088 eV of the global potential energy minimum of $LiI(H_2O)_4$,, as can be seen in Figure 4.9. The predicted IR bands of these isomers are shown in Figure 4.4(d) beneath the spectrum in different colours and lie in the same

general regions as the experimental bands. However, specific assignments to specific isomers of $LiI(H_2O)_4$ are not possible.

4.4.3.5 *Assignment of $LiI(H_2O)_n$ n= 5-7*

IR spectra obtained by detecting $(H_2O)_5Li^+$, $(H_2O)_6Li^+$ and $(H_2O)_7Li^+$ signals are shown in Figure 4.5. A series of relatively broad bands are seen in the bonded OH stretching region along with a single broad band in the free OH stretching region. The bonded OH stretching bands are seen in range between 3300 cm^{-1} and 3600 cm^{-1} while the free OH bands span 3700-3720 cm^{-1}. A small red-shift in the free OH stretching bands was seen which increase gradually from $(H_2O)_5Li^+$ to reach about 12 cm^{-1} in $(H_2O)_7Li^+$complex. The broadness of the bands in both OH stretching regions gives support to the idea that multiple isomers contribute to these absorption features.

4.5 Conclusions

CIP complexes of $LiI(H_2O)_n$ have been formed in helium nanodroplets for the first time. IR spectra have been recorded and compared with predictions from *ab initio* calculations. Several vibrational bands are seen in the OH stretching regions for n = 1-7. The positions of the OH stretching bands for n = 1 and 2 are consistent with formation of a dominant isomer in which the iodide ion forms an ionic hydrogen bond to an OH group in each water molecule. The spectra for $n \geq 3$ suggest that multiple isomers are formed in the liquid helium environment.

Given the evidence for the abundance of $(LiI)_2$ dimers in the vapour above solid LiI, this work could be expanded in the future by recording the IR spectra of $(LiI)_2(H_2O)_n$ complexes. This would be achieved by monitoring IR-induced depletion of $(H_2O)_nLi_2^+$ and $(H_2O)_nLi_2I^+$ signals. By looking at the hydration of clusters of a salt, such as LiI, one is in a sense getting closer to what a real salt would consist of, namely multiple positively charged and negatively charged ions. For example, how much more difficult is it to form SSIP complexes for $(LiI)_2$? The effect this would have on the hydration behaviour would be extremely interesting to investigate.

CHAPTER 5

Infrared Spectroscopy of LiI$(CH_3OH)_n$ Complexes in Helium Nanoroplets

5.1 Introduction

The interaction of LiI with methanol, an alternative protic solvent to water, is presented in this chapter. The study focused on the formation of contact ion-pair (CIP) complexes of the type LiI$(CH_3OH)_n$ in helium droplets. The structures of these CIP complexes was explored spectroscopically by recording their infrared spectra. These spectra were recorded in the OH and CH stretching region.

A mass spectrometric investigation of LiI/methanol clusters was reported some years ago by Martin and Bergmann.[119] In this study, the clusters were produced by allowing both LiI vapour (from an oven) and methanol vapour to mix inside a condensation cell cooled with liquid nitrogen. The condensation cell was filled with 1 mbar helium gas to improve the thermal conductivity. The clusters then entered the analysis chamber through a small aperture and were subjected to quadrupole mass spectrometry using electron ionization. In the absence of methanol several types of ions were observed such as Li^+, $[Li(LiI)]^+$, $[Li(LiI)_2]^+$ and $[Li(LiI)_3]^+$. The assumption was made that the main source of each of these ions was LiI, $(LiI)_2$, $(LiI)_3$ and $(LiI)_4$, respectively. When methanol was added the main series of ions seen in the mass spectrum arose from $[Li(LiI)_m(CH_3OH)_n]^+$ with m = 1 and n = 1-20. Enhanced intensities were seen for $[Li(LiI)(CH_3OH)_{4,8,12}]^+$ ions. The high intensity of these particular ions compared with the neighbouring ions presumably originates from the high stability of the cyclic tetramer of methanol, which is not affected dramatically by the presence of LiI ion-pair. Therefore, the sequence of 4, 8 and 12 may refer to the presence of structural blocks involving four molecules of methanol.

It is useful to mention some previous theoretical and experimental studies which have focused on the solvation and the structures of LiI-methanol clusters in bulk

solutions.[120-125] A mass spectrometric study has explored the solvation of different lithium halide salts, LiX (X=Br,Cl, I), in methanol solution.[120] Ions were formed by electrospray ionisation. Two main series of peaks with the formulas $(CH_3OH)_n(LiI)_mLi^+$ and $(CH_3OH)_nLi^+$ were observed. The data analysis for the formula $(CH_3OH)_n(LiX)_mLi^+$ show a significant difference in the solvated LiI-methanol clusters compared to LiCl and LiBr/methanol clusters. The value of (*m*) in $(CH_3OH)_m(LiI)Li^+$ was found in (1-6), when the value of (*m*) became (1-7) in case of $(CH_3OH)_m(LiI)_2Li^+$ structure. In contrast, the value of (*m*) and (*n*) in the LiCl and LiBr clusters with methanol are considerably smaller. The author refers that this difference may be related to the weak interaction of Li-I compared to the interaction with Li-Cl and Li-Br. This weak interaction increases the possibility of methanol to separate the Li-I ion-pair more easy than Li-Cl and LiBr ion-pairs in methanol solution.

In a molecular dynamics (MD) simulation, the effect of cation and anion size on the structure of the methanol solvation shell at 298 K has been explored.[121] In particular, the differences in association between lithium halides salts LiX (X = F^-, Cl^-, I^-), was investigated to see the effect of different anion sizes. The MD calculations allowed the radial distribution functions for methanol molecules around the ions to be determined along with their orientations. This study shows that the variation of ion size in an ion-pair influences the solvation structure of the other ion. The methanol coordination number decreases with increasing halide anion size, which is the opposite of the behaviour of these anions in water. This difference apparently comes from the low dielectric strength of methanol compared with water, and therefore weaker shielding of the charge is expected for methanol compared with water. The data also illustrate that small ion-pairs (Li^+- F^-) are more stable than pairs with different sized ions (such as Li^+- I^-) in methanol.

More details about the LiI/ methanol interaction will be provided in this chapter by recording the IR spectra of LiI/methanol complexes in helium nanodroplets. As will be seen, the spectroscopic data for $LiI(CH_3OH)_n$ recorded in the current study are consistent with structures in which up to three methanol molecules can bind to a neutral LiI molecule via ionic hydrogen bonds between the OH groups and

the iodide ion. The experimental work has been supported using quantum chemical calculations to explore the structure of the complexes for n ≤ 4.

5.2 Experimental

In brief, helium nanodroplets were formed by expanding pre-cooled ultrahigh pure helium gas with stagnation pressure of 33 bar and at 16 K through a pinhole nozzle, as described in previous chapters. The mean size of the droplets was close to 5500 helium atoms. After passing through a skimmer, the droplet beam then sequentially travelled through two pick-up cells, the first containing LiI vapour and the second methanol vapour. LiI vapour was produced by resistively heating a pick-up cell containing solid lithium iodide to a temperature of 285°C. Methanol vapour was admitted to the second pick-up cell in a controlled manner using an ice bath and a needle valve. The partial pressure in the solvent pickup cell was around 10^{-6} mbar. Under these conditions, $LiI(CH_3OH)_n$ complexes can be formed and their absolute and relative quantities can be optimized by adjusting the dopant partial pressures.

IR spectra were recorded via a depletion technique by recording the reduction in the mass signal, as a result of IR absorption by the dopant was followed by helium evaporation during scans of the IR wavelength.

5.3 Computational details

Calculations on $LiI(CH_3OH)_n$ for n = 1- 4 were carried out using second order Møller-Plesset perturbation theory (MP2) [108] within the Gaussian 09 software package.[107] The calculations were performed via the National Service for Computational Chemistry Software (NSCCS) at Imperial College in London. Geometry searches, energy evaluations and vibrational frequency calculations were performed using 6-311++G(d,p) basis sets for H, O, C and Li atoms. The effective core potential (ECP) basis set Def2-TZVPD [126] was used for the I atom, as obtained from the EMSL basis set exchange library.[110] Harmonic vibrational frequencies were scaled by 0.895. This value for the scaling factor is clearly considerably lower than the standard values, which are more typically near to 0.95. No scaling factor was found in the literature for MP2 theory with the chosen basis set. Therefore, the chosen value was obtained from a comparison with the

experimental data by fitting the theoretical result of the global minimum structure of the LiI(CH_3OH) complex with the OH bonded stretching band in the IR spectrum of the same complex, (see later for more details). Also, the position of CH stretching bands in the IR spectra of the LiI$(CH_3OH)_n$ complexes were taken in to consideration in choosing the value of the scaling factor. The CH stretching bands of LiI$(CH_3OH)_n$ were compared with CH stretching bands of NaCl$(CH_3OH)_n$ in Chapter Three.[114] The difference in the CH frequencies between theory and experiment was found within 10 cm^{-1} with the chosen value of scaling factor, which gives additional support to this value.

5.4 Results and Discussion

5.4.1 Overview of the experimental results

Starting with the mass spectrum of LiI/methanol complexes, Figure 5.1 shows an illustrative spectrum from helium nanodroplets doped with LiI$(CH_3OH)_n$ complexes. Two series of peaks are highlighted, one assigned to $(CH_3OH)_nH^+$ and the other to $(CH_3OH)_mLi^+$. The $(CH_3OH)_nH^+$ ions are presumed to come from ionization of helium nanodroplets containing only methanol clusters, while the other weak $(CH_3OH)_mLi^+$ ions are the products of ionization of helium nanodroplets containing LiI$(CH_3OH)_n$, where $n \geq m$. As seen in previous chapters, a halogen atom is readily lost on ionization. Another series of peaks, highlighted with blue asterisks, are assigned to $(CH_3OH)_nLi_2^+$ ions and these most likely originate from the ionization of $(LiI)_2(CH_3OH)_n$.

As can be seen in Figure 5.1, the intensity of $(CH_3OH)_nLi_2I^+$ ions is higher than $(CH_3OH)_nLi^+$ ions. The experimental conditions were chosen to give the maximum LiI^+ ion signal in the absence of water vapour, which are the conditions which presumably correlate with the maximum vapour pressure of the LiI monomer. Similar behaviour was seen in Chapter Four for LiI$(H_2O)_n$ complexes and discussed in detail there (see section 4.4.1). This difference in the intensities of $(CH_3OH)_nLi_2I^+$ and $(CH_3OH)_nLi^+$ ions supports the claim in Chapter Four about the greater abundance of the $(LiI)_2$ dimer compared with the monomer in the vapour above solid LiI.

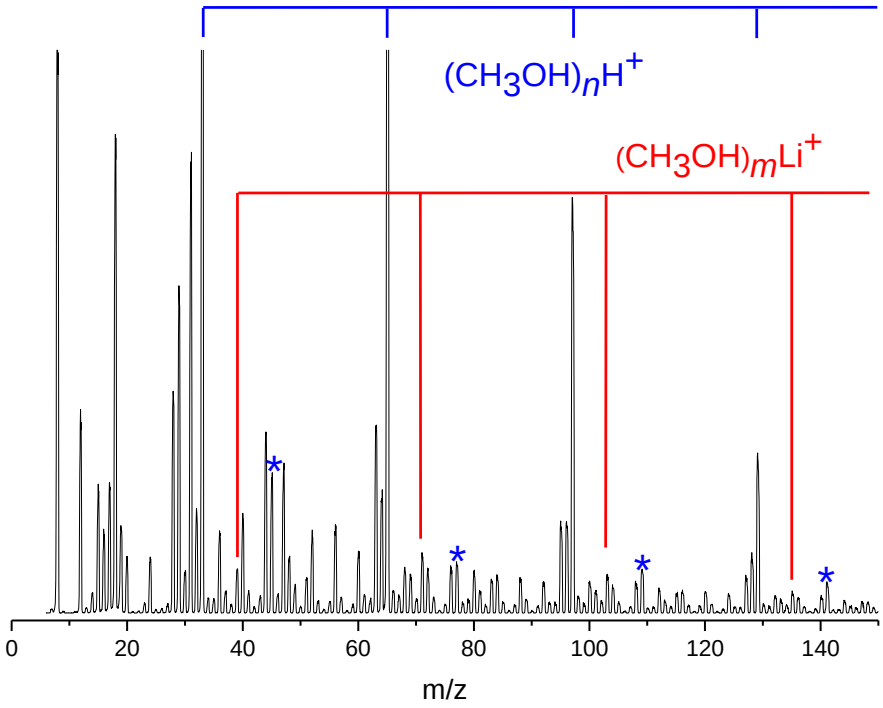

Figure 5.1. Mass spectrum from the LiI/CH_3OH system obtained using an electron energy of 70 eV. Further details are provided in the main text.

The $(CH_3OH)_mLi^+$ ions from $LiI(CH_3OH)_n$ are not particularly abundant. To provide additional confirmation that the peaks we identify are indeed dominated by contributions from $(CH_3OH)_mLi^+$ ions, the dependence of the ion signal on the partial pressure of methanol was recorded, as shown in Figure 5.2. This figure shows pick-up pressure data for $(CH_3OH)_mLi^+$ ions at 39, 71, 103 and 135 m/z respectively in addition to Poisson curves for different values of n = 1-4. The data have been collected from several mass spectra recorded under the same experiment conditions (LiI oven temperature and nozzle expansion conditions) but with different methanol partial pressures. The experimental curves fit quite closely with the Poisson curves and are entirely consistent with the progressive increase in the number of methanol molecules as the mass of the ion monitored is increased. Consequently, while not proving that the signals detected come from $(CH_3OH)_mLi^+$ ions, they are certainly consistent with them and therefore most likely derive from ionization of $LiI(CH_3OH)_n$ complexes.

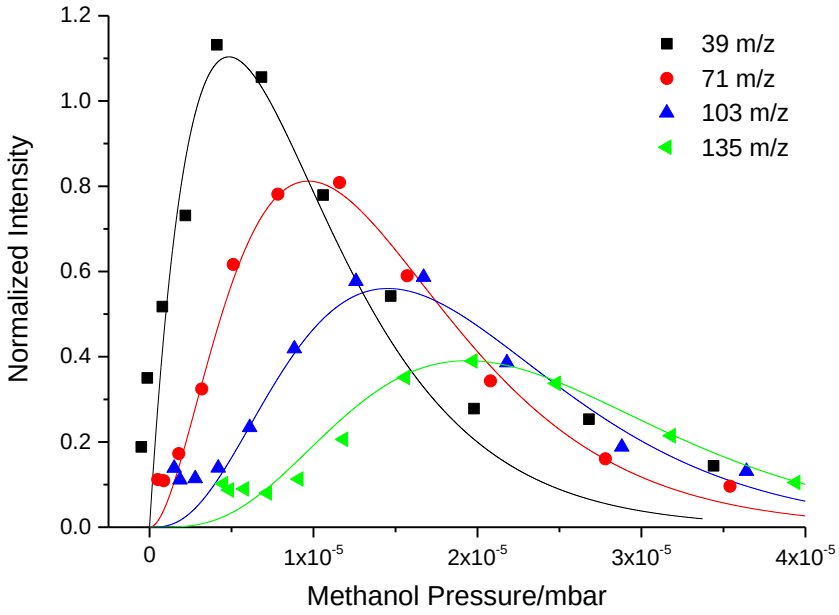

Figure 5.2. Methanol pressure-dependence of the ion signals at *m*/*z* 39 ($(CH_3OH)Li^+$), *m*/*z* 71 ($(CH_3OH)_2Li^+$), 103 ($(CH_3OH)_3Li^+$) and 135 ($(CH_3OH)_4Li^+$). Also shown are the calculated Poisson curves for the pick-up of one (black), two (red), three (blue) and four (green) methanol molecules. These data were collected with the LiI oven at 285ºC.

IR spectra recorded by monitoring the IR-induced depletion of specific $(CH_3OH)_mLi^+$ ions signals for m = 1-6 are shown in Figures 5.3 and 5.4. Bands with relatively narrow linewidths are seen for m = 1-3 in the OH stretching region. Both sharp and broad absorption features can be seen in the m = 4 mass channel. For m = 5 and 6, the narrow bands seen in the smaller complexes are completely replaced by much broader absorption features. No clear bands are seen in the CH stretching region and possible reasons for this absence will be discussed later. The assignments of the spectral carriers shown to the right of each spectrum assume that no ion fragmentation occurs on ionization, other than loss of the iodine atom. This assumption is made for convenience rather than accuracy.

Unfortunately, the dependence of the IR signal on the methanol pick-up pressure could not be used to confirm the spectral assignments for $LiI(CH_3OH)_n$ because the depletion signals were too weak. Consequently, other information must be used to make band assignments.

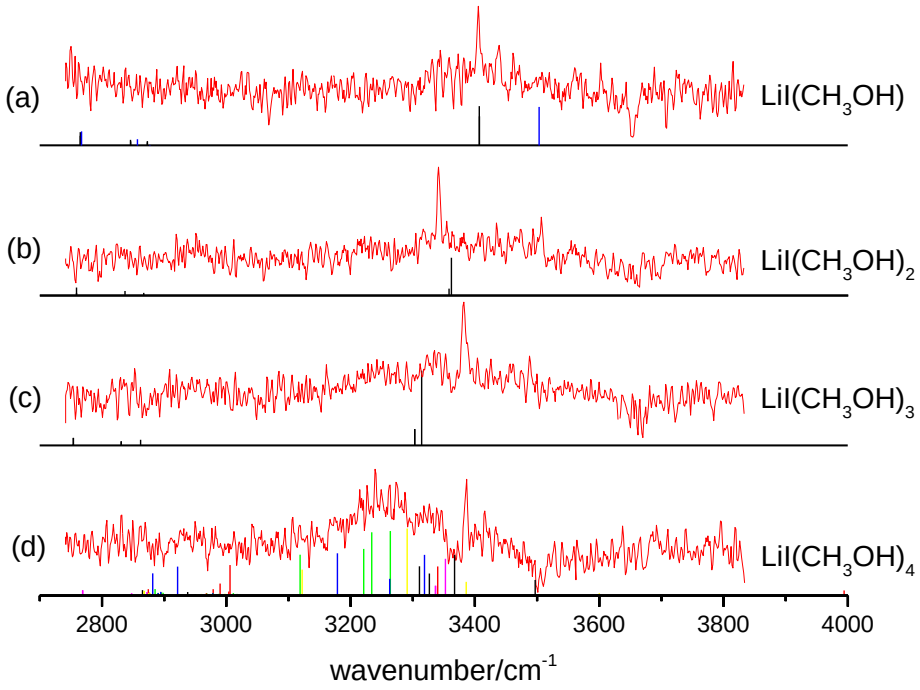

Figure 5.3. Infrared spectra of $LiI(CH_3OH)_n$ recorded by monitoring ion signals at (a) *m*/*z* 39 ($(CH_3OH)Li^+$), (b) *m*/*z* 71 ($(CH_3OH)_2Li^+$), (c) *m*/*z* 103 ($(CH_3OH)_3Li^+$) and (d) *m*/*z* 135 ($(CH_3OH)_4Li^+$). Also shown are the theoretical IR spectra for the complexes shown on the right of the figure. For *n* = 1-3 only the vibrational lines from the global minimum energy structure are shown while the transitions from the global minimum and all calculated local minima are shown for *n* = 4.

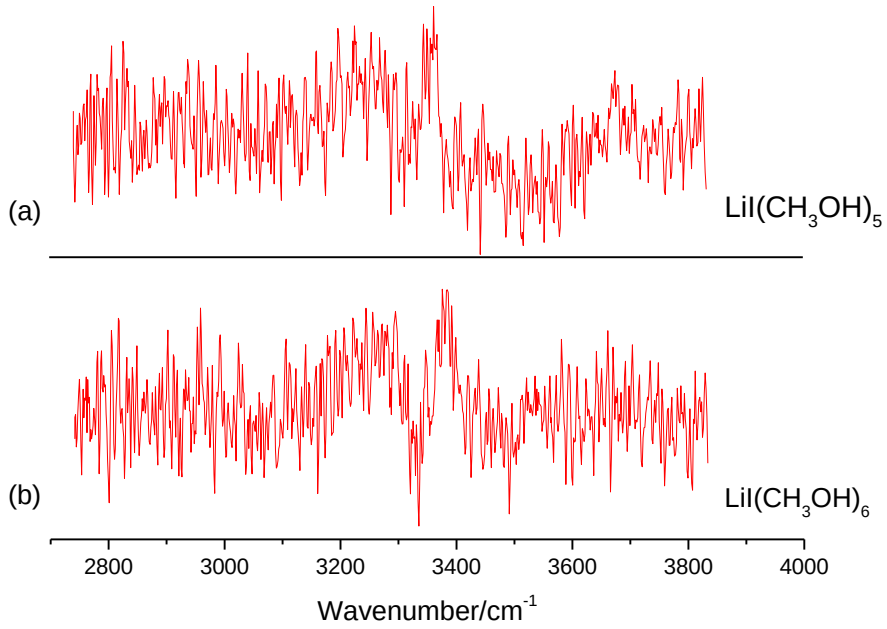

Figure 5.4. Infrared spectra of $LiI(CH_3OH)_n$ recorded by monitoring ion signals at (a) *m*/*z* 167 ($(CH_3OH)_5Li^+$) and (b) *m*/*z* 199 ($(CH_3OH)_6Li^+$).

5.4.2 Predicted structures

Two structures corresponding to distinct minima were found for the LiI(CH_3OH) complex in the MP2 calculations, as illustrated in Figure 5.5. The global minimum structure is obviously different from those found for NaCl$(CH_3OH)_n$ and LiI$(H_2O)_n$ in the previous two chapters, and also for NaCl$(H_2O)_n$ [67]. In the global minimum the LiI ion-pair is oriented so that the iodide ion can form a hydrogen bond (HB) with a CH on the methanol and the Li^+ becomes adjacent to the O atom. This suggests that an electrostatic interaction between Li^+ and the O atom is the dominant interaction term. This is not surprising given the very high charge density expected for Li^+, which can make the electrostatic interaction much stronger than the hydrogen bond between the OH and the halide. The next lowest energy minimum, which is 0.036 eV higher in energy than the global minimum, shows the anticipated ionic hydrogen bond (IHB) between the OH group and the iodide. Clearly both structures are relatively close in energy and so both might be present in experiments.

Figure 5.5. Calculated equilibrium structures for LiI(CH_3OH) along with their energies (not corrected for zero point energy) in eV relative to the global potential energy minimum.

For LiI$(CH_3OH)_2$, the calculations found four distinct minima (see Figure 5.6). The lowest energy structure has two IHBs linking the iodide ion and the OH groups. The next lowest energy minimum lies 0.037 eV above the global minimum and has no IHBs. Instead, and analogous to the global minimum for LiI(CH_3OH), there are hydrogen bonds between CH groups and the iodide in each methanol, molecule and a dominant interaction between the Li^+ and the O atoms. The other two calculated structures have other hydrogen bonding configurations, as shown in the lower half of Figure 5.6.

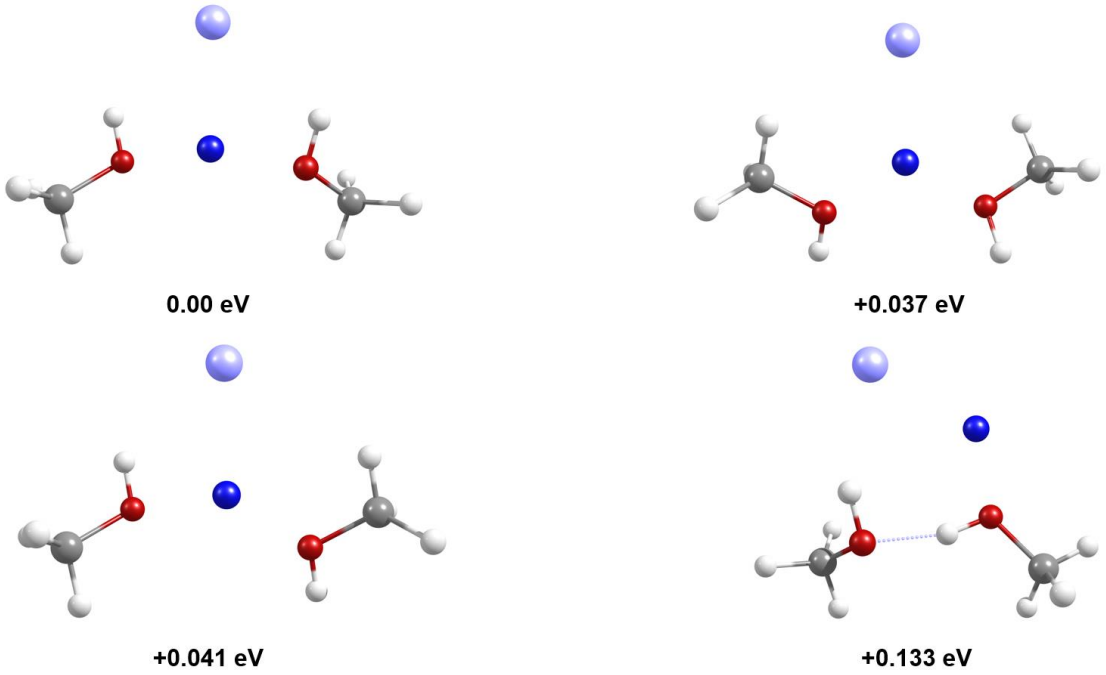

Figure 5.6. Calculated equilibrium structures for $LiI(CH_3OH)_2$ along with their energies (not corrected for zero point energy) in eV relative to the global potential energy minimum.

For *n* = 3 and 4 the structural landscape becomes more complex. Six distinct minima were found for $LiI(CH_3OH)_3$. The global minimum is analogous to that found for $LiI(CH_3OH)_2$, but now with three equivalent IHBs (see Figure 5.7). The next lowest energy minimum lies 0.034 eV above the global minimum and also has a three equivalent IHBs but with non-equivalent orientations of the methyl groups. Seven isomers were found in MP2 calculations for $LiI(CH_3OH)_4$. In the lowest energy structure, three methanol molecules are bonded to the iodine atom via IHBs. The remaining methanol molecule is effectively located in a second solvation shell and is hydrogen-bonded to one of the methanol molecules in the inner solvation shell, as shown in Figure 5.8.

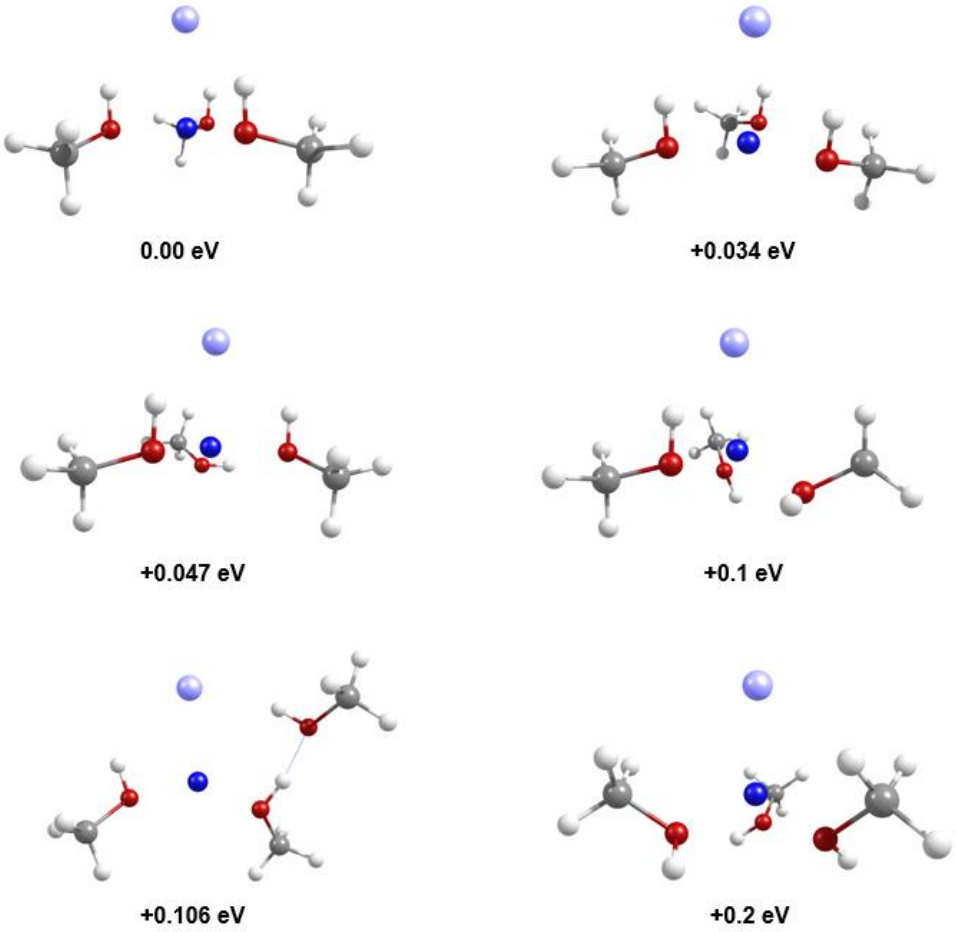

Figure 5.7. Calculated equilibrium structures for $LiI(CH_3OH)_3$ along with their energies (not corrected for zero point energy) in eV relative to the global potential energy minimum.

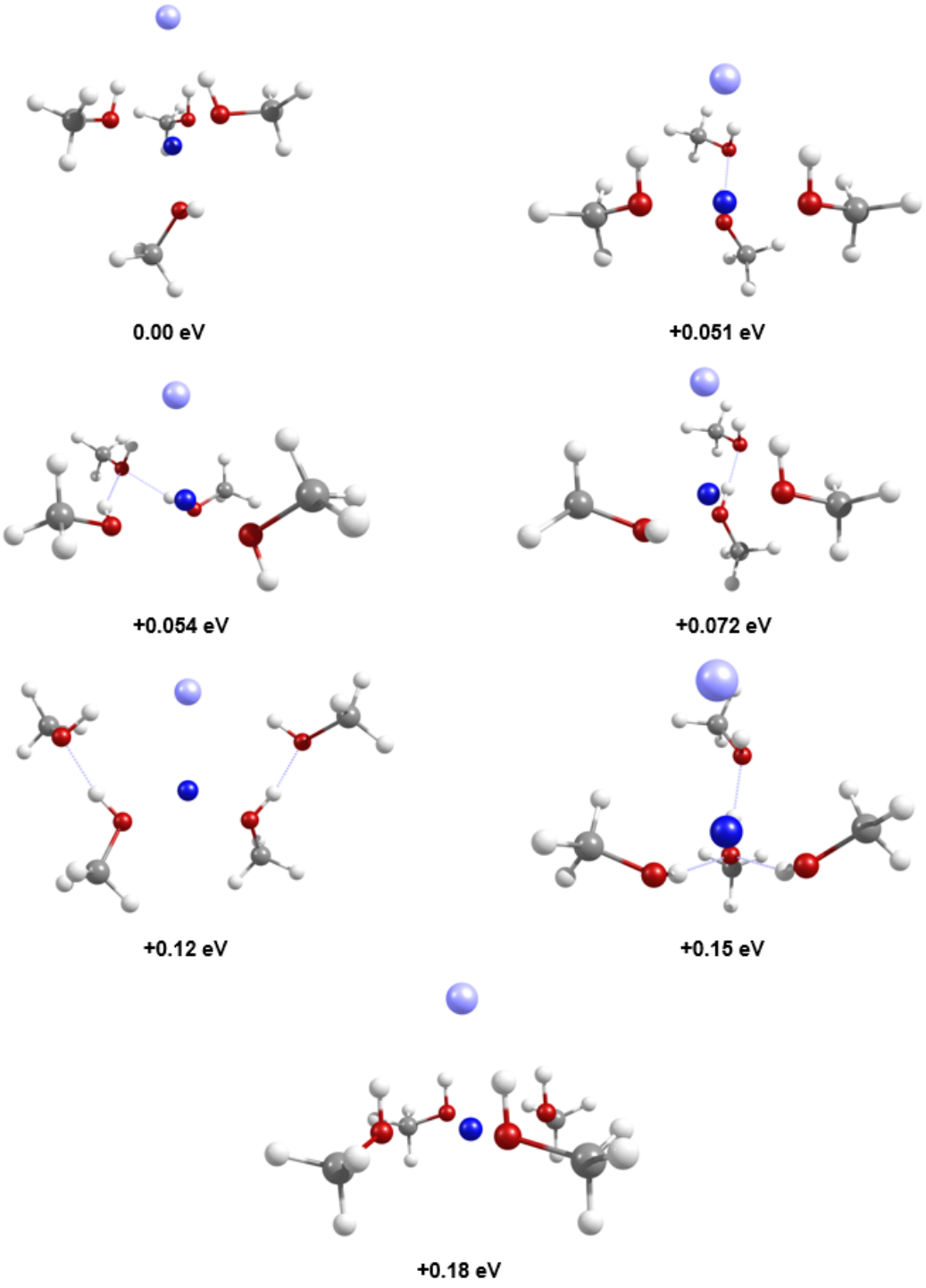

Figure 5.8. Calculated equilibrium structures for $LiI(CH_3OH)_4$ along with their energies (not corrected for zero point energy) in eV relative to the global potential energy minimum.

5.4.3 Assignment of IR spectra: OH stretching region

Figure 5.2 shows the IR spectra obtained by detecting $(CH_3OH)Li^+$, $(CH_3OH)_2Li^+$, $(CH_3OH)_3Li^+$ and $(CH_3OH)_4Li^+$ ions. For the first three ions the IR spectra show a dominant narrow band in the bonded OH stretching region. As the ion mass increases there is increasing evidence of broad underlying absorption features and these become dominant for $(CH_3OH)_4Li^+$, although a sharp peak is still seen for this ion. The positions of the bands are summarized in Table 5.1. In assigning the uncharged spectral carrier it has been assumed that no ion fragmentation has occurred, other than loss of an iodine atom: this assumption will be justified later.

Table 5.1. Positions and assignments of OH stretching bands for $LiI(CH_3OH)_n$ for n = 1-4.

Band position/cm^{-1}	Assigned carrier
3405	$LiI(CH_3OH)$
3340	$LiI(CH_3OH)_2$
3241 3327 3380	$LiI(CH_3OH)_3$
3241 3387 3327	$LiI(CH_3OH)_4$

The absorption bands of $LiI(CH_3OH)_n$ are red shifted from the OH stretching band of the isolated methanol molecule.[94] A similar red shift was seen in the IR spectra of $NaCl(CH_3OH)_n$ clusters (see Chapter Three) and indicated the formation of ionic hydrogen bonds, which weaken the OH bonds and thereby lower the OH stretching frequencies.

The IR spectrum derived from measuring the depletion of the lightest ion, $(CH_3OH)Li^+$, can be seen in Figure 5.2 (a). The possibility of ion fragmentation has been considered but if methanol molecules were easily lost then we might expect to see an IR depletion spectrum in the Li^+ mass channel, but no such spectrum was observed. As a result the IR spectrum of the simplest neutral complex, $LiI(CH_3OH)$, must be contained within the spectrum shown in Figure 5.2(a). Given that this spectrum is dominated by a single sharp band at 3405 cm^{-1} in the OH stretching region, we assign this band to $LiI(CH_3OH)$.

5.4.3.1 *Assignment of LiI(CH_3OH)*

The simplicity of the IR spectrum of LiI(CH_3OH) suggests that only one isomer of this complex is formed in helium nanodroplets. Both of the calculated isomers shown in Figure 5.5 have been considered as possible carriers of the spectrum. Of the two, it is the higher energy minimum that actually provided the better agreement with experiment. In both cases we expect a single band in the OH stretching region. For the global minimum structure we require a very small scaling factor to bring experiment into agreement with the MP2 prediction. A small scaling factor of 0.895 is also needed for the higher energy isomer but this scaling factor is nevertheless considerably larger than that required for the global minimum. For this reason our preference is for an assignment to the higher energy isomer.

5.4.3.2 *Assignment of LiI($CH_3OH)_2$*

The MP2 calculations found a global minimum structure for LiI$(CH_3OH)_2$ in which each methanol molecule is independently bonded to the LiI via two IHBs. Consequently, two bonded OH stretching vibrations, one symmetric and one antisymmetric combination, are expected for this structure. The calculations predict that the symmetric stretch gives the stronger of the two bands, as can be seen in Figure 5.2(b) beneath the experimental spectrum recorded in the $(CH_3OH)_2Li^+$ mass channel. Also, the antisymmetric stretch is predicted to be only 4 cm^{-1} to the red of the symmetric stretching band. Thus we anticipate only one observable IR band for this isomer given that the peak at 3340 cm^{-1} in Figure 5.2(b) has a full-width at half maximum of 10 cm^{-1}. The OH stretching band of LiI$(CH_3OH)_2$ is red-shifted 65 cm^{-1} from the band seen for LiI(CH_3OH). According to the *ab initio* calculations the red-shift should be 45 cm^{-1}, so this is not unreasonable. The MP2 calculations predicted another isomer which is only 0.037 eV above the global minimum structure. This higher energy isomer has no IHBs but there are hydrogen bonds between CH groups and the iodide in each methanol. This structure has two ‘free’ OH groups which delivers high intensity OH stretching band for the symmetric vibration at 3500 cm^{-1}. The antisymmetric vibration predicted a weak band at 3499 cm^{-1} which would clearly be too close to the strong symmetric band to resolve. The predicted band at 3500 cm^{-1} is 160

cm^{-1} above the experimental band at 3340 cm^{-1}. This is a large difference and therefore this isomer was ruled out as a potential contributor to the spectrum. The other two isomers show two bands in the bonded OH stretching region. The isomer that has an energy 0.041 eV higher than the global minimum structure has peaks predicted at 3335 and 3502 cm^{-1}. The even higher energy isomer has two bands predicted at 2952 and 3251 cm^{-1}. Clearly, none of these high energy isomers give a band structure in agreement with the experimental band at 3340 cm^{-1}. Consequently, these isomers have been excluded from the assignment.

5.4.3.3 *Assignment of LiI(CH$_3$OH)$_3$*

The IR spectrum recorded in the $(CH_3OH)_3Li^+$ mass channels is shown in Figure 5.2(c). The spectrum has a sharp band in the bonded OH stretching region at 3380 cm^{-1}. The MP2 calculations predict a global minimum structure for $LiI(CH_3OH)_3$ in which all methanol molecules are independently bonded to the LiI and form equivalent IHBs. Two OH stretching vibrations are expected and one will dominate (see MP2 prediction in Figure 5.2(c)). The strongest band in the calculated $LiI(CH_3OH)_3$ IR spectrum is about 65 cm^{-1} to the red of the experimental band in the m = 3 mass channel. Also, the difference between the two OH stretching bands in the calculated spectrum is 10 cm^{-1} while the full-width at half maximum of the single experimental band is about 20 cm^{-1}. Consequently, both OH stretching bands could be unresolved within the experimental band. The other predicted structures are ignored because they have several OH bands in the bonded OH stretching region that cannot possibly fit with the observed IR spectrum.

5.4.3.4 *Assignment of LiI(CH$_3$OH)$_4$*

The IR spectrum recorded in the $(CH_3OH)_4Li^+$ mass channel is shown in Figure 5.2(d). A narrow band was seen in the bonded OH stretching region at 3387 cm^{-1}, in addition to some much broader absorption features both sides of this sharp peak with a significant two broad bands peak at 3241 and 3327 cm^{-1}. The MP2 calculations predict seven local minima structures within 0.18 eV of the global minimum of $LiI(CH_3OH)_4$, as seen in Figure 5.8. The predicted IR contributions from each of these isomers are shown in Figure 5.2(d) beneath the

experimental IR spectrum. The structure most compatible with experimental band at 3387 cm^{-1} is the highest energy structure, which lies 0.18 eV above the global minimum structure. This structure has four equivalent IHBs which hold the methanol molecules to the LiI in a single solvation shell. Two OH stretching vibrations are predicted and one will dominate with a much higher intensity because it reflects the symmetric vibrational frequencies of four OH bonds. The calculated band for the chosen isomer is about 48 cm^{-1} to the red of the experimental band of $LiI(CH_3OH)_4$. Thus the sharp band might arise from a structure that has four equivalent IHBs, although this assignment is tentative. The two broad bands that peak at 3241 and 3327 cm^{-1} are assigned to overlapping contributions from larger complexes. This assignment was suggested due to the sharp features that seen obviously in IR spectra of n = 5 and 6 which entirely analogous to these two broad bands. Another possibility is that multiple isomers for $LiI(CH_3OH)_4$ cause the broad bands. The simulations beneath the experimental spectrum illustrates that contributions from multiple isomers span across the absorption range of 3100-3500 cm^{-1} and therefore provide a reasonable explanation for the spectral broadening.

5.4.3.5 *Assignment of $LiI(CH_3OH)_n$ n=5 and 6*

There is a significant lower S/N ratio observed in the IR spectra recorded from detection of $(CH_3OH)_5Li^+$ to $(CH_3OH)_6Li^+$ when compared with lighter ions (see Figures 5.3(a) and (b)), which is simply explained by the low absolute signal intensities in the m = 5 and 6 mass channels. The two broad absorption features in the m =3 and 4 spectra are seen also in the OH stretching region of the m = 5 and 6 IR spectra. The maximum absorption peaks at 3260 and 3365 cm^{-1} for $LiI(CH_3OH)_5$ and at 3270 and 3385 cm^{-1} for $LiI(CH_3OH)_6$. The broadening in the OH stretching region can be attributed to the presence of overlapping bands from multiple isomers for $LiI(CH_3OH)_n$ for n = 5 and 6 and from larger complexes owing to ion fragmentation. This trend of overlapping in the IR spectra of large complexes in the OH stretching region has been seen in previous studies [67, 95] and also in the previous two chapters. It therefore seems likely that $MX(solvent)_n$ complexes ($n \geq 4$) tend to give multiple isomers in the helium nanodroplet environment.

5.4.4 Assignment of IR spectra: CH stretching region

No bands were seen for $LiI(CH_3OH)_n$ complexes in the CH stretching region. According to the MP2 calculations, the CH bands intensities should be about 8% of those of the strongest bonded OH stretching bands. Comparing with intensity of CH stretching bands of $NaCl(CH_3OH)_n$ complexes in Chapter Three, the DFT calculations there predicted the intensity of the CH stretching band in about 15% of the OH predicted stretching bands. The absence of CH stretching bands for $LiI(CH_3OH)_n$ complexes may therefore be a consequence of the combination of a poor S/N ratio and the weaker intrinsic line strength for the CH stretching bands in $LiI(CH_3OH)_n$ complexes.

5.5 Conclusions

Infrared spectra have been recorded for the first time for $LiI(CH_3OH)_n$ complexes. These IR spectra, recorded when the complexes were isolated in helium nanodorplets, show clear absorption features in the OH stretching region. Narrow vibrational bands are seen in the bonded OH stretching region for n = 1- 4, which seem to be indicative of the formation of ionic hydrogen bonds in these complexes. For larger complexes (n > 4), broad absorption bands are seen which are assumed to arise from contributions from multiple isomers existing in the liquid helium environment. This trend of forming different isomers for $n \geq 4$ in helium nanodroplets were seen in this work in Chapters Three, Four and Five. The possible reasons for this trend could be derived from the complexity of the potential energy landscape of these complexes as a result of the numerous possible isomers, in addition to the very rapid cooling that traps the isomers in local minima energy inside helium nanodroplets. This behaviour is not possible in the smaller complexes (n=1-3) because they don't have similar local minima of isomers. Also, the formation of the isomers within the helium nanodroplet could be more controlled by dipole-dipole interactions than by energies of local minima of the isomers. Therefore, the distribution of isomers within the helium nanodroplet might not follow those based on gas phase calculations hence making the assignment of the recorded spectra extremely difficult.

CHAPTER 6

Mass Spectrometric Study of a range of Salt-Solvent Complexes in Helium Nanodroplets

6.1 Introduction

Infrared spectra of complexes of NaCl and LiI with the solvents water and methanol were reported in Chapters Three, Four and Five of this thesis. However, there is potential to explore other alkali halides and other solvents via IR spectroscopy with the techniques described in this thesis. Such studies represent a major and lengthy research programme and are beyond the scope of this thesis. However, such studies would be potentially very exciting for several reasons. Variation of the type of salt would allow the effect of cation and anion sizes to be controlled and explored. Equally, by varying the solvent, we would also be able to see how these ion-pairs behave in both protic solvents (water, methanol, etc.) and aprotic solvents (acetone, acetonitrile, etc.). It would also be possible to explore the effect of solvent polarity on the behaviour of the ions.

Before instigating new IR studies, it would be useful to investigate the evaporation characteristics of the various alkali halides, their pick-up by helium nanodroplets, and the prospects for forming complexes with other solvents. This preliminary type of study can be carried out efficiently with mass spectrometry. Indeed, we have seen in previous chapters that recording mass spectra is an essential precursor to recording IR spectra of salt-solvent complexes and this chapter reports the findings from this survey work.

A significant range of salts were chosen for this study, namely NaCl, NaBr, NaF, NaI, LiI, LiCl, CsI and KF. The solvents chosen were water, methanol, acetone and acetonitrile, *i.e*. two protic and two aprotic solvents. The results from the mass spectral work will be presented in this chapter after a description of the apparatus and the general procedure used.

6.2 Experimental Apparatus

The apparatus used for recording the mass spectra of salt-solvent complexes described in this chapter has similarities to that described in the earlier chapters, but also some differences. As detailed below, the main difference is the use of a time-of-flight mass spectrometer (TOF-MS) rather than a quadrupole system. The components of this alternative helium nanodroplet apparatus are therefore described before presenting the findings.

6.2.1 An overview of helium nanodroplet system

Full details of this apparatus has been described in several publications from our research group at the University of Leicester.[127-130] The entire system consists of three vacuum chambers, as illustrated in Figure 6.1. These chambers consist of a source chamber, a pickup chamber and an analysis chamber. The vacuum system contains two pneumatic gate valves. One of these gate valves is located between the pick-up chamber and the analysis chamber, while the other is placed between the diffusion pump and the helium source.

Helium nanodroplets were formed in the source chamber by passage of pre-cooled ultrahigh purity helium (99.9999%) through a 5 μm pinhole aperture into the vacuum. The pre-cooling was achieved using a closed-cycle cryostat (F-50, Sumitomo Heavy Industries) and the helium stagnation pressure was fixed at 20 bar for all of the experiments described in this chapter. Due to problems with the diode temperature sensor the temperature of the helium was unknown for the experiments reported in this chapter (unlike in the earlier chapters) but conditions were chosen which gave the best quality mass spectra. Because of the faulty diode the nozzle temperature readout was artificially low but was nevertheless kept at a steady value by a heater placed behind the nozzle pinhole, which was controlled using a LakeShore 331 unit.

After passing through 0.5 mm diameter nickel skimmer, the helium nanodroplets travelled through two pick-up cells, the first containing MX salt vapour and the second solvent vapour. MX vapour was produced by resistively heating a pick-up cell containing the solid salt. The details of the heating system were described in section 2.1.2.1 and the system used for the experiments described in this chapter

was identical. For the solvent, the liquid was first degassed using the freeze-pump-thaw technique. This entailed freezing the solvent using liquid nitrogen and then pumping off residual gases for 10 minutes. This process was repeated three times before starting each experiment. The solvent partial pressures in the pickup cells were typically in the range of 10^{-6} mbar.

In the analysis chamber, a reflectron (TOF-MS) mass spectrometer equipped with an electron ionization source is mounted vertically on top of this chamber. Time-of-flight mass spectra were collected using a microchannel plate detector and the signal was then sent to a digital oscilloscope. The mass spectrum was then transferred to a PC via specially-written LabView (version 2015) software. The main function of this software is to collect and process the data from the oscilloscope to produce a mass spectrum.

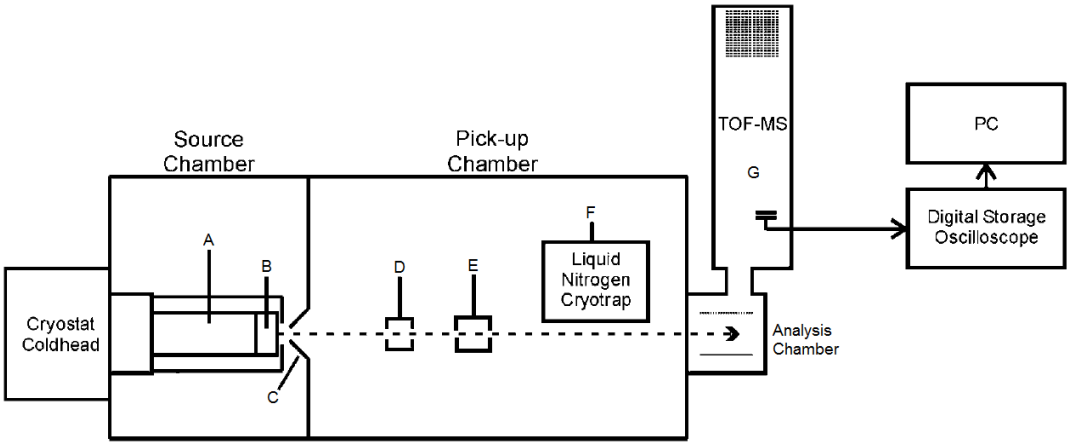

Figure 6.1. Schematic diagram showing the three vacuum chambers of the helium nanodroplet apparatus. (A) Cold head, (B) pinhole aperture, (C) 0.5 mm nickel skimmer, (D) evaporator oven, (E) solvent pickup cell, (F) cryo-trap (77 K), (G) reflectron TOF-MS mass spectrometer. Reprinted from ref [130].

6.2.2 Vacuum system

The vacuum in the source chamber was provided by a diffusion pump (Varian VHS-250) connected to a water-cooled baffle to minimise oil back-streaming. This pump is backed by a roots pump (Edwards-EH250) combined with a two-stage rotary vane pump (Edwards-E2M40).

In the pickup chamber, the vacuum is pumped by a 900 L/s turbomolecular pump (Agilent TV 1001 NAV) backed by a rotary pump (Varian DS402). This pumping system achieves a chamber base pressure in the region of 7×10^{-8} mbar, rising to 8×10^{-7} mbar when the gate valve linking the source chamber is open.

The TOF-MS chamber is pumped by a 380 L/s turbomolecular pump (Leybold Turbovac 361) backed by a rotary pump (Varian DS102). This pumping system achieves a chamber base pressure of about 8×10^{-10} mbar, rising to 2×10^{-9} mbar when the gate valve is open to admit helium nanodroplets.

6.2.3 Time-of-flight mass spectrometer

The time-of-flight mass spectrometer (TOF-MS) used here is a reflectron design and was built by Kore Technology (Ely, UK). It has a typical mass resolution ($m/\Delta m$) of 3000.[130] The electron energy of the TOF-MS in all of the experiments described in this chapter was in the region of 75 eV and was not adjusted.

The concept of a reflectron TOF-MS was first proposed by Mamyrin[131] to improve the mass resolution of the first truly useful TOF-MS, which was designed by Wiley and McLaren.[132] A schematic of a Wiley-McLaren TOF-MS design can be seen in Figure 6.2. This diagram shows a molecular beam entering the ionization region between the cathode (repeller) and grid electrodes. An ionization source is needed, which consist of an electron impact source, as indicated in the figure 6.2. Ions are then accelerated between the two plates as a result of the repulsion force, but the acceleration will not be accrued from the same location. Therefore, a second accelerator zone is added in the Wiley-McLaren design to correct the difference in the kinetic energies of ions arising from these different locations. The ions after the accelerator travel to the detector which is located at the end of the drift region. Consequently, ions which have different *m/z* are separated according to their velocities when they drift in a free-field region (from the accelerator to detector) through unidirectional journey.

The mass resolution in the linear TOF is affected by several factors that create a distribution in flight times between ions that have same *m*/*z* ratio. The length of the ion formation pulse is one of these factors, in addition to the variation of the initial kinetic energy of the ions that have the same *m*/*z*, and the stability of the

voltages applied to the various electrodes.[133] Therefore, to reduce the distribution in the flight time of ions that have same *m/z*, and instead of a unidirectional journey for the ions in the linear TOF-MS introduced by Wiley and McLaren, the reflectron incorporates an electrostatic reflector.

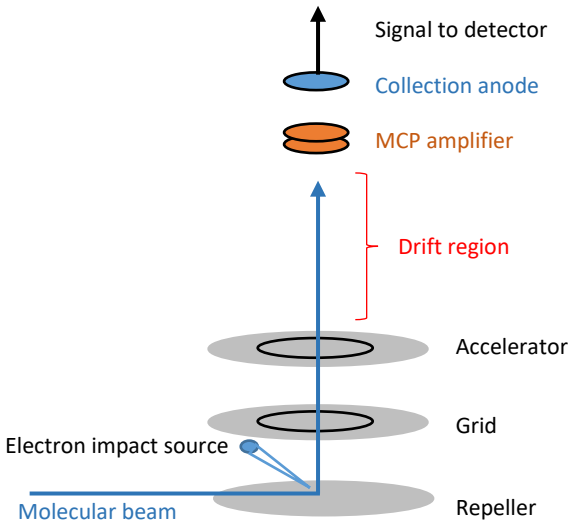

Figure 6.2. Schematic showing the Wiley and McLaren Linear TOF-MS.

Figure 6.3 illustrates the basic structure of a reflectron TOF-MS. Basically, the reflector consists of a series of grid electrodes or ring electrodes which provide a gradually changing electrostatic potential. The reflector array is located on the opposite side of the field-free region from the ion source. The detector is positioned on the same side as the ion source of the ion to capture the arrival of ions after they are reflected, as shown in Figure 6.3.[131]

Figure 6.3 shows two ions having the same mass. The fast ion (●) has mass with correct kinetic energy. The other ion (○) has the same mass and travels in the same direction but with a lower kinetic energy. The total flight length for the ions will be approximately (L1+L2), where L1 and L2 are the flight region lengths before and after the reflectron array. Basically, the reflectron creates a homogeneous reflected electrostatic field at roughly the mid-point in the ion's journey towards the detector. This electrostatic field is chosen to be repulsive and sufficiently large to reflect the ions back in the direction they came (roughly), hence the name reflectron. The slow ion in the figure (○) reaches the reflectron later than the fast ion which penetrate further in the reflecting field, and by using

properly chosen voltages, the reflectron will correct the initial kinetic energy of both ions, fast (●) and slow (○), and reflect them to reach the detector at the same time and thus increase the mass resolution.[133, 134]

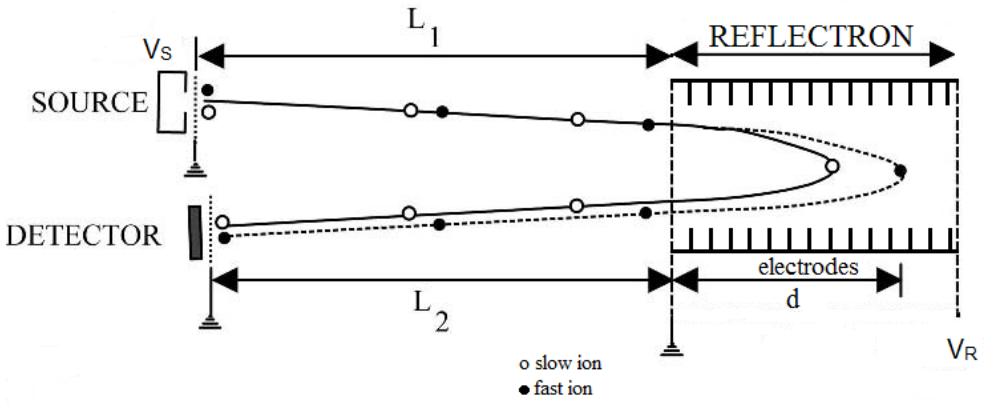

Figure 6.3. Schematic showing the reflectron TOF-MS and possible trajectories of ions with the same mass and different initial kinetic energies.

6.3 Results and Discussion

6.3.1 Mass spectra of NaX-solvent complexes

The presentation of the results from these experiments begins with the sodium halides, partly because NaCl was met in Chapter Three and so there is some overlap with the discussion there. The chosen salts were NaF, NaCl, NaBr and NaI. The main reason for studying these salts is they may allow the exploration of the effect of the halide on the ability to form contact ion-pair (CIP) and separated ion-pair (SIP) complexes in subsequent IR spectroscopy experiments.

Before describing specific mass spectra, some general features of the mass spectra are first identified. At low masses (m/z < 100) a series of peaks arising from He_n^+ ions can be seen with their characteristic spacing of 4 mass units between successive peaks. These were met in earlier chapters. Series of ions also arise from solvent clusters. For water and methanol, a series of protonated water $(H_2O)_nH^+$ and protonated methanol $(CH_3OH)_nH^+$ ions, respectively, are seen in the mass spectra. For acetone and acetonitrile, acetone cluster ions, $((CH_3)_2CO)_n^+$ and acetonitrile cluster ions $(CH_3CN)_n^+$, are seen. Presumably these ions come from ionization of those helium nanodroplets that contain solvent molecules but no salt molecules. These types of ions are common to all of the

mass spectra and so any comments about these ions in what follows will be minimal.

Mass spectra from $NaCl(H_2O)_n$ complexes in helium nanodroplets have been recorded and published previously by our research group.[67] For $NaCl(CH_3OH)_n$, the mass spectrometry in helium nanodroplets was discussed in Chapter Three (see Figure 3.1) in this thesis and also published recently.[114] Those mass spectra were recorded using quadrupole mass spectrometry on a different apparatus to that used for the work in this chapter. Nevertheless, the mass spectra are essentially the same and so are discussed no further here. Instead the focus here for NaCl is on the interaction of this salt with acetone and acetonitrile, two aprotic solvents.

The mass spectrum obtained with NaCl and acetone is shown in Figure 6.3. Several ions are seen in this spectrum which can be assigned by comparison with the known mass spectrum of acetone in the gas phase, in addition to those already mentioned above. As well as the parent ion at *m*/*z* 58 and its clusters, which were already mentioned above, a signal is seen at *m*/*z* 43, which derives from the acylium ion $(CH_3CO)^+$. This ion is a fragment from the ionization of acetone. The peak with the blue asterisk at *m*/*z* 100 is from the 2-hexanone ion $(CH_3(CH_2)_3COCH_3)^+$, which is produced by ejection of an O atom from the acetone dimer and subsequent ion rearrangement.[135]

The most prominent series of sodium-containing ions are from $((CH_3)_2CO)_mNa^+$. These ions presumably originate from the ionization of $NaCl((CH_3)_2CO))_m$ complexes inside helium nanodroplets, with the Cl atom being ejected before detection (as was the case with water and methanol as solvents). The series marked with blue labels refers to $((H_2O)(CH_3)_2CO)_mNa^+$ ions, which presumably derive from the ionization of mixed water-acetone clusters. The presence of water could result from the degassing of water from the vacuum system. In the mass spectrum in Figure 6.4 we can see ions with *m* up to at least 6 and this could easily be extended to higher solvent numbers by increasing the quantity of acetone in the second pick-up cell. Note that there is no evidence for $((CH_3)_2CO)_mNa_2Cl^+$ ions, which might be expected if there was a significant quantity of $(NaCl)_2$ dimers in the helium nanodroplets.

For NaCl with acetonitrile in helium nanodroplets, the mass spectrum in Figure 6.5 shows two series of peaks. One of these series is assigned to the ionization of pure acetonitrile clusters while the other derives from $(CH_3CN)_mNa^+$ (m =1-6) ions, which are the products of ionization of $NaCl(CH_3CN)_n$ complexes. We therefore conclude that we can successfully make both $NaCl((CH_3)_2CO))_n$ and $NaCl(CH_3CN)_n$ complexes in helium nanodroplets and the scene is now set for future IR spectroscopy experiments on these complexes.

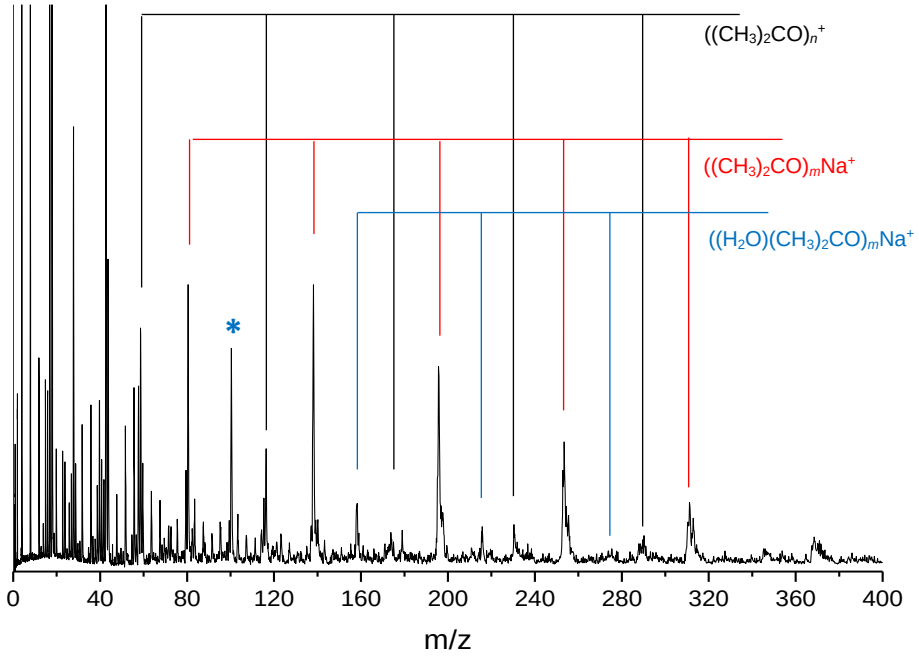

Figure 6.4. Mass spectrum from the $NaCl/(CH_3)_2CO$ system obtained using an electron energy of 75 eV. The temperature of the pick-up cell containing NaCl was 378 °C.

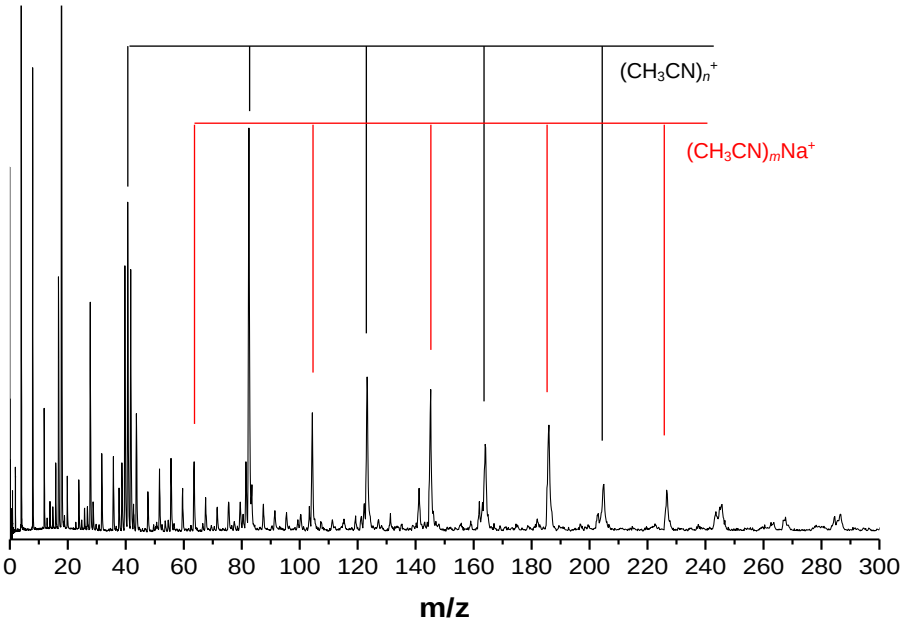

Figure 6.5. Mass spectrum from the NaCl/CH_3CN system obtained using an electron energy of 75 eV. The temperature of the pick-up cell containing NaCl was 363 °C.

The mass spectrum from $NaBr(H_2O)_n$ complexes is shown in Figure 6.6. There are two series of peaks in this figure. The black series signifies protonated water cluster ions, while the red highlighted signals are assigned to $(H_2O)_mNa^+$ (m = 1-14). The latter are assigned to the ionization products of neutral $NaBr(H_2O)_m$ complexes in helium nanodroplets. This behaviour is similar to that previously observed for $NaCl(H_2O)_m$ complexes.

For methanol the mass spectrum is shown in Figure 6.7. Two highlighted series can be seen in the spectrum in addition to the protonated methanol cluster ions. The red highlighted peaks are assigned to $(CH_3OH)_mNa^+$ (m = 1-7) ions and the blue series refers to $(H_2O)(CH_3OH)_nH^+$ (n = 1-7). The $(CH_3OH)_mNa^+$ ions are attributed to ionization of $NaCl(CH_3OH)_m$ clusters, while the $(H_2O)(CH_3OH)_nH^+$ ions are presumably derived from mixed water-methanol clusters. The methanol was very pure (99.9999%, Sigma-Aldrich) and therefore the water presence in the system is most likely from the degassing of water from the walls of the vacuum system.

Figure 6.8 shows the mass spectrum for a NaBr/acetone mixture. The red highlighted series of peaks are from $((CH_3)_2CO)_mNa^+$ (m =1-5) ions and the blue series derive from mixed water-acetone clusters with NaCl salt to produce $((H_2O)(CH_3)_2CO)_nNa^+$(n = 1-3). The $((CH_3)_2CO)_mNa^+$ ions are the products from ionization of neutral $NaBr((CH_3)_2CO)_m$ complexes.

Three series of peaks can be seen in the NaBr/acetonitrile mass spectrum shown in Figure 6.9. One of these series (the black one) is from pure acetonitrile clusters while the $(H_2O)(CH_3CN)_nH^+$ ions are presumably the result of a small water contamination from the vacuum system. $NaBr(CH_3CN)_m$ ionizes to produce $(CH_3CN)_mNa^+$ ions, which are readily detected.

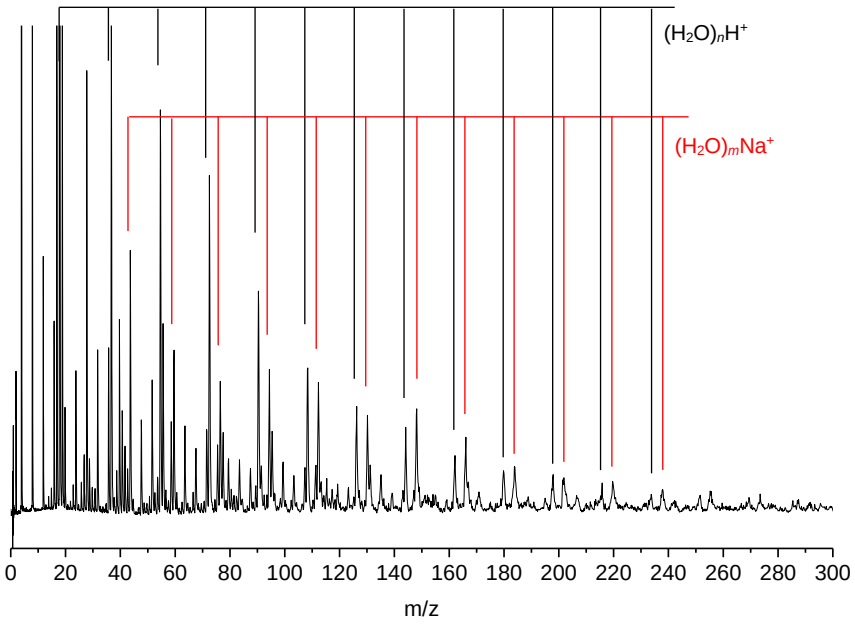

Figure 6.6. Mass spectrum from the $NaBr/H_2O$ system obtained using an electron energy of 75 eV. The temperature of the pick-up cell containing NaBr was 351 °C.

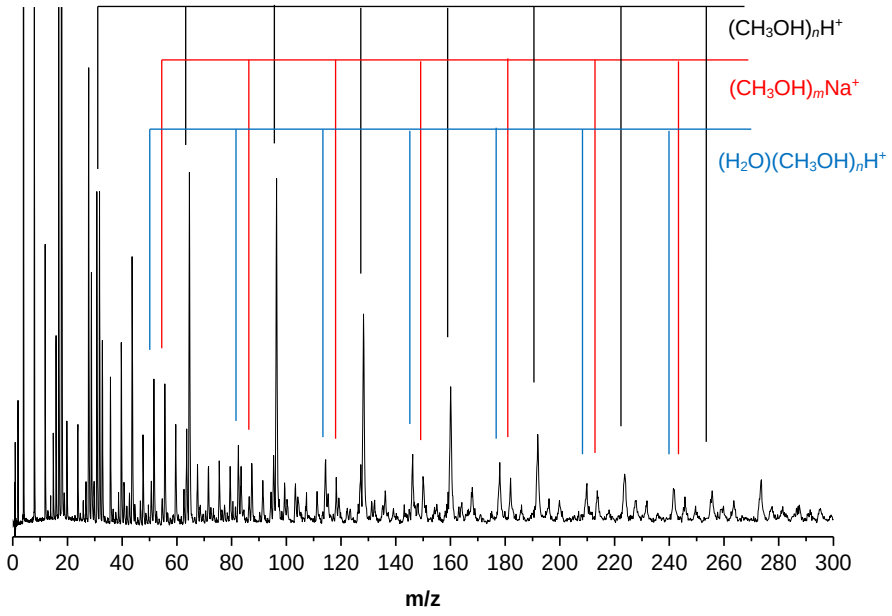

Figure 6.7. Mass spectrum from the NaBr/CH_3OH system obtained using an electron energy of 75 eV. The temperature of the pick-up cell containing NaBr was 351 °C.

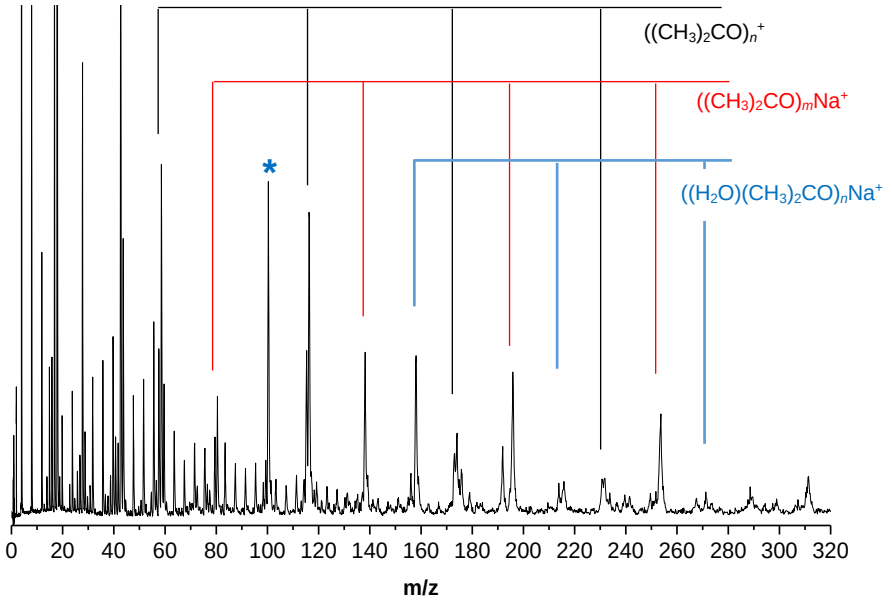

Figure 6.8. Mass spectrum from the NaBr/$(CH_3)_2CO$ system obtained using an electron energy of 75 eV. The temperature of the pick-up cell containing NaBr was 353 °C.

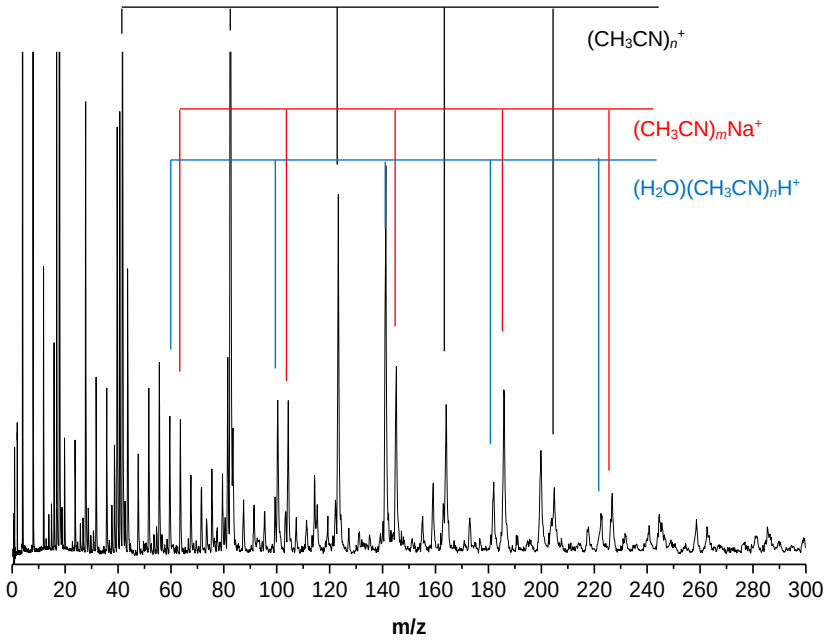

Figure 6.9. Mass spectrum from the NaBr/CH_3CN system obtained using an electron energy of 75 eV. The temperature of the pick-up cell containing NaBr was 353 °C.

Figures 6.10, 6.11, 6.12 and 6.13 show the mass spectra from NaF complexes with water, methanol, acetone and acetonitrile, respectively. These spectra have essentially the same appearance as for the corresponding NaCl-solvent and NaBr-solvent complexes. Likewise, there is no significant difference in the mass spectra of sodium iodide/solvent complexes when compared with the mass spectra from the other sodium halides and so these spectra are not shown here.

To summarise, the pick-up behaviour and subsequent ionization process for NaX-solvent complexes in helium nanodroplets is essentially the same for all of the salts and all of the solvents chosen for investigation. The contribution from the salt monomer clearly dominates, *i.e*. the main ions seem to come from $NaX(solvent)_n$ complexes, and on ionization these yield $(solvent)_nNa^+$ ions.

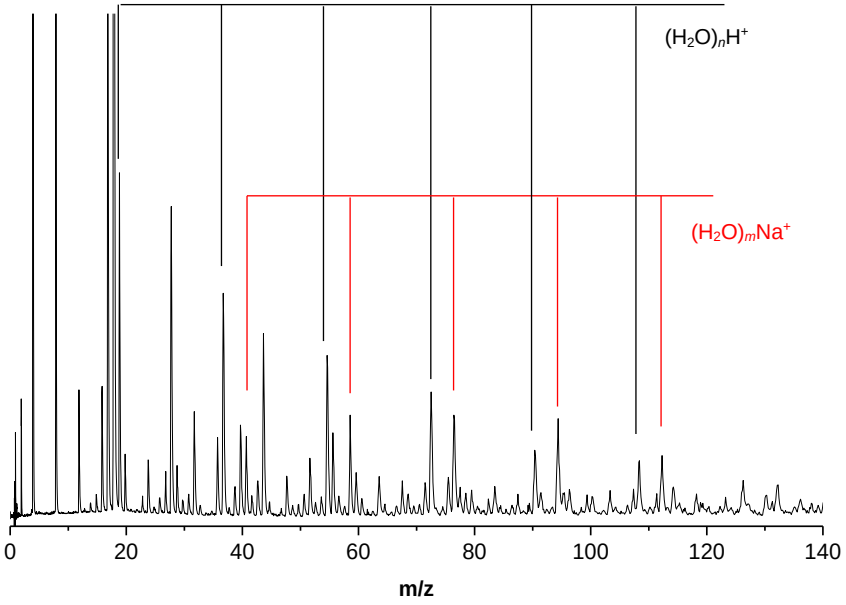

Figure 6.10. Mass spectrum from the NaF/H_2O system obtained using an electron energy of 75 eV. The temperature of the pick-up cell containing NaF was 467 °C.

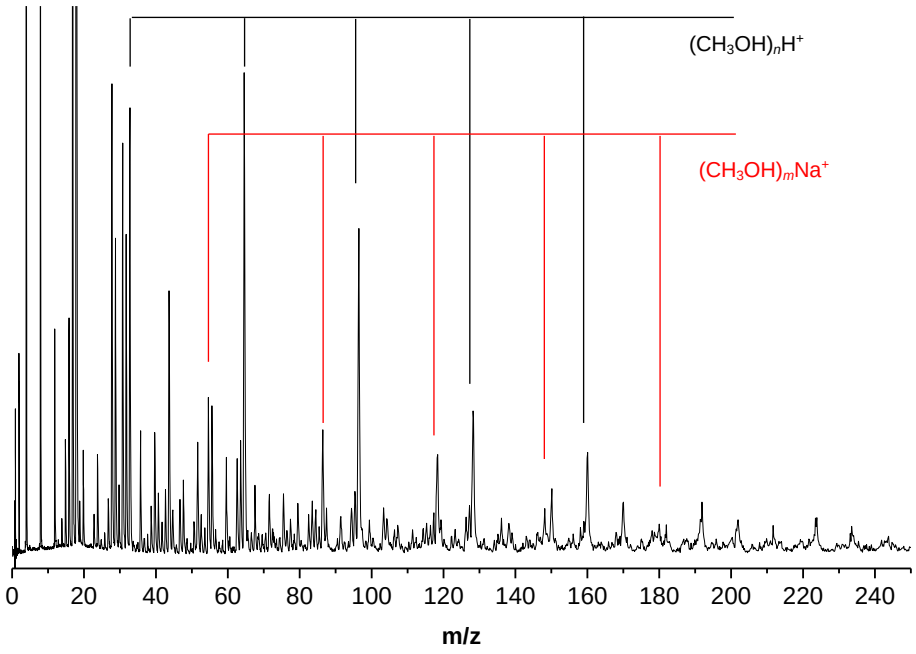

Figure 6.11. Mass spectrum from the NaF/CH_3OH system obtained using an electron energy of 75 eV. The temperature of the pick-up cell containing NaF was 473 °C.

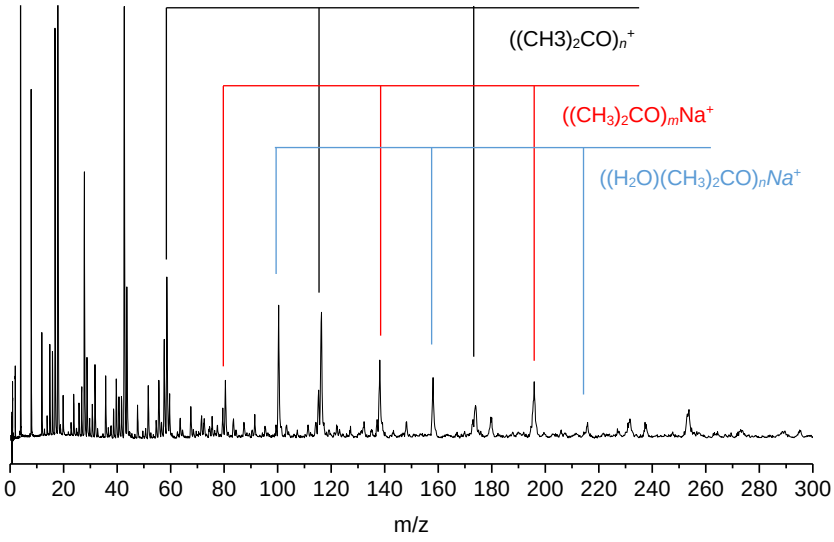

Figure 6.12. Mass spectrum from the NaF/$(CH_3)_2CO$ system obtained using an electron energy of 75 eV. The temperature of the pick-up cell containing NaF was 470 °C.

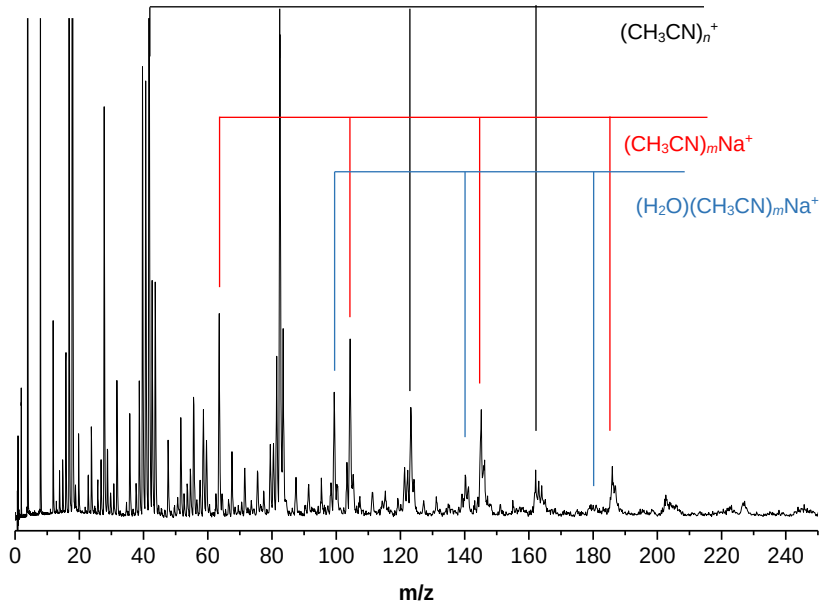

Figure 6.13. Mass spectrum from the NaF/CH_3CN system obtained using an electron energy of 75 eV. The temperature of the pick-up cell containing NaF was 453 °C.

6.3.2 Mass spectra of other MX-solvent complexes

Two lithium halides, LiI and LiCl, in addition to KF and CsI, were chosen for study as examples of salts with a range of different sized anions and cations.

The mass spectra of LiI complexes with water and methanol have already been discussed in this thesis in Chapters Four and Five, respectively, where QMS was used. In this chapter, the mass spectra of LiI complexes with water and methanol obtained via TOF-MS experiments will be briefly shown. Also, the mass spectra of LiI-acetone and LiI-acetonitrile complexes will be reported. The findings will then be compared with those from a different lithium-containing salt, LiCl.

The mass spectrum from a LiI/H_2O mixture in helium nanodroplets was recorded. The key features of the spectrum are summarized in Table 6.1. The same series of weak peaks that were seen in Figure 4.1 were also found in the work reported in this chapter. However, an additional series of peaks which belong to $(H_2O)_mLi_2I^+$ ions were seen with higher intensity, comparing with the intensity of same series that observed in Chapter Four. This series was briefly discussed before in Chapter Four due to the focused was on recording the IR and mass spectra for only $LiI(H_2O)_n$ complexes. The $(H_2O)_mLi_2I^+$ ions presumably originate from the ionization of the neutral complexes between H_2O and the lithium iodide dimer, $(LiI)_2$. This additional series provides more evidence to the assignment of LiI dimer abundance in the LiI vapour that was discussed in details in Chapter Four. Ionization of the latter could yield the observed ions by the following process (ignoring the possibility of accompanying loss of water molecules):

$$Li_2I_2(H_2O)_m + e^- \rightarrow (H_2O)_mLi_2I^+ + I + 2e^- \qquad (6.1)$$

For LiI and methanol in helium nanodroplets the mass spectral findings are summarised in Table 6.1. In addition to the ions already reported in Chapter Five, we see a series arising from $(CH_3OH)_mLi_2I^+$ (m = 1-4). The source of the Li_2I^+ is the same as described above for the case of water. For LiI with acetone and acetonitrile, we see analogous products to those seen for the LiI with water and methanol with clear absence of $(solvent)_nLi_2^+$ ions, as summarised in Table 6.1.

The mass spectra of LiCl mixtures with water, methanol, acetone and acetonitrile are also shown in Table 6.1. No significant change was seen in these mass spectra, with the exception of the observation of $(H_2O)_nLi_2^+$ (n=1-6) and $(CH_3OH)_nLi_2^+$ ions in the experiments with water and methanol, respectively. The source of these ions is presumably the process illustrated in reaction (6.2) below.

$$Li_2Cl_2(H_2O)_m + e^- \rightarrow (H_2O)_mLi_2^+ + 2Cl + 2e^- \qquad (6.2)$$

The reason for the loss of two halogen atom, rather than the usual one, is unclear.

The mass spectra obtained from KF/solvent complexes were recorded and the key findings are summarised in Table 6.1. In addition to the same type of ions seen for other salts, we see for the first time the significant production of intact metal halide ions of the form KF^+, *i.e*. ejection of the F atom is not universal. In other words, ionization of KF(solvent)$_n$ can lead both to (solvent)$_nK^+$ and (solvent)$_nKF^+$. Figure 6.14 shows the mass spectrum of $KF(H_2O)_n$ as an example. This spectrum shows peaks from $(H_2O)_nK^+$ ions, marked with red labels, and $(H_2O)_nKF^+$ ions, shown with blue labels.

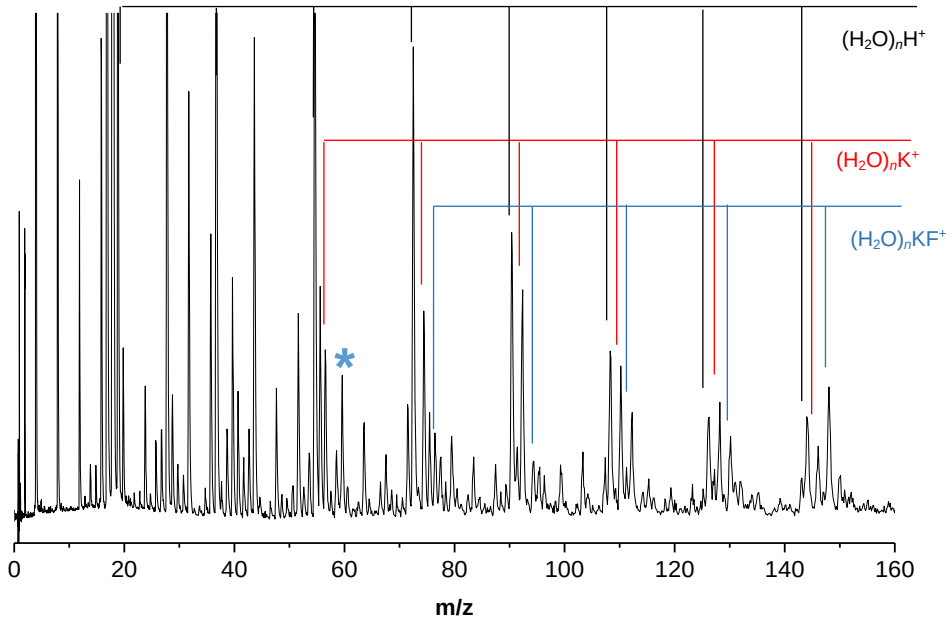

Figure 6.14. Mass spectrum from the KF/H_2O system obtained using an electron energy of 75 eV. The temperature of the pick-up cell containing KF was 418 °C. The blue asterisk refers to KF^+ ion at 59 *m/z*.

Caesium iodide is an example of an alkali halide where both the cation and anion are large. For CsI with water in helium nanodroplets, the mass spectra show two kinds of Cs-containing cluster ions, as summarised in Table 6.1. Peaks for Cs^+ and CsI^+ were seen in the mass spectrum. These ions were previously observed in the mass spectrum of CsI vapour at high temperature.[136] Two series of peaks assigned to $(H_2O)_mCs^+$ (m = 1-14) and $(H_2O)_mCsI^+$ (m = 1-14) ions were seen in the current study. The significant point in the mass spectrum of CsI-water complexes is the formation of larger complexes than for NaX and LiX salts, *i.e*. we see ions with more water molecules. This may result from the size of the CsI ion-pair, which will have a larger first solvation shell than smaller salts. However, it may also be a consequence of the larger size of the Cs^+, which can accommodate more water molecules in its first solvation shell.[137] It is therefore unclear whether the longer series of ions is a consequence of the properties of the neutral complexes or the increased stability of the resulting ions.

Table 6.1 also summarises the findings from the mass spectrometry of CsI-methanol mixtures in helium nanodroplets. The spectrum shows a series of peaks from $(CH_3OH)_mCs^+$ ions with m value up to 12. Another interesting series of peaks which had no analogue when water was used were from $(CH_3OH)_nCs_2I^+$ (n = 1-12). These ions must arise from $(CsI)_2$ with methanol in helium nanodroplets. Similar ions of $(solvent)_mCs^+$ and $(solvent)_nCs_2I^+$ were seen when acetone and acetonitrile were used (see Table 6.1). An obvious absence of $(solvents)_nCsI^+$ ions was observed in the mass spectra of CsI complexes with acetone and acetonitrile. Consequently, it could be concluded that water can stabilise the structure of $(H_2O)_nCsI^+$ ions more than the other solvents. The same can be concluded for $(solvent)_nCs_2I^+$ ions with methanol, acetone and acetonitrile which found to be more stable in these solvents than in water.

Table 6.1. The main series of ions detected in the mass spectra of several MX salts with water, methanol, acetone and acetonitrile.

	H_2O		CH_3OH		Acetone		Acetonitrile	
	Series of ions	**Intensity**	**Series of ions**	**Intensity**	**Series of ions**	**Intensity**	**Series of ions**	**Intensity**
LiI	$(H_2O)_mLi^+$ $(H_2O)_mLi_2^+$ $(H_2O)_nLi_2I^+$	(w) (m) (w)	$(CH_3OH)_mLi^+$ $(CH_3OH)_mLi_2^+$ $(CH_3OH)_nLi_2I^+$	(w) (m) (w)	$((CH_3)_2CO)_mLi^+$ $((CH_3)_2CO)_nLi_2I^+$	(w) (w)	$(CH_3CN)_mLi^+$ $(CH_3CN)_nLi_2I^+$	(w) (w)
LiCl	$(H_2O)_mLi^+$ $(H_2O)_nLi_2^+$	(s) (m)	$(CH_3OH)_mLi^+$ $(CH_3OH)_nLi_2^+$	(s) (m)	$((CH_3)_2CO)_mLi^+$	(s)	$(CH_3CN)_mLi^+$	(m)
KF	$(H_2O)_nK^+$ $(H_2O)_nKF^+$	(m) (w)	$(CH_3OH)_nK^+$ $(CH_3OH)_nKF^+$	(s) (m)	$((CH_3)_2CO)_nK^+$	(s)	$(CH_3CN)_nK^+$ $(CH_3CN)_nKF^+$	(s) (m)
CsI	$(H_2O)_mCs^+$ $(H_2O)_nCsI^+$	(s) (s)	$(CH_3OH)_mCs^+$ $(CH_3OH)_nCs_2I^+$	(s) (m)	$((CH_3)_2CO)_mCs^+$ $((CH_3)_2CO)_nCs_2I^+$	(s) (m)	$(CH_3CN)_mCs^+$ $(CH_3CN)_nCs_2I^+$	(s) (m)

s = strong
m = medium
w = weak

Table 6.2 summarises the oven temperatures used to record the mass spectra of all studied alkali halides. This is intended to provide a resource for future spectroscopic studies of these salts in combination with solvents. The trend in oven temperatures fits with the expected variation in the vapour pressures of the salts, as described in the literature.[138, 139] Essentially, evaporation becomes easier as the halide becomes heavier for a given choice of alkali ion. Thus there is a decrease in the alkali halide evaporation temperature (increase in the vapour pressure) by increasing the mass of the halide. For a given halide the sodium-containing salt requires the highest evaporation temperature and of the species studied in this chapter NaF requires the highest temperature to achieve significant evaporation.

Table 6.2. Evaporation temperature employed for various alkali halides. The values are averages of those used for each salt with different solvents.

Sodium halides	Temperature/°C
NaF	465
NaCl	370
NaBr	352
NaI	330
LiI	280
LiCl	348
KF	416
CsI	295

6.4 Conclusions

Mass spectra from a range of alkali halide complexes with protic and aprotic solvents in helium nanodroplets have been recorded. In all cases ions originating from $MX(solvent)_n$ complexes can be seen. These ions consist of $(solvent)_mM^+$ and $(solvent)_mMX^+$ ions. The former are the dominant ions and are produced by ejection of halogen atoms after ionization. The $(solvent)_mMX^+$ ions are generally far less abundant and for some salts are barely detected at all. Consequently, for IR depletion spectroscopy of $MX(solvent)_n$ complexes, it will make sense to focus on the detection of $(solvent)_nM^+$ ions.

For CsI and LiI, the dimer/solvent complexes seem to be significant, as evidenced by the detection of $(solvent)_mM_2X^+$ ions after electron ionization. The number of solvent molecules that are attached increased in line with the size of the alkali halide ion. Thus for CsI-H_2O complexes $(H_2O)_mCs^+$ ions with *m* up to 14 could be readily seen whereas for Li-H_2O complexes no more than 6 water molecules could be seen in $(H_2O)_nLi^+$ ions.

To summarise, this study has shown that a wide range of salt/solvent complexes can be formed in helium nanodroplets and their ions can successfully be observed using mass spectrometry. This now paves the way for new IR studies of the neutral complexes.

Publication List

1. J. Tandy, C. Feng, A. Boatwright, G. Sarma, A. M. Sadoon, A. Shirley, N. D. N. Rodrigues, E. M. Cunningham, S. Yang, and A. M. Ellis, *Communication: Infrared spectroscopy of salt-water complexes.* Journal of Chemical Physics, 2016. **144**(12): p. 121103.

2. A. M. Sadoon, G. Sarma, E. M. Cunningham, J. Tandy, M. W. Hanson-Heine, N. A. Besley, S. Yang, and A. M. Ellis, *Infrared spectroscopy of NaCl $(CH_3OH)n$ complexes in helium nanodroplets.* Journal of Physical Chemistry A, 2016. **120**(41): p. 8085-8092.

Bibliography

1. B. Conway, *Ionic hydration in chemistry and biophysics. 1981.* Studies in Physical and Theoretical Chemistry. **12**.

2. K. Weller, *Ion Solvation: Y. Marcus. Wiley, Chichester, New York, Brisbane, Toronto, Singapore,* 1988, Elsevier.

3. J. Burgess, *Ions in solution: basic principles of chemical interactions*. 1999: Elsevier.

4. A. Grossfield, P. Ren, and J.W. Ponder, *Ion solvation thermodynamics from simulation with a polarizable force field.* Journal of the American Chemical Society, 2003. **125**(50): p. 15671-15682.

5. E. Knipping, M. Lakin, K. Foster, P. Jungwirth, D. Tobias, R. Gerber, D. Dabdub, and B. Finlayson-Pitts, *Experiments and simulations of ion-enhanced interfacial chemistry on aqueous NaCl aerosols.* Science, 2000. **288**(5464): p. 301-306.

6. D.P. Tieleman, P.C. Biggin, G.R. Smith, and M.S. Sansom, *Simulation approaches to ion channel structure–function relationships.* Quarterly Reviews of Biophysics, 2001. **34**(04): p. 473-561.

7. M.J. Cabral, A. Kaufman, and R. MacKinnon, *Chemistry of ion coordination and hydration revealed by a K^+ channel-Fab complex at 2.0Å resolution.* Nature, 2001. **414**: p. 43-48.

8. J. Payandeh, T. Scheuer, N. Zheng, and W.A. Catterall, *The crystal structure of a voltage-gated sodium channel.* Nature, 2011. **475**(7356): p. 353-358.

9. P. Turq, J.M. Barthel, and M. Chemla, *Transport, relaxation, and kinetic processes in electrolyte solutions*. Vol. 57. 2012: Springer Science & Business Media.

10. G.H. Nancollas, *The thermodynamics of metal-complex and ion-pair formation.* Coordination Chemistry Reviews, 1970. **5**(4): p. 379-415.

11. B. Eisenberg, *Ionic interactions are everywhere.* Physiology, 2013. **28**(1): p. 28-38.

12. Y.Q. Gao, *Simple theoretical model for ion cooperativity in aqueous solutions of simple inorganic salts and its effect on water surface tension.* Journal of Physical Chemistry B, 2011. **115**(43): p. 12466-12472.

13. Y.Q. Gao, *Simple theory for salt effects on the solubility of amide.* Journal of Physical Chemistry B, 2012. **116**(33): p. 9934-9943.

14. L. Yang, Y. Fan, and Y.Q. Gao, *Differences of cations and anions: Their hydration, surface adsorption, and impact on water dynamics.* Journal of Physical Chemistry B, 2011. **115**(43): p. 12456-12465.

15. K.D. Collins, G.W. Neilson, and J.E. Enderby, *Ions in water: characterizing the forces that control chemical processes and biological structure.* Biophysical Chemistry, 2007. **128**(2): p. 95-104.

16. F. Hofmeister, *Zur Lehre von der Wirkung der Salze.* Archiv für experimentelle Pathologie und Pharmakologie, 1888. **24**(4): p. 247-260.

17. Z. Yang, *Hofmeister effects: an explanation for the impact of ionic liquids on biocatalysis.* Journal of Biotechnology., 2009. **144**(1): p. 12-22.

18. S.C. Flores, J. Kherb, N. Konelick, X. Chen, and P.S. Cremer, *The effects of Hofmeister cations at negatively charged hydrophilic surfaces.* Journal of Physical Chemistry C, 2012. **116**(9): p. 5730-5734.

19. M. Eigen, *Schallabsorption in Elektrolytlösungen als Folge chemischer Relaxation II. Meßergebnisse und Relaxationsmechanismen für 2—2-wertige Elektrolyte.* Berichte der Bunsengesellschaft für Physikalische Chemie, 1962. **66**(2): p. 107-121.

20. Y. Luo and B. Roux, *Simulation of osmotic pressure in concentrated aqueous salt solutions.* Journal of Physical Chemistry Letters, 2009. **1**(1): p. 183-189.

21. A. Vila Verde and R. Lipowsky, *Cooperative slowdown of water rotation near densely charged ions is intense but short-ranged.* Journal of Physical Chemistry B, 2013. **117**(36): p. 10556-10566.

22. M.J. Wiedemair, A.K. Weiss, and B.M. Rode, *Ab initio quantum mechanical simulations confirm the formation of all postulated species in ionic dissociation.* Physical Chemistry Chemical Physics, 2014. **16**(16): p. 7368-7376.

23. D.E. Woon and T.H.J. Dunning, *The Pronounced Effect of Microsolvation on Diatomic Alkali Halides: Ab Initio Modeling of MX (H_2O)n (M= Li, Na; X= F, Cl; n= 1-3).* Journal of the American Chemical Society, 1995. **117**(3): p. 1090-1097.

24. G.H. Peslherbe, B.M. Ladanyi, and J.T. Hynes, *Trajectory study of photodissociation dynamics in the NaI (H2O) cluster system.* Journal of Physical Chemistry A, 1998. **102**(23): p. 4100-4110.

25. C.P. Petersen and M.S. Gordon, *Solvation of sodium chloride: an effective fragment study of NaCl (H_2O)n.* Journal of Physical Chemistry A, 1999. **103**(21): p. 4162-4166.

26. G.H. Peslherbe, B.M. Ladanyi, and J.T. Hynes, *Free energetics of NaI contact and solvent-separated ion-pairs in water clusters.* Journal of Physical Chemistry A, 2000. **104**(19): p. 4533-4548.

27. C.W. Liu, F. Wang, L. Yang, X.Z. Li, W.J. Zheng, and Y.Q. Gao, *Stable salt–water cluster structures reflect the delicate competition between ion–water and water–water interactions.* Journal of Physical Chemistry B, 2014. **118**(3): p. 743-751.

28. J.P. Toennies and A.F. Vilesov, *Superfluid helium droplets: a uniquely cold nanomatrix for molecules and molecular complexes.* Angewandte Chemie International Edition, 2004. **43**(20): p. 2622-2648.

29. L. Andrews and M. Moskovits, *Chemistry and physics of matrix isolated species*. 1989: North Holland Publishing Company.

30. M.E. Jacox, *Ground-State Vibrational Energy Levels of Polyatomic Transient Molecules.* Journal of Physical and Chemical Reference Data, 1984. **13**(4): p. 945-1068.

31. G. Scoles, *Atomic and molecular beam methods*. Vol. 1. 1988: Oxford University Press New York.

32. H. Pauly, *Atom, Molecule, and Cluster Beams II: Cluster Beams, Fast and Slow Beams, Accessory Equipment and Applications*. Vol. 32. 2013: Springer Science & Business Media.

33. J. Close, F. Federmann, K. Hoffmann, and N. Quaas, *Helium droplets: A nanoscale cryostat for high resolution spectroscopy and studies of quantized vorticity.* Journal of Low Temperature Physics, 1998. **111**(3): p. 661-676.

34. A. Hofmann, *Matter and methods at low temperatures: F. Pobell Springer-Verlag, Berlin, Germany,* 1993, Elsevier.

35. S. Yang and A.M. Ellis, *Helium droplets: a chemistry perspective.* Chemical Society Reviews, 2013. **42**(2): p. 472-484.

36. R. Laboratorium, *Communications from the Kamerlingh Onnes Laboratory of the University of Leiden*. Vol. 9. 1908: Kamerlingh Onnes Laboratorium, Rijksuniversiteit.

37. M. Weilert, D.L. Whitaker, H. Maris, and G. Seidel, *Magnetic levitation and noncoalescence of liquid helium.* Physical Review Letters, 1996. **77**(23): p. 4840.

38. M. Weilert, D.L. Whitaker, H. Maris, and G. Seidel, *Laser levitation of superfluid helium.* Journal of Low Temperature Physics, 1995. **98**(1): p. 17-35.

39. C.C.Tsao, J.D. Lobo, M. Okumura, and S.Y. Lo, *Generation of charged droplets by field ionization of liquid helium.* Journal of Physics D: Applied Physics, 1998. **31**(17): p. 2195.

40. V. Ghazarian, J. Eloranta, and V. Apkarian, *Universal molecule injector in liquid helium: Pulsed cryogenic doped helium droplet source.* Review of Scientific Instruments, 2002. **73**(10): p. 3606-3613.

41. J.B. Anderson, C.A. Traynor, and B.M. Boghosian, *An exact quantum Monte Carlo calculation of the helium–helium intermolecular potential.* Journal of Chemical Physics, 1993. **99**(1): p. 345-351.

42. H. Buchenau, E. Knuth, J. Northby, J. Toennies, and C. Winkler, *Mass spectra and time-of-flight distributions of helium cluster beams.* Journal of Chemical Physics, 1990. **92**(11): p. 6875-6889.

43. L.F. Gomez, E. Loginov, R. Sliter, and A.F. Vilesov, *Sizes of large He droplets.* Journal of Chemical Physics, 2011. **135**(15): p. 154201.

44. S. Stringari and J. Treiner, *Systematics of liquid helium clusters.* Journal of Chemical Physics, 1987. **87**(8): p. 5021-5027.

45. D. Brink and S. Stringari, *Density of states and evaporation rate of helium clusters.* Zeitschrift für Physik D Atoms, Molecules and Clusters, 1990. **15**(3): p. 257-263.

46. A. Guirao, M. Pi, and M. Barranco, *Finite size effects in the evaporation rate of ^{3}He clusters.* Zeitschrift für Physik D Atoms, Molecules and Clusters, 1991. **21**(2): p. 185-188.

47. E. Becker, R. Klingelhöfer, and P. Lohse, *Notizen: Strahlen aus kondensiertem Helium im Hochvakuum.* Zeitschrift für Naturforschung A, 1961. **16**(11): p. 1259-1259.

48. J.P. Toennies and A.F. Vilesov, *Spectroscopy of atoms and molecules in liquid helium.* Annual Review of Physical Chemistry, 1998. **49**(1): p. 1-41.

49. J. Northby, *Experimental studies of helium droplets.* Journal of Chemical Physics, 2001. **115**(22): p. 10065-10077.

50. H. Buchenau, J. Toennies, and J. Northby, *Excitation and ionization of ^{4}He clusters by electrons.* Journal of Chemical Physics, 1991. **95**(11): p. 8134-8148.

51. J. Harms, J.P. Toennies, and F. Dalfovo, *Density of superfluid helium droplets.* Physical Review B, 1998. **58**(6): p. 3341.

52. Knuth, E. and U. Henne, *Average size and size distribution of large droplets produced in a free-jet expansion of a liquid.* Journal of Chemical Physics, 1999. **110**(5): p. 2664-2668.

53. M.N. Slipchenko, S. Kuma, T. Momose, and A.F. Vilesov, *Intense pulsed helium droplet beams.* Review of Scientific Instruments, 2002. **73**(10): p. 3600-3605.

54. S. Yang and A.M. Ellis, *Selecting the size of helium nanodroplets using time-resolved probing of a pulsed helium droplet beam.* Review of Scientific Instruments, 2008. **79**(1): p. 016106.

55. D. Pentlehner, R. Riechers, B. Dick, A. Slenczka, U. Even, N. Lavie, R. Brown, and K. Luria, *Rapidly pulsed helium droplet source.* Review of Scientific Instruments, 2009. **80**(4): p. 043302.

56. M. Cross and P. Anderson, *Proceedings of the Fourteenth International Conference on Low Temperature Physics.* 1975.

57. J. Gspann, G. Krieg, and H. Vollmar, Atomic interaction with quantum fluid clusters: ^{3}He-cluster beam generation and Cs-scattering by 4He-clusters. Le Journal de Physique Colloques, 1977. **38**(C2): p. 171-173.

58. J. Gspann and H. Vollmar, *Momentum transfer to helium-3 and helium-4-microdroplets in heavy atom collisions.* Le Journal de Physique Colloques, 1978. **39**(C6): p. 330-331.

59. S. Datz, *The physics of electronic and atomic collisions*. New York 1982: North Holland Publishing Company.

60. J. Gspann and R. Ries, *^{3}He and ^{4}He clusters colliding with Cs atoms: Total cross sections for varying impact speed.* Surface Science, 1985. **156**: p. 195-200.

61. O.M. Belotserkovskii, *Rarefied gas dynamics*. Vol. 2. 2013: Springer Science & Business Media.

62. O. Echt, P. Jena, B. Rao, and S. Khanna, *Physics and chemistry of small clusters.* Jena, P., Rao, BK, Khanna, SN,(eds.), 1987. **158**: p. 623.

63. J. Gspann, *Atomic impact experiments with free helium-3 and helium-4 clusters.* Zeitschrift für Physik B Condensed Matter, 1995. **98**(3): p. 405-411.

64. M. Lewerenz, B. Schilling, and J. Toennies, *Successive capture and coagulation of atoms and molecules to small clusters in large liquid helium clusters.* Journal of Chemical Physics, 1995. **102**(20): p. 8191-8207.

65. A. Bartelt, J. Close, F. Federmann, N. Quaas, and J. Toennies, *Cold metal clusters: Helium droplets as a nanoscale cryostat.* Physical Review Letters, 1996. **77**(17): p. 3525.

66. A. Lindinger, J.P. Toennies, and A.F. Vilesov, *High resolution vibronic spectra of the amino acids tryptophan and tyrosine in 0.38 K cold helium droplets.* Journal of Chemical Physics, 1999. **110**(3): p. 1429-1436.

67. J. Tandy, C. Feng, A. Boatwright, G. Sarma, A.M. Sadoon, A. Shirley, N.D.N. Rodrigues, E.M. Cunningham, S. Yang, and A.M. Ellis, *Communication: Infrared spectroscopy of salt-water complexes.* Journal of Chemical Physics, 2016. **144**(12): p. 121103.

68. M. Choi, G. Douberly, T. Falconer, W. Lewis, C. Lindsay, J. Merritt, P. Stiles, and R. Miller, *Infrared spectroscopy of helium nanodroplets: novel methods for physics and chemistry.* International Reviews in Physical Chemistry, 2006. **25**(1-2): p. 15-75.

69. S. Goyal, D. Schutt, and G. Scoles, *Vibrational spectroscopy of sulfur hexafluoride attached to helium clusters.* Physical Review Letters, 1992. **69**(6): p. 933.

70. R. Fröchtenicht, J. Toennies, and A. Vilesov, *High-resolution infrared spectroscopy of SF_6 embedded in He clusters.* Chemical Physics Letters, 1994. **229**(1-2): p. 1-7.

71. R.Z. Li, C.W. Liu, Y.Q. Gao, H. Jiang, H.G. Xu, and W.J. Zheng, *Microsolvation of LiI and CsI in water: Anion photoelectron spectroscopy and ab initio calculations.* Journal of the American Chemical Society, 2013. **135**(13): p. 5190-5199.

72. P. Jungwirth, *How many waters are necessary to dissolve a rock salt molecule?* Journal of Physical Chemistry A, 2000. **104**(1): p. 145-148.

73. S. Godinho, P.C. do Couto, and B.C. Cabral, *Charge separation and charge transfer to solvent in NaCl–water clusters.* Chemical Physics Letters, 2004. **399**(1): p. 200-205.

74. S. Godinho, P. Cabral do Couto, and B. Costa Cabral, *Polarization effects and charge separation in AgCl-water clusters.* The Journal of Chemical Physics, 2005. **122**(4): p. 044316.

75. A.C. Olleta, H.M. Lee, and K.S. Kim, *Ab initio study of hydrated sodium halides Na X (H_2O) 1–6 (X= F, Cl, Br, and I).* Journal of Chemical Physics, 2006. **124**(2): p. 024321.

76. N.J. Singh, H.-B. Yi, S.K. Min, M. Park, and K.S. Kim, *Dissolution nature of cesium fluoride by water molecules.* Journal of Physical Chemistry B, 2006. **110**(8): p. 3808-3815.

77. P. Jungwirth and D.J. Tobias, *Ions at the air/water interface*. 2002, ACS Publications.

78. C.K. Siu, B.S. Fox-Beyer, M.K. Beyer, and V.E. Bondybey, *Ab initio molecular dynamics studies of ionic dissolution and precipitation of sodium chloride and silver chloride in water clusters, NaCl(H_2O)n and AgCl(H_2O)n, n= 6, 10, and 14.* Chemistry–A European Journal, 2006. **12**(24): p. 6382-6392.

79. G. Gregoire, M. Mons, I. Dimicoli, C. Dedonder-Lardeux, C. Jouvet, S. Martrenchard, and D. Solgadi, *Femtosecond pump–probe ionization of small (NaI–S)n clusters, S: H_2O, NH_3: A tool to probe the structure of the cluster.* Journal of Chemical Physics, 2000. **112**(20): p. 8794-8805.

80. B.S. Ault, *Infrared spectra of argon matrix-isolated alkali halide salt/water complexes.* Journal of the American Chemical Society, 1978. **100**(8): p. 2426-2433.

81. A. Mizoguchi, Y. Ohshima, and Y. Endo, *Microscopic hydration of the sodium chloride ion pair.* Journal of the American Chemical Society, 2003. **125**(7): p. 1716-1717.

82. A. Mizoguchi, Y. Ohshima, and Y. Endo, *The study for the incipient solvation process of NaCl in water: The observation of the NaCl–(H_2O)n (n=1,2,and3) complexes using Fourier-transform microwave spectroscopy.* Journal of Chemical Physics, 2011. **135**(6): p. 064307.

83. R. Miller and P. Kusch, *Molecular composition of alkali halide vapors.* Journal of Chemical Physics, 1956. **25**(5): p. 860-876.

84. C.T. Ewing and K.H. Stern, *Vaporization kinetics of sodium chloride. I. Solid.* Journal of Physical Chemistry, 1973. **77**(11): p. 1442-1449.

85. J.E. Mayer and I.H. Wintner, *Measurements of low vapor pressures of alkali halides.* Journal of Chemical Physics, 1938. **6**(6): p. 301-306.

86. J. Giordmaine and R.C. Miller, *Tunable coherent parametric oscillation in $LiNbO_3$ at optical frequencies.* Physical Review Letters, 1965. **14**(24): p. 973.

87. S. Pinho and E. Macedo, *Solubility of NaCl, NaBr, and KCl in water, methanol, ethanol, and their mixed solvents.* Journal of Chemical & Engineering Data, 2005. **50**(1): p. 29-32.

88. M. Li, D. Constantinescu, L. Wang, A. Mohs, and J. Gmehling, *Solubilities of NaCl, KCl, LiCl, and LiBr in methanol, ethanol, acetone, and mixed solvents and correlation using the LIQUAC model.* Industrial & Engineering Chemistry Research, 2010. **49**(10): p. 4981-4988.

89. D. Bowron and J. Finney, *Anion bridges drive salting out of a simple amphiphile from aqueous solution.* Physical Review Letters, 2002. **89**(21): p. 215508.

90. D. Paschek, A. Geiger, M. Hervé, and D. Suter, *Adding salt to an aqueous solution of t-butanol: Is hydrophobic association enhanced or reduced?* Journal of Chemical Physics, 2006. **124**(15): p. 154508.

91. Y. Shao, Z. Gan, E. Epifanovsky, A. Gilbert, M. Wormit, J. Kussmann, A.W. Lange, A. Behn, J. Deng, and X. Feng, *Advances in molecular quantum chemistry contained in the Q-Chem 4 program package.* Molecular Physics, 2015. **113**(2): p. 184-215.

92. Y. Zhao and D.G. Truhlar, *The M06 suite of density functionals for main group thermochemistry, thermochemical kinetics, noncovalent interactions, excited states, and transition elements: two new functionals and systematic testing of four M06-class functionals and 12 other functionals.* Theoretical Chemistry Accounts: Theory, Computation, and Modeling (Theoretica Chimica Acta), 2008. **120**(1): p. 215-241.

93. C.Y. Lin, A.T. Gilbert, and P.M. Gill, *Calculating molecular vibrational spectra beyond the harmonic approximation.* Theoretical Chemistry Accounts: Theory, Computation, and Modeling (Theoretica Chimica Acta), 2008. **120**(1): p. 23-35.

94. P.L. Raston, G.E. Douberly, and W. Jäger, *Single and double resonance spectroscopy of methanol embedded in superfluid helium nanodroplets.* Journal of Chemical Physics, 2014. **141**(4): p. 044301.

95. O.M. Cabarcos, C.J. Weinheimer, T.J. Martınez, and J.M. Lisy, *The solvation of chloride by methanol—surface versus interior cluster ion states.* Journal of Chemical Physics, 1999. **110**(19): p. 9516-9526.

96. J.P. Beck and J.M. Lisy, *Cooperatively Enhanced Ionic Hydrogen Bonds in $Cl^-(CH_3OH)$ 1− 3 Ar Clusters.* Journal of Physical Chemistry A, 2010. **114**(37): p. 10011-10015.

97. C.J. Gruenloh, G.M. Florio, J.R. Carney, F.C. Hagemeister, and T.S. Zwier, *C−H Stretch Modes as a Probe of H-Bonding in Methanol-Containing Clusters.* Journal of Physical Chemistry A, 1999. **103**(4): p. 496-502.

98. Y. Marcus, *Effect of ions on the structure of water.* Pure Appled. Chemistery., 2010. **82**(10): p. 1889-1899.

99. S. Moelbert, B. Normand, and P. De Los Rios, *Kosmotropes and chaotropes: modelling preferential exclusion, binding and aggregate stability.* Biophysical Chemistry, 2004. **112**(1): p. 45-57.

100. C.W. Liu and Y.Q. Gao, *Understanding the microsolvation of salts in molecular clusters.* International Journal of Quantum Chemistry, 2015. **115**(9): p. 541-544.

101. H.B. Gray, *Electrons and chemical bonding*. 1965: WA Benjamin, Inc.

102. J. Dean, *Properties of atoms, radicals, and bonds.* Lange's handbook of chemistry, 1999.

103. K.D. Collins, *Ion hydration: Implications for cellular function, polyelectrolytes, and protein crystallization.* Biophysical Chemistry, 2006. **119**(3): p. 271-281.

104. C.J. Fennell, A. Bizjak, V. Vlachy, and K.A. Dill, *Ion pairing in molecular simulations of aqueous alkali halide solutions.* Journal of Physical Chemistry. B, 2009. **113**(19): p. 6782.

105. M. Lukšič, C.J. Fennell, and K.A. Dill, *Using interpolation for fast and accurate calculation of ion–ion interactions.* Journal of Physical Chemistry. B, 2014. **118**(28): p. 8017.

106. J. Mähler and I. Persson, *A study of the hydration of the alkali metal ions in aqueous solution.* Inorganic Chemistry, 2011. **51**(1): p. 425-438.

107. M. J. Frisch, G. W. Trucks, H. B. Schlegel, G. E. Scuseria, M. A. Robb, J. R. Cheeseman, G. Scalmani, V. Barone, G. A. Petersson, H. Nakatsuji, X. Li, M. Caricato, A. Marenich, J. Bloino, B. G. Janesko, R. Gomperts, B. Mennucci, H. P. Hratchian, J. V. Ortiz, A. F. Izmaylov, J. L. Sonnenberg, D. Williams-Young, F. Ding, F. Lipparini, F. Egidi, J. Goings, B. Peng, A. Petrone, T. Henderson, D. Ranasinghe, V. G. Zakrzewski, J. Gao, N. Rega, G. Zheng, W. Liang, M. Hada, M. Ehara, K. Toyota, R. Fukuda, J. Hasegawa, M. Ishida, T. Nakajima, Y. Honda, O. Kitao, H. Nakai, T. Vreven, K. Throssell, J. A. Montgomery, Jr., J. E. Peralta, F. Ogliaro, M. Bearpark, J. J. Heyd, E. Brothers, K. N. Kudin, V. N. Staroverov, T. Keith, R. Kobayashi, J. Normand, K. Raghavachari, A. Rendell, J. C. Burant, S. S. Iyengar, J. Tomasi, M. Cossi, J. M. Millam, M. Klene, C. Adamo, R. Cammi, J. W. Ochterski, R. L. Martin, K. Morokuma, O. Farkas, J. B. Foresman, and D. J. Fox, *GAUSSIAN09. Gaussian Inc., Wallingford, CT, USA*. 2009.

108. C. Møller and M.S. Plesset, *Note on an approximation treatment for many-electron systems.* Physical Review, 1934. **46**(7): p. 618.

109. P.J. Hay and W.R. Wadt, *Ab initio effective core potentials for molecular calculations. Potentials for the transition metal atoms Sc to Hg.* Journal of Chemical Physics, 1985. **82**(1): p. 270-283.

110. K.L. Schuchardt, B.T. Didier, T. Elsethagen, L. Sun, V. Gurumoorthi, J. Chase, J. Li, and T.L. Windus, *Basis set exchange: a community database for computational sciences.* Journal of Chemical Information and Modeling, 2007. **47**(3): p. 1045-1052.

111. R.D. Johnson III, *NIST Computational Chemistry Comparison and Benchmark Database, NIST Standard Reference Database Number 101, Release 15b. 2011.* cccbdb. nist. gov, 2005.

112. L. Friedman, *Mass spectrum of lithium iodide.* Journal of Chemical Physics, 1955. **23**(3): p. 477-482.

113. L. Bencze, A. Lesar, and A. Popovic, *The evaporation thermodynamics of lithium iodide. Mass spectrometric and ab initio studies.* Rapid Communications in Mass Spectrometry, 1998. **12**(14): p. 917-930.

114. A.M Sadoon, G. Sarma, E.M. Cunningham, J. Tandy, M.W. Hanson-Heine, N.A. Besley, S. Yang, and A.M. Ellis, *Infrared spectroscopy of NaCl $(CH_3OH)n$ complexes in helium nanodroplets.* Journal of Physical Chemistry A, 2016. **120**(41): p. 8085-8092.

115. J. Kim, H.M. Lee, S.B. Suh, D. Majumdar, and K.S. Kim, *Comparative ab initio study of the structures, energetics and spectra of $X^-\cdot(H_2O)_n$ n= 1–4 [X= F, Cl, Br, I] clusters.* Journal of Chemical Physics, 2000. **113**(13): p. 5259-5272.

116. H.M. Lee and K.S. Kim, *Structures and spectra of iodide–water clusters $I^-(H_2O)_n$ n= 1–6: An ab initio study.* Journal of Chemical Physics, 2001. **114**(10): p. 4461-4471.

117. D. Majumdar, J. Kim, and K.S. Kim, *Charge transfer to solvent (CTTS) energies of small $X^-(H_2O)_n$ n= 1–4 (X= F, Cl, Br, I) clusters: Ab initio study.* Journal of Chemical Physics, 2000. **112**(1): p. 101-105.

118. J.D. Smith, R.J. Saykally, and P.L. Geissler, *The effects of dissolved halide anions on hydrogen bonding in liquid water.* Journal of the American Chemical Society, 2007. **129**(45): p. 13847-13856.

119. T. Martin and T. Bergmann, *Solvation in clusters: lithium iodide in alcohol.* Journal of Physical Chemistry, 1987. **91**(10): p. 2530-2533.

120. T. Megyes, T. Radnai, and A. Wakisaka, *Complementary Relation between Ion− Counterion and Ion− Solvent Interaction in Lithium Halide− Methanol Solutions.* Journal of Physical Chemistry A, 2002. **106**(35): p. 8059-8065.

121. P. Kumar, A.D. Kulkarni, and S. Yashonath, *Influence of a Counterion on the Ion Atmosphere of an Anion: A Molecular Dynamics Study of LiX and CsX (X= F^-, Cl^-, I^-) in Methanol.* Journal of Physical Chemistry B, 2015. **119**(34): p. 10921-10933.

122. T. Megyes, T. Radnai, T. Grósz, and G. Pálinkás, *X-ray diffraction study of lithium halides in methanol.* Journal of Molecular Liquids. 2002. **101**(1-3): p. 3-18.

123. Y. Kameda, T. Usuki, and O. Uemura, *The structure analysis of highly concentrated Li-salt solutions.* High Temperature Materials and Processes. (London), 1999. **18**(1-2): p. 27-40.

124. Y. Kameda, H. Ebata, T. Usuki, and O. Uemura, *The coordination structure of Li+ in highly concentrated methanolic LiBr and LiI solutions.* Physica B: Condensed Matter, 1995. **213**: p. 477-479.

125. S. Mochizuki and A. Wakisaka, *Solvation for Ions and Counterions: Complementary Relation between Ion− Counterion and Ion− Solvent Interaction.* Journal of Physical Chemistry A, 2002. **106**(20): p. 5095-5100.

126. Rappoport, D. and F. Furche, *Property-optimized Gaussian basis sets for molecular response calculations.* Journal of Chemical Physics, 2010. **133**(13): p. 134105.

127. S. Yang, S.M. Brereton, and A.M. Ellis, *Controlled growth of helium nanodroplets from a pulsed source.* Review of Scientific Instruments, 2005. **76**(10): p. 104102.

128. J. Liu, B. Shepperson, A.M. Ellis, and S. Yang, *Core–shell effects in the ionization of doped helium nanodroplets.* Physical Chemistry Chemical Physics, 2011. **13**(31): p. 13920-13925.

129. S. Yang, S.M. Brereton, M.D. Wheeler, and A.M. Ellis, *Electron impact ionization of haloalkanes in helium nanodroplets.* Journal of Physical Chemistry A, 2006. **110**(5): p. 1791-1797.

130. S. Yang, S.M. Brereton, M.D. Wheeler, and A.M. Ellis, *Soft or hard ionization of molecules in helium nanodroplets? An electron impact investigation of alcohols and ethers.* Physical Chemistry Chemical Physics, 2005. **7**(24): p. 4082-4088.

131. B. Mamyrin, V. Karataev, D. Shmikk, and V. Zagulin, *The mass-reflectron, a new nonmagnetic time-of-flight mass spectrometer with high resolution.* Journal of Experimental and Theoretical Physics, 1973. **64**: p. 82-89.

132. W. Wiley and I.H. McLaren, *Time-of-flight mass spectrometer with improved resolution.* Review of Scientific Instruments, 1955. **26**(12): p. 1150-1157.

133. E. De Hoffmann and V. Stroobant, *Mass spectrometry: principles and applications*. 2007: John Wiley & Sons.

134. C. Brunnée, *The ideal mass analyzer: Fact or fiction?* International Journal of Mass Spectrometry and Ion Processes, 1987. **76**(2): p. 125-237.

135. J.H. Gross, *Mass spectrometry: a textbook*. 2006: Springer Science & Business Media.

136. R. Viswanathan and K. Hilpert, *Mass Spectrometric Study of the Vaporization of Cesium Iodide and Thermochemistry of $(CsI)_2$ (g) and $(CsI)_3$ (g).* Berichte der Bunsengesellschaft für Physikalische Chemie, 1984. **88**(2): p. 125-131.

137. J.G. Stark, H.G. Wallace, and M. MacGlashan, *Chemistry Data Book*. 1982: Murray London.

138. D.R. Stull, *Vapor pressure of pure substances. Organic and inorganic compounds.* Industrial & Engineering Chemistry, 1947. **39**(4): p. 517-540.

139. W.M. Haynes, *CRC Handbook of Chemistry and Physics*. 2014: CRC press.